Competing Orders in Strongly Correlated Systems

by

Ganesh Ramachandran

A thesis submitted in conformity with the requirements
for the degree of Doctor of Philosophy
Graduate Department of Physics
University of Toronto

Abstract

Competing Orders in Strongly Correlated Systems

Ganesh Ramachandran

Doctor of Philosophy

Graduate Department of Physics

University of Toronto

2012

Systems with competing orders are of great interest in condensed matter physics. When two phases have comparable energies, novel interplay effects such can be induced by tuning an appropriate parameter. In this thesis, we study two problems of competing orders - (i) ultracold atom gases with competing superfluidity and Charge Density Wave(CDW) orders, and (ii) low dimensional antiferromagnets with Neel order competing against various disordered ground states.

In the first part of the thesis, we study the attractive Hubbard model which could soon be realized in ultracold atom experiments. Close to half-filling, the superfluid ground state competes with a low-lying CDW phase. We study the collective excitations of the superfluid using the Generalized Random Phase Approximation (GRPA) and strong-coupling spin wave analysis. The competing CDW phase manifests as a roton-like excitation. We characterize the collective mode spectrum, setting benchmarks for experiments. We drive competition between orders by imposing superfluid flow. Superflow leads to various instabilities: in particular, we find a dynamical instability associated with CDW order. We also find a novel dynamical incommensurate instability analogous to exciton condensation in semiconductors.

In the second part, inspired by experiments on $Bi_3Mn_4O_{12}(NO_3)$(BMNO), we first study the interlayer dimer state in spin-S bilayer antiferromagnets. At a critical bilayer coupling strength, condensation of triplet excitations leads to Neel order. In describing

this transition, bond operator mean field theory suffers from systematic deviations. We bridge these deviations by taking into account corrections arising from higher spin excitations. The interlayer dimer state shows a field induced Néel transition, as seen in BMNO. Our results are relevant to the quantitative modelling of spin-S dimerized systems.

We then study the J_1 - J_2 model on the honeycomb lattice with frustrating next-nearest neighbour exchange. For $J_2 > J_1/6$, quantum and thermal fluctuations lead to lattice nematic states. For S=1/2, this lattice nematic takes the form of a valence bond solid. With $J_2 < J_1/6$, quantum fluctuations melt Néel order so as to give rise to a field induced Néel transition. This scenario can explain the observed properties of BMNO. We discuss implications for the honeycomb lattice Hubbard model.

Acknowledgements

After five very eventful years, I have many to thank for my wonderful experiences. Foremost, I am deeply grateful to Prof. Arun Paramekanti who has been an inspiring teacher, a hands-on supervisor and a caring mentor. It has been a privilege to work with him. I hope to take with me his thorough and honest approach to science.

I am grateful to members of my thesis committee, Prof. Y. B. Kim, Prof. J. Thywissen, Prof. Young-June Kim, and Prof. Erik Sorensen. I learnt a lot from discussions with them, and their valuable suggestions have made this thesis better.

Prof. G. Baskaran has been a steady source of inspiration and guidance. I am beholden to him for showing me the creative essence in physics. I am fortunate to have learnt from many excellent teachers: Dr. K. S. Balaji who introduced me to the joy of physics, Dr. Saugata Ghosh who encouraged me to pursue it, Prof. P. K. Thiruvikraman, Prof. Suresh Ramaswamy and Prof. Ashoke Sen who taught me the fundamentals and inspired me.

My collaborators Prof. A. A. Burkov and A. Mulder have made this thesis possible. I have learnt much from an enlightening collaboration with Dr. Shunji Tsuchiya.

My co-students and post-docs have played a large part in my graduate education. My sincere thanks go to Jean-Sébastien Bernier who showed me the ropes. I thank Christoph Puetter for innumerable discussions and for sharing the joys and frustrations of graduate school. He was a great co-organizer of dinners, journal clubs and kayak trips. I am particularly indebted to Jeffrey Rau who showed me it's possible to think about science in so many ways for so many hours a day. Tyler Dodds helped me understand tricks involved in bosonic mean-field theories used in Chapters 4 and 5. I thank So, Daniel, Matt, Dariush, Bohm-Jung, Furukawa-san, Si, J-M, Simon, William, Shubhro, Robert, Eric, Tamas and Manas for their friendship and many discussions. I wish Vijay many officemates just like himself, eager for discussions and reliable in running errands. I learnt much from Danshita-san and Siddharth at conferences.

‘The way you spend your days is the way you spend your life’. My officemates added colour, new ideas and the occasional box of Belgian truffles to my daily life. It was a pleasure to have Navin, Justin, Asma, Luke, Aida, Parinaz and Federico for company.

I cannot thank our administrative staff enough: Krystyna Biel has been a pillar of support since even before I reached Toronto, Teresa Baptista went to great lengths to help me with my TA duties, and I could always rely on April Seeley for support.

My happiest moments in Toronto were spent with friends. Jung-Yun, Josephine, Louis, Kai, Amir, Helder, Stefan, David, Nicola, Andre, Bogdan, Ioannis, Babak, Hanif, Karen, Winnie, Hanae, Brian, Diana, Pooja, Lawrence, Jamieson, Bertrand, Akiko, Tejas and Yeshwanth: you’ve taught me much and kept me sane. Thank you! A special thank you to Meital and Dor for the lovely times and the great hospitality. My best friend Edwin and Tanmay and Sachi, thank you for keeping me young!

Nancy and Harold, I will always cherish your friendship, generosity and warmth! A big thank you to Sambhavi *maami* for recipes, dinners, accommodation and for looking out for me. Bhuma perimma, thank you for the delicious love packed in yoghurt containers, your patient music lessons, the stories and the laughter. Bhuvana chithi and Ravi chithapa, your company always meant happiness and laughter. Thank you for the lovely evenings and *kucheri* rides. Sriram and Meera, you are the funnest cousins ever.

Thank you, Gopal chithapa, for being my earliest mentor and a shining example of the systematic acquisition of knowledge. I will always be indebted to Govinda mama, Shyamala Perimma, Sivakumar mama, Kamala perimma, Mangala chithi, Sundar mama, Chandri athai, Ambi perippa, Appa and Kala chithi for their unconditional love.

Katharine, your love and support have helped me finish with ‘grumpy magnets and annoyed honeybees’. Thank you for the countless little joys that make life liveable.

Amma, you have always wanted the very best for me. I can never thank you enough for your sacrifices and unceasing affection. Vachimma, your love knows no bounds. This thesis is dedicated to you two.

To Amma and Vachimma.

List of publications

The work presented in this thesis has been published in the following journal articles. I acknowledge specific contributions from co-authors below. These contributions are not discussed in this thesis - interested readers may refer to the journal articles.

- *Collective modes and superflow instabilities of strongly correlated Fermi superfluids*
  R. Ganesh, A. A. Burkov, A. Paramekanti
  Physical Review A **80**, 043612 (2009)

- *Spiral order by disorder and lattice nematic order in a frustrated Heisenberg antiferromagnet on the honeycomb lattice*
  A. Mulder, R. Ganesh, L. Capriotti, A. Paramekanti
  Physical Review B **81**, 214419 (2010)

  – Classical Monte Carlo simulations were performed by Prof. A. Paramekanti in conjunction with Dr. L. Capriotti

- *Quantum paramagnets on the honeycomb lattice and field-induced Néel order: Possible application to* $Bi_3Mn_4O_{12}(NO_3)$
  R. Ganesh, D. N. Sheng, Y. J. Kim, A. Paramekanti
  Physical Review B **83**, 144414 (2011)

  – Exact diagonalization for Heisenberg model with higher order exchange was performed by Prof. D. N. Sheng

- *Néel to dimer transition in spin-S antiferromagnets: Comparing bond operator theory with quantum Monte Carlo simulations for bilayer Heisenberg models*
  R. Ganesh, S. V. Isakov, A. Paramekanti
  Physical Review B **84**, 214412 (2011)

  – Quantum Monte Carlo simulations were performed by Dr. S. V. Isakov

Contents

Chapter 1

Introduction

1.1 Competing orders

Condensed matter physics is the study of macroscopic phases of matter. The ambitious aim of studying every phase of matter that exists in nature leads physicists to seek ever newer phases in a variety of systems. This search has led to impressive discoveries such as Bose-Einstein condensation in ultracold atoms and superconductivity in neutron stars. In recent times, systems with competing orders have emerged as a fertile breeding ground for novel phases. When two or more phases are in close proximity, a combination of strong interactions, quantum mechanics and finely balanced energy scales gives rise to rich behaviour. Various phenomena can be induced by tuning the fine balance between phases in such regimes. The best known example is perhaps the emergence of d-wave superconductivity in the high-T_c cuprates at the interface between antiferromagnetic and Fermi liquid phases.

Systems with competing order are fairly common in condensed matter physics, some examples are listed in Table 1.1. Typically, a tuning parameter tunes the relative energies of competing phases in these systems leading to a phase transition. In the vicinity of this phase transition, the energies of the phases are comparable and perturbations such

as disorder, magnetic field, pressure, currents, etc. can induce interplay of orders. An interesting route to generating interplay effects is to locally suppress the dominant phase. For example, superconductivity is suppressed in a vortex core due to the high energy cost of supercurrents, allowing competing orders to arise in the vortex core region. As shown in Fig. 1.1, antiferromagnetism has been observed[1, 2] in the vortex cores of high-T_c cuprates. Another example is seen in the Bose Hubbard model. Close to the Mott insulator-superfluid transition, in the limit of small hopping, disorder destabilizes the Mott insulator leading to a Bose glass phase[3] as shown in Fig. 1.1. Competing orders can also lead to coexistence phases which simultaneously show multiple orders. Fig. 1.1 shows such a coexistence phase in a pnictide material[4].

In this thesis, we study competing orders as reflected in collective excitations which embody the macroscopic degrees of freedom in a system. Typically, they contain information about all the interactions present and possible competing phases. An understanding of the collective mode spectrum allows us to manipulate excitations using suitable perturbations. This in turn, allows us to induce competition between phases and to reveal competing orders. We study competing phases in two very different contexts - ultracold atomic gases and low dimensional magnetism. In both cases, we will understand the effects of competing phases by means of the collective excitations. We present a brief introduction to these two systems and our motivations for studying them.

1.2 Ultracold atom gases

Ultracold atom gases have emerged as a versatile testing ground for models of condensed matter physics. Advances in cooling technologies have made it possible to trap dilute gases of bosonic or fermionic atoms at extremely cold temperatures of a few hundred nanoKelvins. On account of their low temperatures and high controllability, ultracold gases are well suited to the study of quantum condensed matter physics. They provide

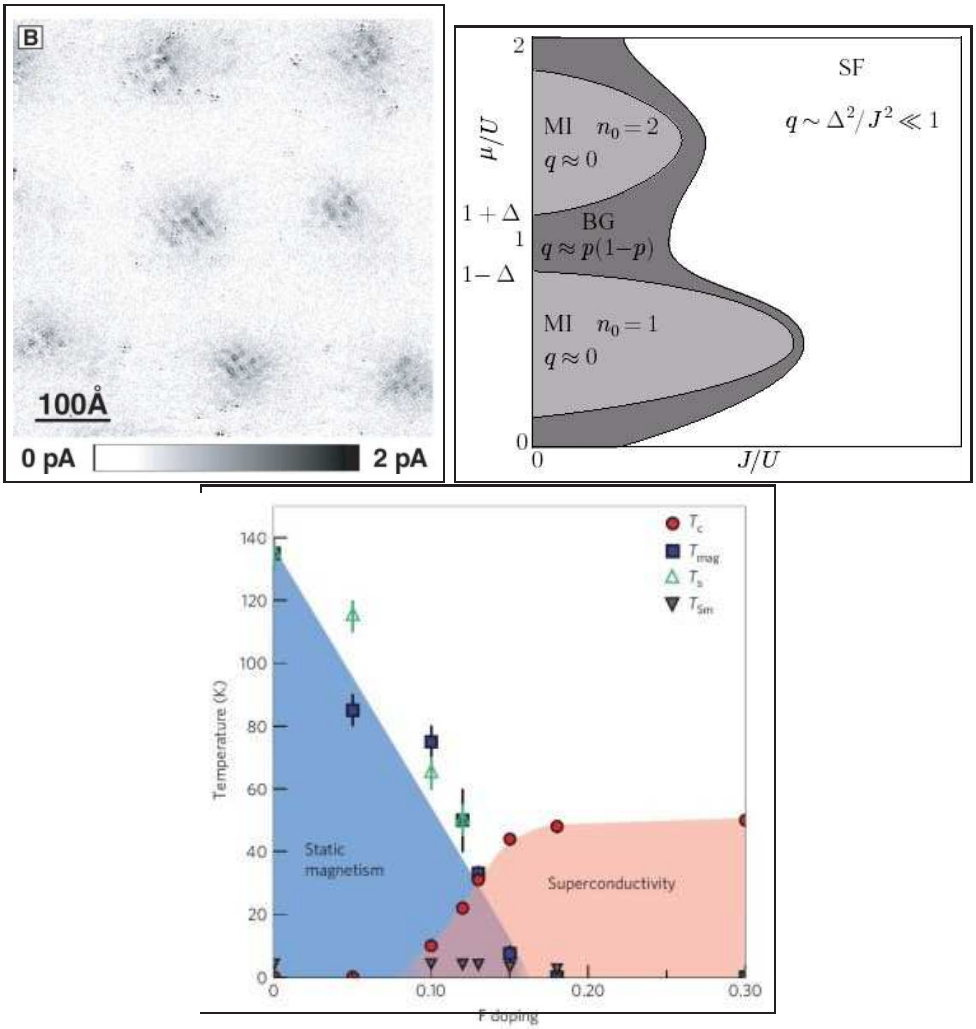

Figure 1.1: Exotic phenomena arising from competing orders: (Top Left) Scanning Tunneling Microscopy (STM) images[2] of a superconducting vortex in $Bi_2Sr_2CaCu_2O_{8+\delta}$ - from Science **295**, 5554 (2002). Reprinted with permission from AAAS.

(Top Right) Sketch of the phase diagram of the Bose Hubbard model in the presence of a disordered potential. A Bose Glass(BG) phase emerges at the interface between superfluid(SF) and Mott Insulating(MI) phases - from Ref. [3]).

(Bottom) Coexistence of superconductivity and antiferromagnetism[4] in $SmFeAsO_{1-x}F_x$ induced by doping. Figure reprinted by permission from Macmillan Publishers Ltd: Nature materials **8**, 310 ©2009.

Table 1.1: Examples of systems with competing order

System	Tuning Parameter	Competing Orders
High-T_c Cuprates[5]	Doping	Antiferromagnetism, Superconductivity
Pnictide materials[6]	Doping	Stripe-like magnetic order, Superconductivity
$TiSe_2$[7]	Cu Intercalation/Pressure	Charge Density Wave order, Superconductivity
Bose Hubbard model[8]	Lattice potential	Mott Insulator, Superfluidity
URu_2Si_2[9]	Pressure	'Hidden order', Antiferromagnetism

clean experimental systems which are free of complications arising from extra degrees of freedom such as coupling to lattice phonons. They offer an unprecedented degree of tunability as the geometry, density and interaction strength can all be varied independently. In addition, 'optical lattices'[10] allow for the simulation of lattice problems that are of particular interest in the condensed matter context. Optical lattices are generated by counterpropagating laser beams which set up standing waves in the amplitude of the electromagnetic field. The coupling between atoms and the resulting electric field confines the atoms to the minima (or maxima) of the standing wave, creating an effective lattice potential. Square/cubic lattices have been generated in several experiments, and proposals have been put forward to emulate other lattice geometries[11]. With these advantages, experiments with ultracold atoms will help us understand non-perturbative features of models with strong correlations. An example of the simulation of condensed matter models using ultracold gases is the remarkable realization of the Mott insulator-superfluid transition[12] in the Bose-Hubbard model[8]. Both sides of this phase transition were accessed experimentally by tuning the optical lattice potential.

In this thesis, we study models of Fermi gases which present a harder experimental challenge than Bose systems (see Ref.[13, 14] for reviews). We study fermions with attractive interactions in the lowest band of an optical lattice. At low enough temperatures, the fermions are expected to form a superfluid. Such superfluidity of fermions in an optical lattice has already been demonstrated[15], however the superfluid phase of the single-band Hubbard model has not yet been realized as the temperatures required are beyond the limits of current cooling technologies. Theoretical proposals have suggested novel techniques to further lower temperatures[16, 17, 18] which may soon allow experimental realizations of the Hubbard model.

Ultracold gases offer a great advantage over solid state materials in that the strength of interactions can be easily tuned. Being extremely dilute, ultracold atoms only interact via contact scattering, which can be characterized by the s-wave scattering length. The phenomenon of Feshbach resonance[13] allows this scattering length to be tuned using an applied magnetic field. Hyperfine states of fermionic atoms, typically Lithium (^{6}Li) or Potassium (^{40}K), mimic the spin states of an electron. During a scattering process, two fermions can couple to a bound state in the closed channel (corresponding to a hyperfine spin-triplet state of the two scattering fermions). An applied magnetic field tunes the energy of this bound state, and thereby tunes the scattering length of fermions in the open channel. Thus, an applied magnetic field can tune the strength of contact interactions in a fermionic system. Projected to the lowest band of an optical lattice, this naturally simulates the Hubbard interaction[19]. On the repulsive side of the resonance, the system is metastable as three-body processes can lead to formation of bound molecules. However, the attractive model suffers from no such limitation and can be studied by experiments[20].

A strong motivation to experimentally study the attractive Hubbard model stems from the BCS-BEC crossover[21, 14, 22, 23]. In the weakly interacting limit, the Bardeen-Cooper-Schrieffer(BCS) theory of superconductivity can be used to describe the system.

Fermions close to the Fermi surface are weakly bound, forming pairs in momentum space. In the limit of strong interactions however, fermions form Cooper pairs which are spatially tightly bound. These pairs behave as bosons which undergo Bose-Einstein condensation at low temperatures. These two phases are connected by a crossover, with all observable many-body properties changing smoothly. In fact, almost all observed properties vary monotonically across this transition. One of the few non-monotonic properties which can be used to identify the crossover point is the critical velocity of superfluid flow. We will next present a brief review of the problem of critical superfluid flow.

1.2.1 Critical velocity of a superfluid

The critical velocity of a superfluid is a long standing problem which has been investigated in many systems. One of the first significant theoretical advances was made by Landau who devised the eponymous criterion to determine the critical velocity. Landau considered a bosonic superfluid with excitations having a well-defined momentum $\mathbf{q}$ and an energy cost $\omega_{\mathbf{q}}$. An imposed superflow leads to a Doppler shift of excitations in the rest frame of the superfluid. At the critical velocity, the energy cost of making excitations vanishes and dissipation sets in due to the proliferation of excitations. The Landau criterion (see Appendix B.1 for derivation) gives $v_{crit} = \min_{\mathbf{q}}\{\omega(\mathbf{q})/q_{\|}\}$ where $q_{\|}$ is the component of momentum in the direction of flow.

However, in the canonical Bose superfluid ^{4}He, the observed critical velocity is always lower than the Landau criterion result. Due to a combination of strong correlations and the geometry of the experimental apparatus, the loss of superfluidity usually occurs through the proliferation of topological defects such as vortex rings. As the Landau criterion does not take into account such complex excitations, it significantly overestimates the critical velocity. It was realized early on that these issues can be circumvented by forcing superflow across a microscopic structureless obstacle, giving a strict test of the Landau criterion. With this objective, experiments studied ions moving through a ^{4}He

bath with a controlled velocity(see [24] for a review). However, the observed critical velocity still shows deviations from the Landau criterion result.

The advent of ultracold atom gases paved the way for the first successful test of the Landau criterion[25]. As ultracold gases are dilute and weakly interacting, an impurity atom moving through a Bose gas can precisely probe the Landau dissipation limit. In fact, further experiments using 'rough surfaces' instead of point-like impurities have also succeeded in realizing the Landau dissipation limit[26]. In addition, progress in the field of ultracold atom gases has opened up several new possibilities. A remarkable experiment using *Fermi* superfluids[26] measured critical velocity by dragging a shallow optical lattice (a rough surface) through the superfluid. The critical velocity beyond which dissipation sets in was measured as a function of interaction strength. In the limit of strong interactions (the BEC limit), the Landau criterion applies - the critical velocity is set by the Doppler-shifted sound mode becoming gapless. In this thesis, we call this a 'Landau instability' (a detailed discussion is given in Chapter 3). However, in the weakly interacting limit (the BCS limit), the critical velocity is instead set by 'depairing' - the cost of superfluid flow overwhelms the energy gain from condensation, and the system reverts to the normal (non-superfluid) state. Overall, the experimentally observed critical velocity is non-monotonic across the BCS-BEC crossover, due to the different mechanisms involved on either side.

The use of optical lattices has given rise to a further new class of instabilities. In the presence of a lattice, imposed flow can renormalize excitation energies beyond a simple Doppler shift. At the critical flow velocity, the renormalized excitation energies acquire complex energies resulting in exponentially growing fluctuations. These 'dynamical' instabilities have interesting observable consequences. Dynamical instabilities were first discussed in theoretical calculations[27, 28] in a system of lattice bosons. Subsequent experimental observations have confirmed theoretical predictions[29]. Even non-interacting bosons on a lattice undergo a dynamical instability, which is related to the superfluid

	Bosons	Fermions
Galilean Invariance	Landau[25]	Landau,Depairing[26]
Lattice	Landau, Dyn. Incomm.[29]	Landau, Depairing, Dyn. Incomm., Dyn. Comm.

Table 1.2: Types of superflow instabilities: Possibilities in cold atom experiments. The 'Dynamical Incommensurate' (Dyn. Incomm.) and 'Dynamical Commensurate' (Dyn. Comm.) instabilities are discussed in Chapter 3. The case of fermions on a lattice is the richest as it allows for the most possibilities. Also, it is the only category that has not yet been studied in experiments.

stiffness becoming negative. Interestingly, Ref.[28] shows that this instability is smoothly connected to the superfluid-Mott transition which occurs at zero flow.

In Part I of this thesis, we study the case of a Fermi gas loaded onto an optical lattice. As indicated in Table 1.2.1, this case captures all the instabilities present in other cases. In addition, it allows for new possibilities which we will explore in Chapter 3.

1.3 Low dimensional magnetism

Models of local moment magnetism provide well-understood examples of ordered phases and phase transitions. Historically, a close interplay between theory and experiment has led to a good understanding of magnetic order, e.g., antiferromagnetism, especially in three dimensional systems. The thermal transition from such magnetically ordered phases to paramagnetism has long occupied a central place in the field of condensed matter physics. In the last twenty years, low dimensional magnetism has emerged as an active field of research allowing for the study of *quantum phase transitions* between disparate phases. Reduced dimensionality disfavours conventional magnetic order and

makes way for exotic quantum behaviour. Here, we highlight two salient features of low dimensional magnetism to provide the context for Part II of this thesis.

1.3.1 Frustrated Magnetism

A successful route to generating novel phases in low-dimensional systems is 'frustration'. Frustrated magnets are spin systems in which all interactions cannot be maximally satisfied simultaneously. The simplest example is that of a triangular configuration with antiferromagnetically coupled Ising moments, as shown in Fig. 1.2.

As no single ground state satisfies all interactions in a frustrated system, there are many ground state configurations with comparable energies. A hallmark of frustrated systems is macroscopic degeneracy of the ground state in the classical limit. Indeed, the degree of degeneracy can be treated as a measure of frustration. Small effects such as quantum/thermal fluctuations, weak additional interactions, anisotropies, etc, become important in breaking this degeneracy and deciding the true low-energy state. The resulting state may correspond to novel symmetry-breaking or may even be a spin-liquid with no broken symmetries.

Frustrated magnets are usually antiferromagnets which obey the Curie-Weiss law ($\chi \sim C/\{T - \Theta_{CW}\}$) at high temperatures. In contrast to conventional magnets, they do not develop long-range order near the Curie-Weiss temperature. Any ordering, if at all, occurs at much lower energy scales set by weak effects which break the classical degeneracy. A quantitative measure of frustration can be obtained from the ratio $f = \Theta_{CW}/T_{ordering}$. Typically, $f \gtrsim 10$ indicates magnetic frustration.

An important motivation for the study of frustration in low dimensional systems is the possibility of generating novel states of matter in simple models which are experimentally realizable. Simple models of frustration, both classical and quantum, give rise to rich phase diagrams with various competing orders. This rich behaviour arises from large classical degeneracy and the interplay of weak degeneracy breaking effects. We give a

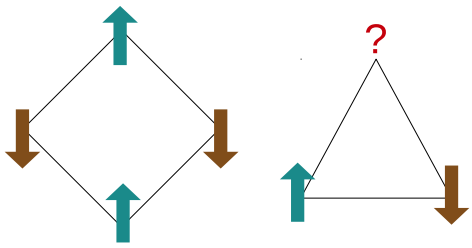

Figure 1.2: Example of frustration with antiferromagnetically coupled Ising moments: (Left) The Néel state maximally satisfies the exchange coupling on every bond, i.e., every bond connects anti-aligned spins. (Right) On the triangular lattice, this is impossible leading to frustration.

Table 1.3: Examples of novel states arising from simple models of frustration

State	Broken symmetry	Model
Chiral UUD [30]	Inversion, Translations	S=1/2 $J - J' - h$, triangular lattice
Spin nematic[31]	Spin rotations	S=1/2 $J_1(<0)$-$J_2(>0)$, square lattice
Spin octupolar[32]	Spin rotations	Classical antiferromagnet, Kagomé lattice
Stripe[33]	Lattice, Spin rotations	Large-S $J_1 - J_2$, square lattice
Plaquette RVB[34]	Lattice translations	S=1/2 $J_1 - J_2$, honeycomb lattice

(non-exhaustive) list of novel phases in frustrated systems in Table. 1.3. These phases can be experimentally probed in materials and/or numerically studied in model Hamiltonians.

1.3.2 Ground states with quantum entanglement

At low temperatures, quantum mechanics can lead to novel phases which have no analogues in classical physics. Such truly quantum phases have the distinguishing feature of entanglement, wherein interactions force two or more entities (electrons, atoms, spins, etc.) to become mutually intertwined. The quantum state of a single entity cannot be described independently as the wavefunction mixes the states of different constituents. The

best known example, perhaps, is BCS superconductivity which involves entanglement between electrons in momentum space. Historically, there have been very few examples of phases with entanglement, both in theoretical models of condensed matter physics and in solid state materials. Low dimensional magnets have dramatically changed this situation within the last twenty years, as a wide array of entangled phases have been proposed and experimentally realized.

A magnetically ordered state (for example, a Néel antiferromagnet), can be represented as a direct product of spins on each site. This kind of site-ordering has a simple classical analogue, in models of classical vector spins. In low dimensional magnetic systems however, strong quantum effects can prevent site-ordering leading to various degrees of entanglement. The simplest example is a Valence Bond Solid (VBS) in which spins on pairs of sites are entangled, forming singlet dimers. The ground state can be written as a direct product of bond-wavefunctions, and not site-wavefunctions. States with even higher degrees of entanglement have been proposed such as plaquette-ordered states (Fig. 1.3c), weakly coupled chains[35], etc. As an extreme case, low dimensional magnets also give rise to spin-liquids which cannot be written as direct products of wavefunctions restricted to any finite collection of sites. Fig. 1.3 shows a series of states with progressively higher degrees of entanglement.

With this motivation, we study two low-dimensional antiferromagnets in Part II of this thesis. Chapter 4 discusses a spin-S bilayer $J_1 - J_c$ model on the honeycomb and square lattices. It discusses the interlayer-VBS state, which does not break any symmetries. Chapter 5 deals with the $J_1 - J_2$ model on the honeycomb lattice. In various limits, this frustrated model exhibits 'lattice nematic' states, which break lattice rotational symmetry. In Chapter 6, we discuss field-induced Néel ordering in both these models. Our results are relevant to various experiments and numerical studies.

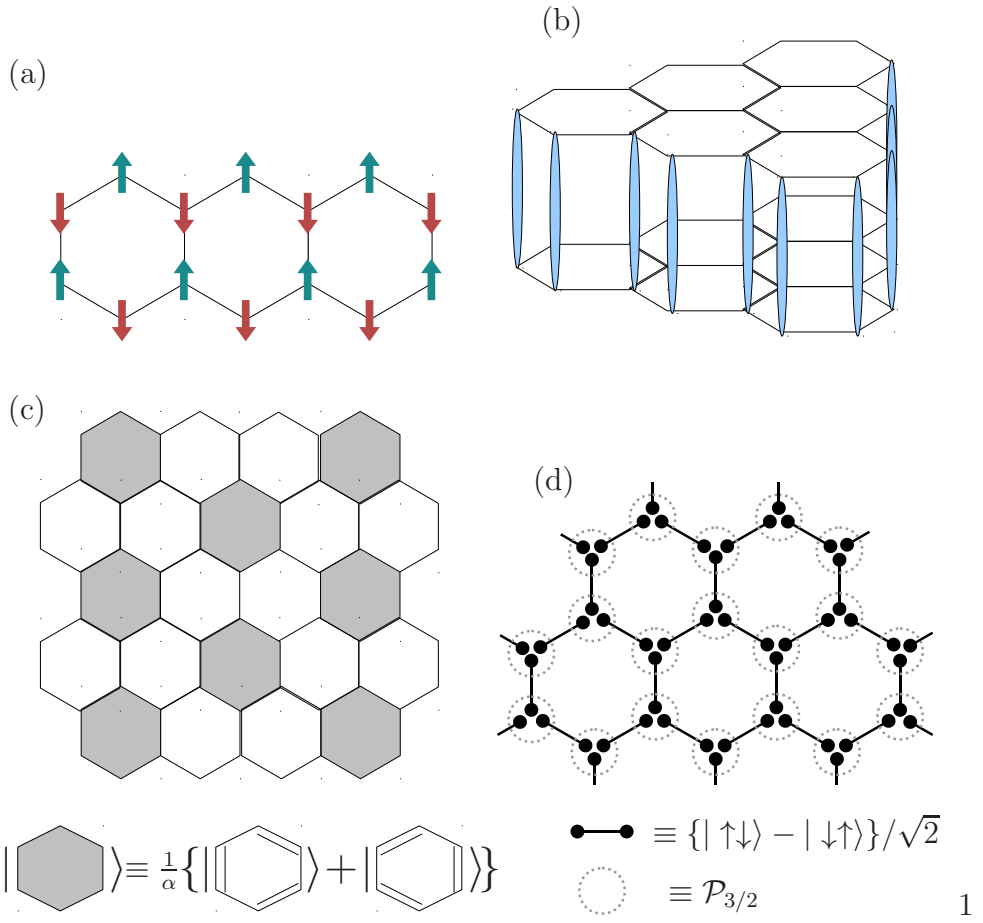

Figure 1.3: Entangled states on the honeycomb lattice: (a)-(d) show progressively higher entanglement. (a) is Néel ordered phase that occurs when only nearest neighbour exchange is present. (b) represents the interlayer VBS state in a honeycomb bilayer $J_1 - J_c$ system (see Chapter 4). Interlayer bonds form singlet dimers. (c) represents the 'plaquette RVB' state, proposed in the S=1/2 $J_1 - J_2$ model on the honeycomb lattice[36, 34]. The coefficient $\alpha = \sqrt{3/2}$ is a normalization factor. (d) is the S=3/2 Affleck-Kennedy-Lieb-Tasaki (AKLT) state on the honeycomb lattice, proposed for a model with second order exchange[37]. The operator $\mathcal{P}_{3/2}$ projects onto spin-3/2.

Part I

Superflow Instabilities in Ultracold Atom Gases

Chapter 2

Collective Mode of the Attractive Hubbard Model

2.1 Introduction

The Hubbard model was first introduced in the context of narrow band transition metals[38]. J. Hubbard phrased the problem of interacting electrons on a lattice in terms of Wannier states and argued that for a narrow band system, Coulomb interaction can be approximated as local on-site repulsion. The analogous *attractive* Hubbard model with on-site attraction has long been theoretically studied as a simple model system for s-wave superconductivity[39, 40]. It is only with the advent of ultracold atom physics that a clean, tunable experimental realization has come within reach. The Hamiltonian is given by

$$H = -t \sum_{\langle ij\rangle,\sigma\in\{\uparrow,\downarrow\}} \left(c^{\dagger}_{i,\sigma}c_{j,\sigma} + h.c.\right) - \mu \sum_{i,\sigma} n_{i,\sigma} - U \sum_{i} (n_{i,\uparrow} - \frac{1}{2})(n_{i,\downarrow} - \frac{1}{2}). \qquad (2.1)$$

The index i sums over all sites of the lattice. Quantum Monte Carlo studies[41, 42, 40] show that the ground state of this model is a superfluid. In this chapter, we use the Generalized Random Phase Approximation(GRPA) to find the collective mode spectrum arising from fluctuations around this superfluid state. We focus on the 2-dimensional

square lattice and the 3-dimensional cubic lattice.

The primary motivation for our study stems from experiments with ultracold Fermi gases which may soon realize this model Hamiltonian. Such experimental studies can study the regimes of validity of approximation schemes such as GRPA and can set the direction for improvements to theoretical methods. We quantitatively characterize the collective mode spectrum with a view to setting benchmarks for future experiments. Our results suggest simple checks to verify if the Hubbard model has indeed been realized. Another important motivation is the possibility of studying competing phases in this system theoretically and experimentally. As we discuss in the next section, this model shows competition between superfluidity and Charge Density Wave (CDW) phases. The collective mode spectrum provides a means of understanding and quantifying this competition. Further, in Chapter 3, we study imposed superflow in this system. Superflow induces competition between orders, and also leads to various instabilities. The collective mode spectrum serves as an excellent tool to understand the effect of superflow and the mechanisms of superflow breakdown.

Theoretically, various techniques have been used to evaluate the collective mode dispersion of the Hubbard model. Belkhir and Randeria[43] used the equations-of-motion method of Anderson[44] and Rickayzen[45], focussing only on the long-wavelength sound mode. They point out that the Random Phase Approximation(RPA) which is a weak-coupling approach, also correctly captures the strong coupling limit. Our calculations reaffirm this finding. An alternate derivation of the collective mode spectrum is presented in Ref.[46], which identifies the collective mode frequency from the poles of density-density response function. This paper presents an early calculation of a 'roton' gap in an extended Hubbard model (see section.2.5). As nearest neighbour repulsion is tuned, the superfluid state becomes unstable to various commensurate and incommensurate density orders. In Chapter 3, we will examine such instabilities induced instead by imposed superflow.

We begin this chapter with a discussion on the symmetries of the Hubbard model. In particular, we discuss an extra pseudospin symmetry at half-filling. With this background, we present the mean-field theory of superfluidity. We then use the GRPA formalism to calculate the collective mode spectrum. We present results for sound velocity and roton gap that can be measured in experiments on ultracold fermions. In the limit of strong coupling, we evaluate the collective mode by a spin-wave analysis of the relevant strong coupling spin model. We show that GRPA correctly captures the strong-coupling limit which suggests that GRPA is reliable for all interaction strengths. We summarize and discuss avenues for experimental investigation.

2.1.1 Symmetries of the Hubbard model

The Hubbard model of Eq. 2.1 possesses the following symmetries:

(i) U(1) global gauge transformations: The Hamiltonian is invariant under $c_{i,\sigma} \rightarrow c_{i,\sigma}e^{i\phi}$. In solid state materials, this symmetry is associated with the conservation of electric charge. As our fermions are electrically neutral, this symmetry is associated with fermion number conservation.

(ii) SU(2) global spin rotations: As there is no special direction picked out, the Hamiltonian is invariant under global spin rotations. The fermions mimic spin-1/2 electrons and transform under the SU(2) algebra.

(iii) When $\mu = 0$, the Hamiltonian is invariant under a sublattice dependent particle-hole transformation. The transformation $c_{i\sigma} \rightarrow \eta_i \tilde{c}^{\dagger}_{i,\sigma}$ leaves the Hamiltonian invariant when $\mu = 0$, where $\eta_i = \pm 1$ on the two sublattices. Clearly, this property is only valid on a bipartite lattice. In addition, the hopping term should only connect sites of different sublattices. For instance, on the square lattice, this symmetry is lost if we add next-nearest neighbour hopping with amplitude t'. We deduce that $\langle n_{i\sigma} \rangle = \langle \tilde{n}_{i\sigma} \rangle = 1 - \langle n_{i\sigma} \rangle$, which tells us that $\mu = 0$ corresponds to half-filling.

(iv) The attractive Hubbard model can be mapped onto the repulsive Hubbard model

using the following transformation. For the moment, let us consider the attractive Hubbard model in the presence of a magnetic field. The Hamiltonian can be written as

$$H = -t\sum_{\langle ij\rangle,\sigma}\left[c^{\dagger}_{i\sigma}c_{j,\sigma} + h.c.\right] - \mu\sum_{i,\sigma} n_{i,\sigma} - U\sum_{i}(n_{i,\uparrow}-1/2)(n_{i,\downarrow}-1/2) - B\sum_{i}(n_{i\uparrow}-n_{i,\downarrow}) \quad (2.2)$$

By transforming the down spins alone using $c_{i,\downarrow} \rightarrow \eta_i c^{\dagger}_{i,\downarrow}$, we obtain

$$H' = -t\sum_{\langle ij\rangle,\sigma}\left[c^{\dagger}_{i\sigma}c_{j,\sigma} + h.c.\right] - B\sum_{i,\sigma} n_{i,\sigma} + U\sum_{i}(n_{i,\uparrow}-1/2)(n_{i,\downarrow}-1/2) - \mu\sum_{i}(n_{i\uparrow}-n_{i,\downarrow}) \quad (2.3)$$

This transformation gives us a repulsive Hubbard model with the chemical potential μ and the magnetic field B interchanged. While the repulsive model is of great interest in the context of the high -T_c cuprates, it is difficult to simulate using ultracold gases. On the repulsive side of the Feshbach resonance, the Fermi gas is in a metastable state and is susceptible to formation of two-body bound states. Three body processes can therefore lead to depletion of the fermion condensate. Instead of simulating the repulsive Hubbard model by stabilizing the metastable Fermi gas, the associated attractive model can be studied in experiments instead[20].

(v) We discuss a special case of the previous transformation which occurs at half-filling in the absence of a magnetic field ($\mu = B = 0$). The attractive Hubbard model precisely maps onto the repulsive model which is known to possess a Néel ground state. The orientation of Néel order is arbitrary. In the attractive model, this takes the form a global pseudo-spin rotational symmetry[47] at half-filling for any bipartite lattice. To illustrate this symmetry, we define the following pseudospin operators which were first used in the context of superconductivity by Anderson[44],

$$\begin{aligned} T^{+}_{i} &= \eta_i c^{\dagger}_{i\uparrow}c^{\dagger}_{i\downarrow}, \\ T^{-}_{i} &= \eta_i c_{i\downarrow}c_{i\uparrow}, \\ T^{z}_{i} &= \frac{1}{2}(c^{\dagger}_{i\uparrow}c_{i\uparrow} + c^{\dagger}_{i\downarrow}c_{i\downarrow} - 1), \end{aligned} \quad (2.4)$$

where $\eta_i = +1$ on one sublattice and $\eta_i = -1$ on the other sublattice of the square or cubic lattice. The physical meaning of these operators is evident: T^{+}_{i} creates a fermion

pair at site i, T_i^- annihilates a fermion pair at site i, and T_i^z measures deviation of density from half-filling.

It is easily shown that these operators obey usual spin commutation relations. Furthermore, if $\mu = 0$, the global pseudospin operators,

$$\begin{aligned} T^z &= \sum_i T_i^z, \\ T^\pm &= \sum_i T_i^\pm, \end{aligned} \tag{2.5}$$

all commute with the Hubbard Hamiltonian in Eq. 2.1 revealing a global pseudospin SU(2) symmetry at half-filling where $\mu = 0$.

2.1.2 Ground state degeneracy at half-filling

The ground state of Eq. 2.1 on the square/cubic lattice is known to be a uniform superfluid for any choice of U/t and μ/t[41, 42]. The uniform superfluid has an order parameter $\langle c_{i\uparrow}^\dagger c_{i\downarrow}^\dagger \rangle \sim \Delta e^{i\varphi}$ where the phase φ corresponds to a spontaneously broken symmetry. In terms of pseudospin operators, this may be written as $\langle T_i^+ \rangle \sim \eta_i \Delta e^{i\varphi}$. At half-filling, due to the extra pseudospin symmetry, all states which can be obtained by a global pseudospin rotation of the uniform superfluid are also ground states. The ground state manifold can thus be characterized by a vector order parameter $\mathbf{N} = \eta_i \langle \mathbf{T}_i \rangle$ with magnitude Δ which can point in any direction in pseudospin space. We represent this order parameter on the Bloch sphere as shown in Fig. 2.1(a). The uniform superfluid state has $\mathbf{N}$ lying on the equator. The state with $\mathbf{N} \sim \pm\Delta\hat{z}$ points to the north/south pole of the Bloch sphere. This signifies $\langle T_i^z \rangle \sim \pm\eta_i\Delta$, which corresponds to a checkerboard Charge Density Wave (CDW) state. Other locations on the Bloch sphere correspond to states with coexisting CDW and superfluid orders.

Away from half-filling, this degeneracy is broken and the ground state is superfluid. For small $\mu \neq 0$, the energy splitting between the CDW and superfluid states scales linearly with μ. Upon tuning away from half-filling, the CDW is a low-lying excited

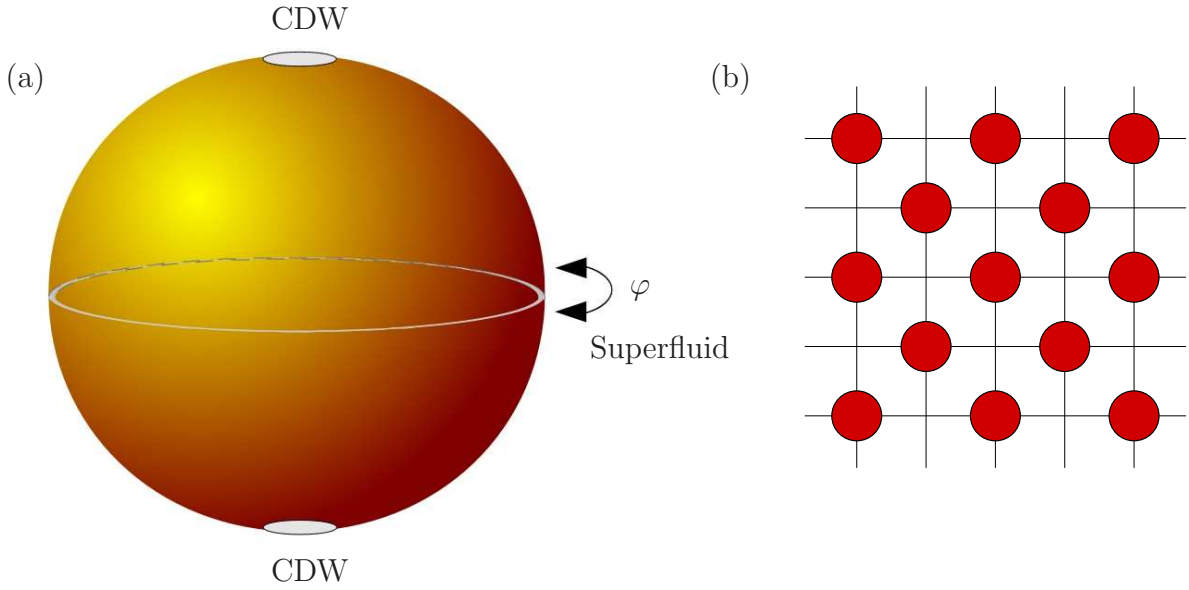

Figure 2.1: (a) The ground state manifold at half-filling. The order parameter can be represented as a vector on a Bloch sphere. The poles correspond to CDW orders. The equator corresponds to superfluid order; each point on the equator represents a choice of the phase of the superfluid order parameter. (b) The two CDW states: sites marked with red squares have higher/lower density than unmarked sites.

state. We expect the collective mode spectrum of the superfluid to reflect the presence of this low-lying competing phase. Indeed, in the following sections, we will identify a 'roton'-like feature in the collective mode spectrum resulting from this weak degeneracy breaking.

2.2 Mean-field theory of superfluid state

As the ground state of the Hubbard model is generically a superfluid, we begin with a mean-field treatment of the superfluid state. We decouple the Hubbard interaction in Eq. 2.1 using the order parameter $U\langle c_{i\downarrow}c_{i\uparrow}\rangle = \Delta_0$, to get

$$H_{\text{MFT}} = -t\sum_{\langle ij\rangle,\sigma}(c^\dagger_{i\sigma}c_{j\sigma} + c^\dagger_{j\sigma}c_{i\sigma}) - \mu\sum_{i\sigma} n_{i\sigma} - \Delta_0\sum_i \left(c^\dagger_{i\uparrow}c^\dagger_{i\downarrow} + c_{i\downarrow}c_{i\uparrow}\right),$$

where we have absorbed the uniform Hartree shift into the chemical potential. In momentum space, the mean field Hamiltonian takes the form

$$H_{\rm MFT} = \sum_{\mathbf{k},\sigma} \xi_{\mathbf{k}} c^\dagger_{\mathbf{k}\sigma} c_{\mathbf{k}\sigma} - \Delta_0 \sum_{\mathbf{k}} \left(c^\dagger_{\mathbf{k}\uparrow} c^\dagger_{-\mathbf{k}\downarrow} + c_{-\mathbf{k}\downarrow} c_{\mathbf{k}\uparrow} \right), \tag{2.6}$$

where $\xi_{\mathbf{k}} \equiv -2t\epsilon_{\mathbf{k}} - \mu$, with $\epsilon_{\mathbf{k}} \equiv \sum_{i=1}^{d} \cos(k_i)$ ($d = 2, 3$ is the dimensionality of the lattice).

We can diagonalize $H_{\rm MFT}$ by defining Bogoliubov quasiparticles (QPs), γ, via

$$\begin{pmatrix} c_{\mathbf{k}\uparrow} \\ c^\dagger_{-\mathbf{k}\downarrow} \end{pmatrix} = \begin{pmatrix} u_{\mathbf{k}} & v_{\mathbf{k}} \\ -v_{\mathbf{k}} & u_{\mathbf{k}} \end{pmatrix} \begin{pmatrix} \gamma_{\mathbf{k}\uparrow} \\ \gamma^\dagger_{-\mathbf{k}\downarrow} \end{pmatrix}. \tag{2.7}$$

Parametrizing $u_{\mathbf{k}} \equiv \cos(\theta_{\mathbf{k}})$, $v_{\mathbf{k}} \equiv \sin(\theta_{\mathbf{k}})$, and demanding that the transformed Hamiltonian be diagonal leads to the condition $\tan(2\theta_{\mathbf{k}}) = \Delta_0/\xi_{\mathbf{k}}$. We denote the eigenvalue of the Hamiltonian matrix by

$$E_{\mathbf{k}} = \sqrt{\xi^2_{\mathbf{k}} + \Delta^2_0}. \tag{2.8}$$

The Bogoliubov transformation coefficients must satisfy the relations

$$u^2_{\mathbf{k}} = \frac{1}{2}\left(1 + \frac{\xi_{\mathbf{k}}}{E_{\mathbf{k}}}\right); \quad v^2_{\mathbf{k}} = \frac{1}{2}\left(1 - \frac{\xi_{\mathbf{k}}}{E_{\mathbf{k}}}\right); \quad u_{\mathbf{k}} v_{\mathbf{k}} = \frac{\Delta_0}{2E_{\mathbf{k}}}. \tag{2.9}$$

In terms of the Bogoliubov QPs, the mean field Hamiltonian finally takes the form

$$H_{\rm MFT} = E_{\rm GS} + \sum_{\mathbf{k}} E_{\mathbf{k}} \gamma^\dagger_{\mathbf{k}\sigma} \gamma_{\mathbf{k}\sigma}, \tag{2.10}$$

where $E_{\rm GS} = \sum_{\mathbf{k}} (E_{\mathbf{k}} - \xi_{\mathbf{k}})$ denotes the ground state energy of $H_{\rm MFT}$. Demanding self-consistency of the mean field theory yields the gap and number equations:

$$\begin{aligned} \frac{1}{U} &= \frac{1}{N} \sum_{\mathbf{k}} \frac{(1 - 2n_F(E_{\mathbf{k}}))}{2E_{\mathbf{k}}}, \\ f &= \frac{2}{N} \sum_{\mathbf{k}} \left[u^2_{\mathbf{k}} n_F(E_{\mathbf{k}}) + v^2_{\mathbf{k}} (1 - n_F(E_{\mathbf{k}})) \right], \end{aligned} \tag{2.11}$$

where f is the filling, i.e. the average number of fermions per site, and N is the total number of sites. $n_F(.)$ denotes the Fermi distribution function. For given U and filling f, these equations can be solved to obtain the superfluid order parameter Δ_0 and the QP spectrum.

2.3 Collective modes at weak-coupling

Going beyond mean field theory, we include fluctuations of the density and the superfluid order parameter within GRPA. We begin by considering fictitious external fields that couple to modulations in density and in the superfluid order parameter:

$$H'_{\rm MFT} = H_{\rm MFT} - \sum_i [h_\rho(i,t)\hat{\rho}_i + h_\Delta(i,t)\hat{\Delta}_i + h^*_\Delta(i,t)\hat{\Delta}^\dagger_i], \tag{2.12}$$

where $\hat{\rho}_i = \frac{1}{2}c^\dagger_{i\sigma}c_{i\sigma}$ and $\hat{\Delta}_i = c_{i\downarrow}c_{i\uparrow}$. Going to momentum space, [1]

$$H' = H_{MFT} - \frac{1}{N}\sum_{\mathbf{K},\beta\in\{1,2,3\}} h_\beta(\mathbf{K},t)\hat{O}^\dagger_\beta(\mathbf{K}), \tag{2.13}$$

where $\hat{\mathbf{O}}^\dagger(\mathbf{K}) \equiv \{\hat{\rho}_{-\mathbf{K}}, \hat{\Delta}_{-\mathbf{K}}, \hat{\Delta}^\dagger_{\mathbf{K}}\}$ is the vector of fermion bilinear operators corresponding to modulations in density and superfluid order at nonzero momenta. The modulation operators are given by:

$$\begin{aligned}
\hat{\rho}_{\mathbf{K}} &\equiv \tfrac{1}{2}\textstyle\sum_{\mathbf{k}} c^\dagger_{\mathbf{k}\sigma}c_{\mathbf{k}+\mathbf{K}\sigma}, & h_1(\mathbf{K},t) &= h_\rho(\mathbf{K},t),\\
\hat{\Delta}_{\mathbf{K}} &\equiv \textstyle\sum_{\mathbf{k}} c_{-\mathbf{k}+\mathbf{K}\downarrow}c_{\mathbf{k}\uparrow}, & h_2(\mathbf{K},t) &= h_\Delta(\mathbf{K},t),\\
\hat{\Delta}^\dagger_{\mathbf{K}} &\equiv \textstyle\sum_{\mathbf{k}} c^\dagger_{\mathbf{k}\uparrow}c^\dagger_{-\mathbf{k}+\mathbf{K}\downarrow}, & h_3(\mathbf{K},t) &= h^*_\Delta(-\mathbf{K},t).
\end{aligned}$$

2.3.1 Bare Susceptibility

We treat these perturbing fields within first order in perturbation theory. The expectation value of a modulation field is given by

$$\langle\hat{O}_\alpha\rangle(\mathbf{K},t) = \int_{-\infty}^{+\infty} dt'\ \chi^0_{\alpha\beta}(\mathbf{K},t-t')h_\beta(\mathbf{K},t'), \tag{2.14}$$

where

$$\chi^0_{\alpha\beta}(\mathbf{K},t-t') = \frac{i\Theta(t-t')}{N}\langle\Big[\hat{O}_\alpha(\mathbf{K},t),\hat{O}^\dagger_\beta(\mathbf{K},t')\Big]\rangle_0. \tag{2.15}$$

Here $[.,.]$ denotes the commutator and $\langle.\rangle_0$ implies that the expectation value is taken in the ground state of H_0.

[1] We use the Fourier transform conventions: $c_{i\sigma} = \frac{1}{\sqrt{N}}\sum_{\mathbf{k}} c_{\mathbf{k}\sigma}e^{i\mathbf{k}.\mathbf{r_i}}.$; which defines $(\hat{\rho}/\hat{\Delta})_i = \frac{1}{N}\sum_{\mathbf{K}}(\hat{\rho}/\hat{\Delta})_{\mathbf{K}}e^{i\mathbf{K}.\mathbf{r_i}}$. For the perturbing fields, we use $h_{\rho/\Delta}(i,t) = \frac{1}{N}\int\frac{d\omega}{2\pi}\sum_{\mathbf{q}} h_{\rho/\Delta}(\mathbf{q},\omega)e^{i(\mathbf{q}\cdot\mathbf{r}_i-\omega t)}$.

In frequency domain, the susceptibility matrix is given by

$$\langle \hat{O}_\alpha(\mathbf{K},\omega)\rangle = \chi^0_{\alpha\beta}(\mathbf{K},\omega) h_\beta(\mathbf{K},\omega), \tag{2.16}$$

where

$$\chi^0_{\alpha\beta}(\mathbf{K},\omega) = \frac{1}{N}\sum_n \left(\frac{(\hat{O}^\dagger_\beta)_{0n}(\hat{O}_\alpha)_{n0}}{\omega + E_{n0} + i0^+} - \frac{(\hat{O}_\alpha)_{0n}(\hat{O}^\dagger_\beta)_{n0}}{\omega - E_{n0} + i0^+} \right). \tag{2.17}$$

The index n sums over all excited states of the mean-field Hamiltonian. We have denoted $(\hat{O})_{mn} \equiv \langle m|\hat{O}|n\rangle$, wherein $|n\rangle, |m\rangle$ are eigenstates of H_{MFT} (with $n=0$ corresponding to the ground state). In the denominator, $E_{n0} \equiv E_n – E_0$ where E_n is the energy of state $|n\rangle$.

The excited states of the mean-field Hamiltonian are given by the Fock space of Bogoliubov quasiparticles. The operators $\hat{O}_\alpha$ and $\hat{O}^\dagger_\beta$ are composed of quasiparticle bilinears. At zero temperature, the only intermediate states which contribute to $\chi^0_{\alpha\beta}(\mathbf{K},\omega)$ are those with two quasiparticle excitations. We give explicit expressions for the entries in $\chi^0_{\alpha\beta}(\mathbf{K},\omega)$, which we call the 'bare susceptibility' matrix, in Appendix A.1.

2.3.2 Generalized Random Phase Approximation (GRPA)

The bare susceptibility evaluated in the previous section will be renormalized by the interaction term. The interaction term in the Hamiltonian may be decomposed as follows:

$$-U c^\dagger_{i\uparrow} c^\dagger_{i\downarrow} c_{i\downarrow} c_{i\uparrow} \rightarrow -U\Big[\langle c^\dagger_{i\uparrow} c_{i\uparrow}\rangle c^\dagger_{i\downarrow} c_{i\downarrow} + \langle c^\dagger_{i\downarrow} c_{i\downarrow}\rangle c^\dagger_{i\uparrow} c_{i\uparrow}\Big] - U\Big[\langle c^\dagger_{i\uparrow} c^\dagger_{i\downarrow}\rangle c_{i\downarrow} c_{i\uparrow} + \langle c_{i\downarrow} c_{i\uparrow}\rangle c^\dagger_{i\uparrow} c^\dagger_{i\downarrow}\Big] \tag{2.18}$$

These expectation values act as "internal fields" which renormalize the applied field. We take these internal fields into account by setting

$$\begin{aligned} h_1(\mathbf{K},\omega) &\rightarrow h_1(\mathbf{K},\omega) + 2U\langle \hat{O}_1(\mathbf{K},\omega)\rangle, \\ h_2(\mathbf{K},\omega) &\rightarrow h_2(\mathbf{K},\omega) + U\langle \hat{O}_2(\mathbf{K},\omega)\rangle, \\ h_3(\mathbf{K},\omega) &\rightarrow h_3(\mathbf{K},\omega) + U\langle \hat{O}_3(\mathbf{K},\omega)\rangle. \end{aligned} \tag{2.19}$$

With these renormalized fields, the expectation value of the modulation fields becomes:

$$\langle \hat{O}_\alpha\rangle = \chi^0_{\alpha\beta}(h_\beta + U D_{\beta\tau}\langle \hat{O}_\tau\rangle), \tag{2.20}$$

where $D \equiv \text{Diag}\{2,1,1\}$ is a diagonal matrix, and we have suppressed $(\mathbf{K},\omega)$ labels for notational simplicity. Rearranging the above equation gives:

$$\langle \hat{O}_\alpha \rangle = [(1 - U\chi^0 D)^{-1}\chi^0]_{\alpha\beta}\ h_\beta \equiv \chi^{GRPA}_{\alpha\beta} h_\beta. \tag{2.21}$$

This gives us the GRPA susceptibility. We call this the Generalized Random Phase Approximation after Anderson[44].

This GRPA susceptibility will diverge when the determinant $\text{Det}(1-U\chi^0 D)$ becomes zero (or equivalently, one of the eigenvalues of this matrix vanishes). This indicates that a modulation mode will acquire a non-zero expectation value, even in the presence of an infinitesimal external field. We identify the locus of real frequencies ($\omega \equiv \omega(\mathbf{K})$) at which such spontaneous modulation fields arise, as the dispersion of a sharp (undamped) collective mode.

The above GRPA prescription is perturbative in interaction corrections, and is justified in the weak coupling limit. To test its regime of validity, we juxtapose this prescription with a strong coupling analysis in the following section.

2.4 Strong Coupling Limit: Spin Wave Analysis of Pseudospin Model

In the strong coupling limit, the attractive Hubbard model of Eq. 2.1 reduces to the S=1/2 Heisenberg model in the pseudospin operators (see Appendix A.2 for derivation),

$$H_{pseudospin} = J \sum_{\langle ij \rangle} \mathbf{T}_i \cdot \mathbf{T}_j - \mu \sum_i T^z_i, \tag{2.22}$$

with $J = 4t^2/U$. The uniform stationary superfluid is described by antiferromagnetic ordering in the XY plane. Deviation from half-filling manifests as uniform canting away from the XY plane. (The CDW state corresponds to antiferromagnetic ordering along the z axis.) The collective modes of a magnetically ordered state are naturally described

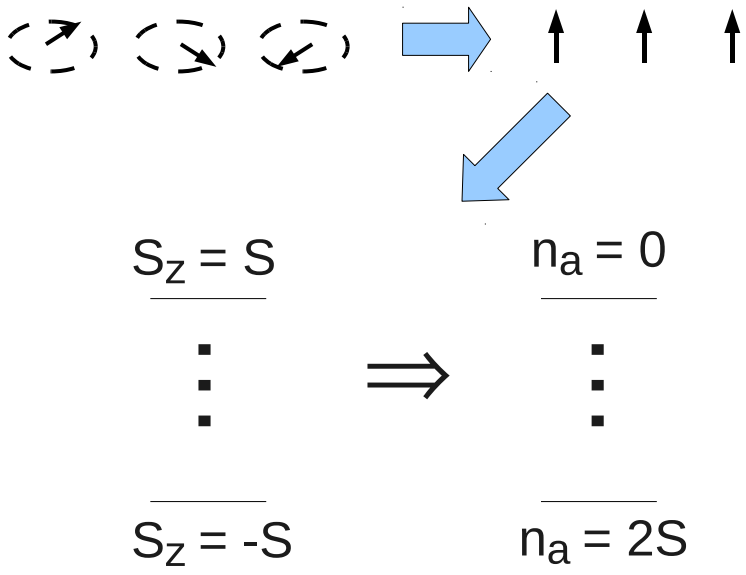

Figure 2.2: Holstein Primakoff spin wave calculation: The spiral state is first transformed into a ferromagnet by a local spin rotation. In the ferromagnet, the Hilbert space of each spin into mapped to a bosonic state which can be occupied by 0-2S bosons. These bosons acquire a dispersion on the lattice - giving the quantized spin wave mode energies.

by the Holstein-Primakoff approach[48] (see Fig. 2.2). Although this approach is strictly valid in the large S limit, it is known to work well even for $S = 1/2$ systems[49, 50]. We begin by treating the pseudospins as classical vectors, and subsequently add quantum corrections. The ground state in the classical limit $|0\rangle_c$ may be parametrizing as

$$T_i^c \equiv S(\eta_i \sin\theta, 0, \cos\theta), \tag{2.23}$$

where $S = 1/2$ is the pseudospin magnitude. The pseudospins T_i^c form a canted antiferromagnet. The canting angle θ is related to the filling by

$$f - 1 = \cos\theta. \tag{2.24}$$

where f is the average number of fermions per site. To use the Holstein-Primakoff prescription, we first perform a site-dependent spin rotation into a ferromagnetic state. We

define new pseudospin operators $\tilde{\mathbf{T}}$ given by

$$\begin{aligned} \tilde{T}_i^z &= T_i^z \cos(\theta) + \eta_i T_i^x \sin(\theta), \\ \tilde{T}_i^x &= -T_i^z \sin(\theta) + \eta_i T_i^x \cos(\theta), \\ \tilde{T}_i^y &= \eta_i T_i^y, \end{aligned} \tag{2.25}$$

In terms of these operators, the classical ground state is a ferromagnet with pseudospins pointing towards the Z axis. We replace the $\tilde{\mathbf{T}}$ operators with Holstein-Primakoff bosons. By setting terms that are linear in the boson operators to zero, we obtain μ as a function of θ.

$$\mu = 4JS\cos(\theta)\epsilon_0, \tag{2.26}$$

where $\epsilon_{\mathbf{k}} \equiv \sum_{i=1}^{d} \cos(k_i)$ as defined in Sec. 2.2.

The Hamiltonian to $\mathcal{O}(S)$ in terms of Holstein-Primakoff bosons, is given by

$$H = E_{\rm c} + \delta E + \sum_{\mathbf{K}} \omega_{\mathbf{K}} b_{\mathbf{K}}^\dagger b_{\mathbf{K}}, \tag{2.27}$$

where ($E_{\rm c} = -NJS^2\epsilon_0[1 + 2\cos^2\theta]$) is the classical ground state energy and ($\delta E = JS\cos^2\theta \sum_{\mathbf{K}} \epsilon_{\mathbf{K}}$) is the leading quantum correction. The spin-wave dispersion $\omega_{\mathbf{K}}$ is given by

$$\omega_{\mathbf{K}} = 2JS + \sqrt{\alpha_{\mathbf{K}}^2 - \gamma_{\mathbf{K}}^2}, \tag{2.28}$$

with $\alpha_{\mathbf{K}} = \epsilon_0 - \cos^2\theta\epsilon_{\mathbf{K}}$ and $\gamma_{\mathbf{K}} = \sin^2\theta\epsilon_{\mathbf{K}}$.

An illustration of the collective mode dispersions obtained using this approach is shown in Fig. 2.3 at strong coupling ($U/t = 15$) for two different fillings, $f = 0.8, 1.0$ fermions per site. These spin wave dispersions are in very good agreement with the collective mode frequency obtained using GRPA. We find better and better agreement as U/t is increased. Thus, the GRPA formalism also correctly captures the strong coupling limit. Given that GRPA works well both in the weak-coupling limit and in the strong-coupling limit, it is likely that GRPA gives reliable results for all interaction strengths.

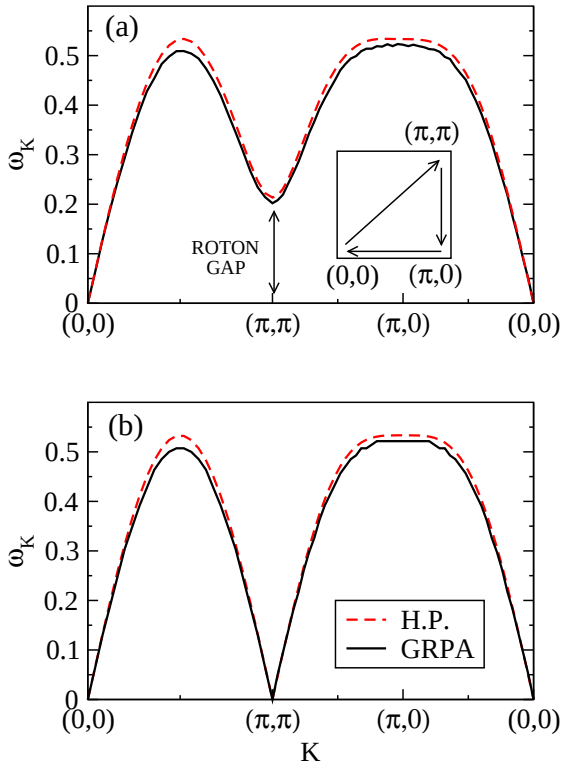

Figure 2.3: Collective mode energy at zero superflow in 2D at strong coupling, $U/t = 15$. The dispersion is shown along the indicated contour in the Brillouin zone for a filling of (a) $f = 0.8$ fermions per site and (b) $f = 1.0$ per site. The GRPA result (solid line) is in good agreement (within 10%) with the Holstein-Primakoff spin wave result (dashed line, HP) for the strong coupling pseudospin model. The roton minimum (see Section 2.5)has a small gap at $f = 0.8$ but becomes a gapless mode at $f = 1.0$ due to the pseudospin SU(2) symmetry discussed in the text.

2.5 Features of the collective mode

Fig. 2.4 provides an illustrative example of the collective mode spectrum obtained using GRPA. We highlight two features:

(i) A linearly dispersing "phonon" mode occurs at small momenta and low energy. The slope of this linear dispersion is the sound velocity.

(ii) An extremum occurs at the corner of the Brillouin zone, due to symmetry reasons.

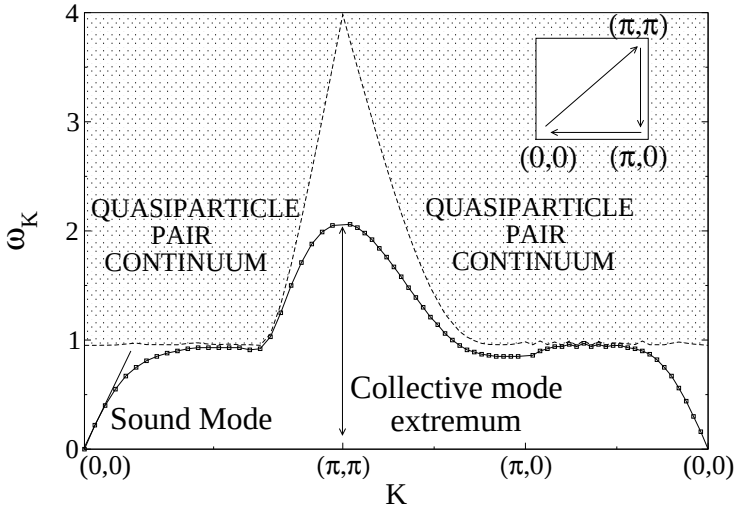

Figure 2.4: Illustrative example of the collective mode dispersion and quasiparticle-pair continuum in 2D, for zero superflow ($\mathbf{Q} = 0$) with $U/t = 3$ and $f = 0.2$ fermions per site, along the contour displayed in the inset.

In Fig. 2.4, the collective mode has a maximum at $\mathbf{K} = (\pi, \pi)$. At fillings closer to $f = 1$, the spectrum exhibits a minimum at $\mathbf{K} = (\pi, \pi)$. This minimum indicates a tendency towards checkerboard density order, reflecting the presence of a low-lying CDW mode. Indeed, the minimum touches zero at half-filling (see Fig. 2.3), on account of the degeneracy between superfluid and CDW phases. We call this mode a 'roton' in analogy with liquid ^{4}He. Unlike ^{4}He however, this feature occurs at the Brillouin zone corner only and does not form a ring of wavevectors.

We plot our results for the sound velocity and the roton gap in Fig. 2.5. We hope that cold-atom experiments will be able to verify these predictions.

At high energies, there is an onset of a two-quasiparticle continuum where the collective mode can decay by creating two Bogoliubov quasiparticles with opposite spins in a manner which conserves energy and momentum. Once the collective mode energy goes above the lower edge of the two-particle continuum of Bogoliubov QP excitations, it ceases to be a sharp excitation and acquires a finite lifetime.

2.6 Summary and Discussion

We have studied the collective mode spectrum of the attractive Hubbard model using the GRPA formalism. In the limit of strong coupling, we have developed an effective pseudospin model; collective mode excitations at strong coupling correspond to spin waves in this pseudospin model. The GRPA result at strong coupling is in very good quantitative agreement with the spin wave analysis, indicating that GRPA correctly captures the strong coupling physics as well. Having thus gained confidence in the GRPA formalism, we have characterized the collective mode spectrum as a function of interaction strength, density and dimensionality. We have presented results for sound velocity and roton gap, which we hope can be experimentally measured in the near future.

Our results are in good agreement with several recent calculations using various methods. A strong-coupling treatment in the presence of superflow has been presented in Ref.[51]. Two recent articles, Ref.[52](using diagrammatics) and Ref.[53](using the Bethe-Salpeter equation), have studied the collective mode in a flowing superfluid. Our results are in good agreement with all of these reports.

Close to half-filling, there is a low-lying CDW phase which competes with the superfluid ground state. This low-lying state manifests as a minimum of the collective mode at the Brillouin zone corner - (π, π) in two dimensions and (π, π, π) in three dimensions. This roton mode is a unique feature of the attractive Hubbard model and is an interesting manifestation of competing orders. At half-filling, the superfluid ground state is degenerate with the CDW phase making the roton mode gapless. A promising avenue to verify our findings experimentally is Bragg spectroscopy which measures the density-density response function. This measurement has been successfully performed in the case of a two-component Fermi gas with Galilean invariance[54]. In fact, this has been shown to be in excellent agreement with RPA results[55]. In this measurement, two counter-propagating laser beams set up a shallow optical lattice on top of a trapped Fermi gas. One of the lasers is slightly detuned to produce a running lattice. Fermions

can absorb a photon from one lattice beam and emit into another - the energy imparted to the Fermi gas is fixed by the detuning of lattice lasers while the momentum imparted is given by the period of the shallow optical lattice. By measuring the centre-of-mass momentum imparted to the cloud of fermions, the density-density response can be evaluated. For the case of the attractive Hubbard model, we expect that a shallow running lattice can be superimposed on the optical lattice potential without mixing higher bands. The collective mode spectrum can thus be mapped as a function of momentum.

In Chapter3, we discuss the collective mode spectrum in the presence of an imposed superfluid flow and explore flow-induced breakdown of superfluidity. Superflow instabilities also serve as a probe of collective excitations.

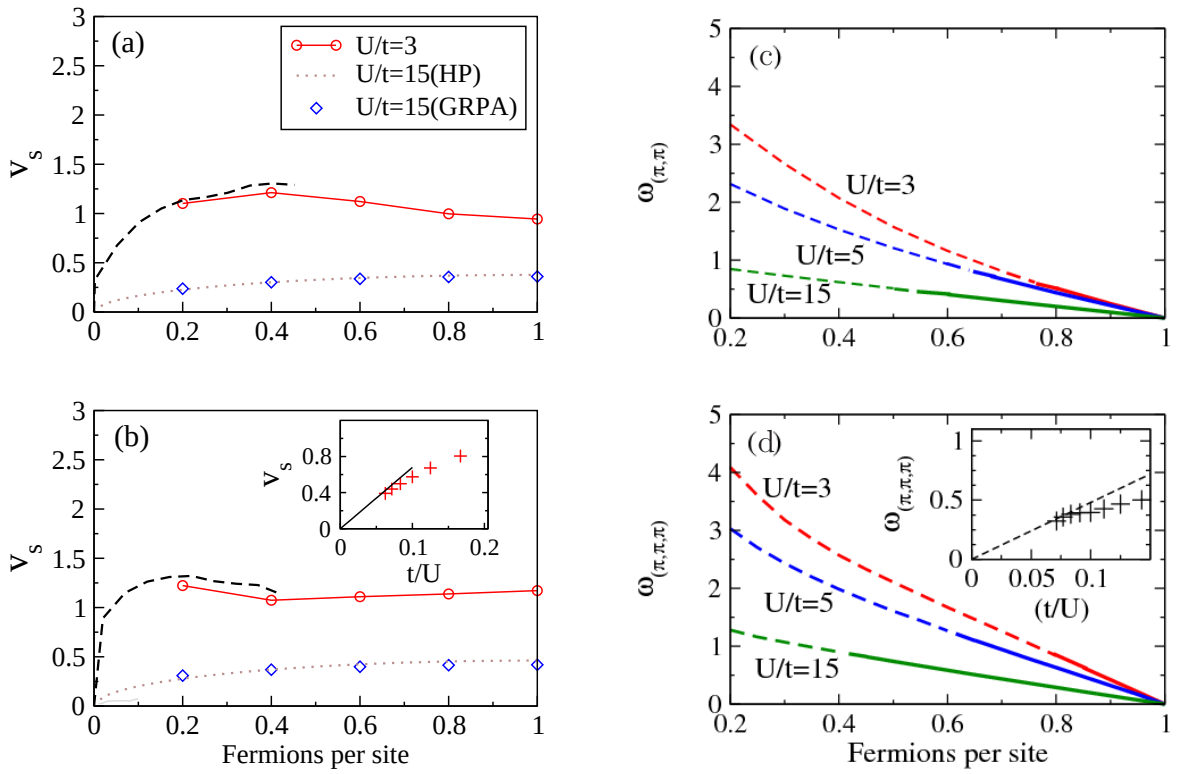

Figure 2.5: Left: Sound mode velocity, v_s, as a function of the fermion filling f in (a) 2D and (b) 3D for $U/t = 3, 15$. Solid line is a guide to the eye. The dashed lines are the weak coupling result, $v_s = (v_F/\sqrt{d})[1 - UN(0)]^{1/2}$, from Ref.[43] for $U/t = 3$, with $N(0)$ being the non-interacting density of states (per spin) at the Fermi level. The dotted line indicates the Holstein Primakoff spin-wave result for $U/t = 15$. The inset to (b) shows the expected t/U scaling of v_s/t for $U/t \gg 1$. Right: The roton gap at (c) (π, π) in 2D and (d) (π, π, π) in 3D for different interaction strengths. The dashed (solid) lines indicate that the mode energy corresponds to a local maximum (minimum) of the dispersion. The inset shows the roton gap in 3D at a filling of $f = 0.8$ fermions per site, as a function of t/U. Inset shows a comparison of the GRPA result (points) with the strong coupling spin-wave theory result (dashed line).

Chapter 3

Superflow instabilities in the attractive Hubbard model

3.1 Introduction

Chapter 2 evaluates the collective mode spectrum in the superfluid phase of the attractive Hubbard model. Close to half-filling, there is a low-lying CDW mode which manifests as a roton-like excitation. In this chapter, we use imposed superflow as a tool to induce competition between superfluid and CDW phases. As caricatured in Fig. 3.1, imposed flow raises the energy of the superfluid state. When the energy cost of flow overwhelms the energy difference between the superfluid and CDW phases, the system may prefer to switch to the insulating CDW phase. Alternatively, a novel coexistence phase could result when superflow makes the energies of the two states comparable. Such a 'supersolid' phase has long been sought in various systems[56, 57].

The critical velocity of a superfluid is a classic problem which has been studied in many contexts. Chapter 1 gives a brief overview. Superflow in the attractive Hubbard model is a natural extension of the accumulated body of work on this question. Earlier work has identified various mechanisms of superfluid breakdown in Bose gases, lattice

bosons and Fermi gases. The attractive Hubbard model exhibits all of these breakdown mechanisms; furthermore, it gives rise to new instabilities that are not present in earlier systems. In this chapter, we will classify various superflow instabilities in the attractive Hubbard model. At the end of this chapter, we will plot 'stability phase diagrams' which indicate the leading instability as a function of dimensionality, interaction strength and density.

We begin this chapter with the mean-field theory of the flowing superfluid. We then calculate the collective mode spectrum using GRPA and the strong coupling pseudospin model. Imposed superflow renormalizes the mean-field parameters as well as the collective mode spectrum. At the critical flow velocity, the superfluid becomes unstable which can be seen from the mean-field theory and/or the collective mode spectrum. We identify three categories of instabilities, which we call "depairing", "Landau" and "dynamical". In the following sections, we describe each of these and map out stability phase diagrams.

From the point of view of cold-atom experiments, the case of dynamical instabilities is the most interesting. We find two qualitatively different kinds of dynamical instabilities: commensurate and incommensurate. The commensurate instability is a manifestation of flow-induced competition between superfluidity and CDW order. It is associated with the exponential growth of checkerboard CDW fluctuations. We investigate the fate of the system beyond this instability by performing an extended mean-field analysis allowing for both orders. The mean-field theory shows a coexistence phase which however, appears to be unstable to long wavelength fluctuations. The incommensurate instability is an intermediate-density, intermediate-interaction-strength phenomenon which is a novel finding of our study. We understand this instability in analogy with exciton condensation in semiconductors. We end this chapter with implications for cold atoms experiments.

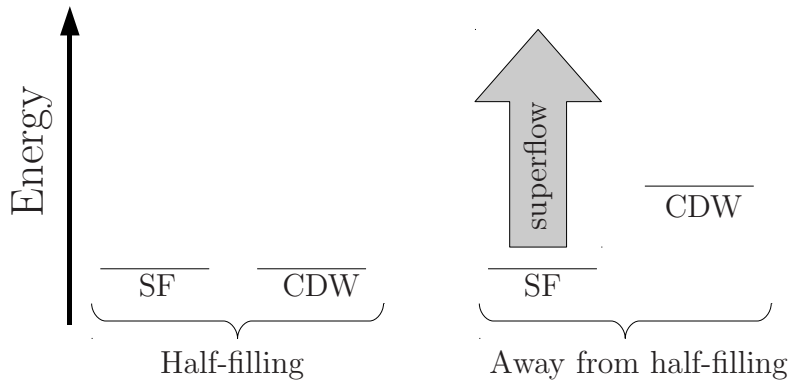

Figure 3.1: Dynamical commensurate instability: Competition between superfluid(SF) and CDW states. Left: At half-filling, the two states are degenerate. Right: Away from half-filling, the SF is lower in energy. As indicated by the arrow, imposed superflow raises the energy of the superfluid state and forces competition with CDW order.

3.2 Mean-field theory of the flowing superfluid

The flowing superfluid state is composed of Cooper pairs with non-zero momentum. The Hubbard interaction is decoupled using the order parameter $U\langle c_{i\downarrow}c_{i\uparrow}\rangle = \Delta_0 e^{i\mathbf{Q}\cdot\mathbf{r}_i}$. In this state, the superfluid order parameter has a uniform amplitude and a winding phase. As superflow is imposed, we expect the stationary superfluid to adiabatically evolve into this state. For simplicity, we restrict our attention to superflow momenta $\mathbf{Q} = Q_x\hat{x}$. The mean-field Hamiltonian in momentum space takes the form

$$H_{\mathrm{MFT}} = \sum_{\mathbf{k},\sigma} \xi_{\mathbf{k}} c^\dagger_{\mathbf{k}\sigma} c_{\mathbf{k}\sigma} - \Delta_0 \sum_{\mathbf{k}} \left(c^\dagger_{\mathbf{k}\uparrow} c^\dagger_{-\mathbf{k}+\mathbf{Q}\downarrow} + c_{-\mathbf{k}+\mathbf{Q}\downarrow} c_{\mathbf{k}\uparrow} \right), \tag{3.1}$$

where $\xi_{\mathbf{k}} \equiv -2t\epsilon_{\mathbf{k}} - \mu$, with $\epsilon_{\mathbf{k}} \equiv \sum_{i=1}^{d} \cos(k_i)$ ($d = 2, 3$ is the dimensionality of the lattice).

We can diagonalize H_{MFT} by defining Bogoliubov quasiparticles (QPs), γ, via

$$\begin{pmatrix} c_{\mathbf{k}\uparrow} \\ c^\dagger_{-\mathbf{k}+\mathbf{Q}\downarrow} \end{pmatrix} = \begin{pmatrix} u_{\mathbf{k}}(\mathbf{Q}) & v_{\mathbf{k}}(\mathbf{Q}) \\ -v_{\mathbf{k}}(\mathbf{Q}) & u_{\mathbf{k}}(\mathbf{Q}) \end{pmatrix} \begin{pmatrix} \gamma_{\mathbf{k}\uparrow} \\ \gamma^\dagger_{-\mathbf{k}+\mathbf{Q}\downarrow} \end{pmatrix}. \tag{3.2}$$

Demanding that the Hamiltonian be diagonal in terms of the new QP operators leads to

$$u^2_{\mathbf{k}}(\mathbf{Q}) = \frac{1}{2}\left(1 + \frac{\xi_{\mathbf{k}} + \xi_{-\mathbf{k}+\mathbf{Q}}}{2\Gamma_{\mathbf{k},\mathbf{Q}}}\right); \quad v^2_{\mathbf{k}}(\mathbf{Q}) = \frac{1}{2}\left(1 - \frac{\xi_{\mathbf{k}} + \xi_{-\mathbf{k}+\mathbf{Q}}}{2\Gamma_{\mathbf{k},\mathbf{Q}}}\right); \quad u_{\mathbf{k}}(\mathbf{Q})v_{\mathbf{k}}(\mathbf{Q}) = \frac{\Delta_0}{2\Gamma_{\mathbf{k},\mathbf{Q}}} \tag{3.3}$$

where we have defined

$$\Gamma_{\mathbf{k},\mathbf{Q}} = \sqrt{\frac{1}{4}(\xi_{\mathbf{k}} + \xi_{-\mathbf{k}+\mathbf{Q}})^2 + \Delta_0^2}. \tag{3.4}$$

The transformed mean field Hamiltonian is given by

$$H_{\mathrm{MFT}} = E_{\mathrm{GS}} + \sum_{\mathbf{k}} E_{\mathbf{k}} \gamma^\dagger_{\mathbf{k}\sigma}\gamma_{\mathbf{k}\sigma}, \tag{3.5}$$

where E_{GS} denotes the ground state energy of H_{MFT} and $E_{\mathbf{k}}$ denotes the Bogoliubov QP dispersion given by:

$$\begin{aligned} E_{\mathbf{k}} &= \Gamma_{\mathbf{k},\mathbf{Q}} + \frac{1}{2}\left(\xi_{\mathbf{k}} - \xi_{-\mathbf{k}+\mathbf{Q}}\right), \\ E_{\mathrm{GS}} &= \sum_{\mathbf{k}} \left(E_{\mathbf{k}} - \xi_{\mathbf{k}}\right). \end{aligned} \tag{3.6}$$

The self-consistency of the mean field theory yields the gap and number equations:

$$\begin{aligned} \frac{1}{U} &= \frac{1}{N}\sum_{\mathbf{k}} \frac{1}{2\Gamma_{\mathbf{k},\mathbf{Q}}}(1 - n_F(E_{\mathbf{k}}) - n_F(E_{-\mathbf{k}+\mathbf{Q}})), \\ f &= \frac{2}{N}\sum_{\mathbf{k}} \left[u^2_{\mathbf{k}}(\mathbf{Q}) n_F(E_{\mathbf{k}}) + v^2_{\mathbf{k}}(\mathbf{Q})(1 - n_F(E_{-\mathbf{k}+\mathbf{Q}}))\right], \end{aligned} \tag{3.7}$$

where f is the filling, i.e. the average number of fermions per site, and N is the total number of sites. Given the interaction strength, chemical potential and the flow momentum, these equations can be self-consistently solved to obtain the pairing amplitude Δ and the filling.

$n_F(.)$ denotes the Fermi distribution function. At the level of mean-field theory, the effect of flow is twofold - to renormalize the order parameter Δ_0 and to modify the QP dispersion.

3.3 Collective modes of the flowing superfluid

The effect of imposed flow on the collective mode spectrum is best understood in the strong coupling limit. We first discuss the strong-coupling spin wave description of the

collective mode. We then extend our GRPA prescription to the case of the flowing superfluid.

3.3.1 Strong coupling limit

In the strong coupling limit, the attractive Hubbard model reduces to the spin-1/2 Heisenberg model in pseudospin operators (see Appendix A.2 for derivation),

$$H_{pseudospin} = J \sum_{\langle ij \rangle} \mathbf{T}_i \cdot \mathbf{T}_j - \mu \sum_i T_i^z, \tag{3.8}$$

with $J = 4t^2/U$. The pseudospin operators are defined as (see Chapter 2)

$$\begin{aligned} T_i^+ &= \eta_i c_{i\uparrow}^\dagger c_{i\downarrow}^\dagger, \\ T_i^- &= \eta_i c_{i\downarrow} c_{i\uparrow}, \\ T_i^z &= \frac{1}{2}(c_{i\uparrow}^\dagger c_{i\uparrow} + c_{i\downarrow}^\dagger c_{i\downarrow} - 1), \end{aligned} \tag{3.9}$$

where $\eta_i = \pm 1$ on the two sublattices of the square or cubic lattice. The ground state of this Heisenberg model has Néel order and can be represented as

$$\langle \eta_i \mathbf{T}_i \rangle = \mathcal{O}. \tag{3.10}$$

The vector $\mathcal{O}$ is the Néel vector which gives the amplitude and orientation of Néel ordering. From the definition of the pseudospin operators, we see that Néel ordering in the XY plane corresponds to a uniform stationary superfluid state. The phase of this superfluid phase is given by the orientation of the Néel vector within the plane.

An imposed superflow forces the phase of the order parameter to wind with a wavevector $\mathbf{Q}$. In the strong coupling picture, the Néel vector winds within the XY plane forming a spiral with wavevector $\mathbf{Q}$. The resulting state can be obtained by a phase twist on the stationary superfluid, denoted as $|0\rangle$, as follows

$$|\mathbf{Q}\rangle = \exp\left[-i \sum_i T_i^z \mathbf{Q} \cdot \mathbf{r}_i\right] |0\rangle. \tag{3.11}$$

By this operation, the pseudospin vector at each site is rotated in the XY plane by an angle given by $\mathbf{Q}\cdot\mathbf{r}_i$. This forces the Néel vector at each site to spiral with a pitch given by $\mathbf{Q}$. Instead of dealing with this spiral state directly, we absorb the phase twist operator into the Hamiltonian to get

$$H_{\rm eff}(\mathbf{Q}){=}J\sum_{\langle ij\rangle}[T_i^zT_j^z+(T_i^xT_j^x+T_i^yT_j^y)\cos(\mathbf{Q}\cdot\mathbf{r}_{ij})-(T_i^xT_j^y-T_i^yT_j^x)\sin(\mathbf{Q}\cdot\mathbf{r}_{ij})]-\mu\sum_i T_i^z,$$

where $\mathbf{r}_{ij}\equiv\mathbf{r}_i-\mathbf{r}_j$. By this transformation, we have reverted to the rest frame of the superfluid. While we can use the eigenstates of the stationary superfluid, energy expectation values should be evaluated using this 'flowing' Hamiltonian. In the rest frame, the pseudospins possess canted antiferromagnetic order. The out-of-plane canting corresponds to deviation from half-filling. The pseudospin vector at a lattice site i may be characterized as

$$T_i^c\equiv S(\eta_i\sin\theta,0,\cos\theta), \tag{3.12}$$

As described in Eq.2.25 of Chapter 2, we perform a site-dependent pseudospin rotation into a ferromagnetic state with spins pointing along the Z axis. To study the collective excitations, we introduce Holstein-Primakoff bosons. Demanding that the terms linear in boson operators should vanish, we obtain

$$\cos(\theta)=\frac{\mu}{2JS(\epsilon_0+\epsilon_{\mathbf{Q}})}, \tag{3.13}$$

where $\epsilon_{\mathbf{Q}}\equiv\sum_{i=1}^d\cos(Q_i)$ and $S=1/2$.

The Hamiltonian to $\mathcal{O}(S)$ in terms of Holstein-Primakoff bosons, is given by

$$H \;=\; E_{\rm c}+\delta E_{\rm q}+\sum_{\mathbf{K}}\omega_{\mathbf{K}}(\mathbf{Q})b_{\mathbf{K}}^\dagger b_{\mathbf{K}}, \tag{3.14}$$

where

$$\begin{aligned}E_{\rm c} &= -NJS^2[\cos^2\theta\epsilon_0+(1+\cos^2\theta)\epsilon_{\mathbf{Q}}],\\ \delta E_{\rm q} &= -\frac{JS}{2}\sum_{\mathbf{K}}[\epsilon_{\mathbf{K}}\sin^2\theta-\frac{(1+\cos^2\theta)}{2}(\epsilon_{\mathbf{K}+\mathbf{Q}}+\epsilon_{\mathbf{K}-\mathbf{Q}})],\end{aligned} \tag{3.15}$$

represent, respectively, the classical ground state energy and the leading quantum correction. The spin-wave dispersion $\omega_{\mathbf{K}}(\mathbf{Q})$ is given by

$$\omega_{\mathbf{K}}(\mathbf{Q}) = 2JS\left\{\beta_{\mathbf{K}}(\mathbf{Q}) + \sqrt{\alpha^2_{\mathbf{K}}(\mathbf{Q}) - \gamma^2_{\mathbf{K}}(\mathbf{Q})}\right\}, \tag{3.16}$$

with

$$\begin{aligned}
\alpha_{\mathbf{K}}(\mathbf{Q}) &= \epsilon_{\mathbf{Q}} + \frac{\sin^2\theta}{2}\epsilon_{\mathbf{K}} - \frac{(1+\cos^2\theta)}{2}\left(\frac{\epsilon_{\mathbf{K}+\mathbf{Q}}+\epsilon_{\mathbf{K}-\mathbf{Q}}}{2}\right), \\
\beta_{\mathbf{K}}(\mathbf{Q}) &= \frac{1}{2}\cos\theta\left(\epsilon_{\mathbf{K}-\mathbf{Q}} - \epsilon_{\mathbf{K}+\mathbf{Q}}\right), \\
\gamma_{\mathbf{K}}(\mathbf{Q}) &= \frac{1}{4}\sin^2\theta\left(2\epsilon_{\mathbf{K}} + \epsilon_{\mathbf{K}+\mathbf{Q}} + \epsilon_{\mathbf{K}-\mathbf{Q}}\right).
\end{aligned} \tag{3.17}$$

Comparing the spin wave dispersion for the flowing superfluid with the stationary case (obtained by setting $\mathbf{Q} = 0$), we see that imposed flow alters the dispersion in two ways:

(i) The term $\beta_{\mathbf{k}}$ constitutes a 'Doppler-shift'. This term clearly vanishes in the absence of flow. In addition, this term vanishes at special points on the Brillouin zone which satisfy $2\mathbf{K} \equiv 0$. In particular, it vanishes at the wavevector corresponding to checkerboard CDW order (the Brillouin zone corner).

(ii) The term $\sqrt{\alpha^2_{\mathbf{K}}(\mathbf{Q}) - \gamma^2_{\mathbf{K}}(\mathbf{Q})}$ represents an additional renormalization of the collective mode energy. This effect results from the underlying lattice structure and does not occur in systems with Galilean invariance (see Appendix B.1 and Ref.[27]).

For small flow momentum, the former gives a correction that is linear in Q while the latter gives a correction that is quadratic. Thus, at small Q, the Doppler shift is the dominant correction to the collective mode energy. For all interaction strengths, the impact of flow on the collective mode can be understood in terms of these two effects.

3.3.2 Collective modes from GRPA

The GRPA calculation of collective modes in the flowing superfluid closely mirrors the calculation in the stationary case in Chapter 2. We consider fictitious external fields that

couple to modulations in density and in the superfluid order parameter:

$$H'_{\rm MFT} = H_{\rm MFT} - \sum_i [h_\rho(i,t)\hat{\rho}_i + h_\Delta(i,t)\hat{\Delta}_i e^{i\mathbf{Q}\cdot\mathbf{r}_i} + h^*_\Delta(i,t)\hat{\Delta}^\dagger_i e^{-i\mathbf{Q}\cdot\mathbf{r}_i}], \tag{3.18}$$

where $\hat{\rho}_i = \frac{1}{2}c^\dagger_{i\sigma}c_{i\sigma}$ and $\hat{\Delta}_i = c_{i\downarrow}c_{i\uparrow}$. Going to momentum space,

$$H' = H_{MFT} - \frac{1}{N}\sum_{\mathbf{K}}\ h_\beta(\mathbf{K},t)\hat{O}^\dagger_\beta(\mathbf{K}), \tag{3.19}$$

where $\beta = 1,2,3$, and $\hat{\mathbf{O}}^\dagger(\mathbf{K}) \equiv \{\hat{\rho}_{-\mathbf{K}}, \hat{\Delta}_{-\mathbf{K}+\mathbf{Q}}, \hat{\Delta}^\dagger_{\mathbf{K}+\mathbf{Q}}\}$ is the vector of fermion bilinear operators representing modulations in density and in the superfluid order parameter at nonzero momenta. The operators $\hat{\rho}_{\mathbf{K}}$ and $\hat{\Delta}_{\mathbf{K}}$ are as defined in Sec. 2.3 of Chapter 2. The expectation value of a modulation field, within first order in perturbation theory, is given by

$$\langle\hat{O}_\alpha\rangle(\mathbf{K},t) = \int_{-\infty}^{+\infty} dt'\ \chi^0_{\alpha\beta}(\mathbf{K},t-t')h_\beta(\mathbf{K},t'). \tag{3.20}$$

In frequency domain, we obtain

$$\langle\hat{O}_\alpha(\mathbf{K},\omega)\rangle = \chi^0_{\alpha\beta}(\mathbf{K},\omega)h_\beta(\mathbf{K},\omega), \tag{3.21}$$

where

$$\chi^0_{\alpha\beta}(\mathbf{K},\omega) = \frac{1}{N}\sum_n \left(\frac{(\hat{O}^\dagger_\beta)_{0n}(\hat{O}_\alpha)_{n0}}{\omega + E_{n0} + i0^+} - \frac{(\hat{O}_\alpha)_{0n}(\hat{O}^\dagger_\beta)_{n0}}{\omega - E_{n0} + i0^+}\right). \tag{3.22}$$

The index n sums over all excited states of the mean-field Hamiltonian. We denote $(\hat{O})_{mn} \equiv \langle m|\hat{O}|n\rangle$, wherein $|n\rangle, |m\rangle$ are eigenstates of H_{MFT} (with $n=0$ corresponding to the ground state). In the denominator, $E_{n0} \equiv E_n – E_0$ where E_n is the energy of state $|n\rangle$. We evaluate these matrix elements by summing over all states in the Fock-space of Bogoliubov QPs. We give explicit expressions for the entries in the bare susceptibility matrix $\chi^0_{\alpha\beta}(\mathbf{K},\omega)$ in Appendix B.2.

In order to include interaction effects, we decouple the Hubbard interaction in fluctuation channels as in Sec. 2.3.2 of Chapter 2. This gives rise to 'internal' perturbing fields which add to $h_\beta(\mathbf{K},\omega)$. Taking into account these renormalized fields, the expectation value of modulations becomes:

$$\langle\hat{O}_\alpha\rangle = \chi^0_{\alpha\beta}(h_\beta + UD_{\beta\tau}\langle\hat{O}_\tau\rangle), \tag{3.23}$$

where $D \equiv \text{Diag}\{2,1,1\}$ is a diagonal matrix. We have suppressed $(\mathbf{K},\omega)$ labels for notational simplicity. Rearranging the above equation gives:

$$\langle \hat{O}_\alpha \rangle = [(1 - U\chi^0 D)^{-1}\chi^0]_{\alpha\beta}\ h_\beta \equiv \chi^{GRPA}_{\alpha\beta} h_\beta, \tag{3.24}$$

which defines the GRPA susceptibility. We identify the collective mode energy $\omega(\mathbf{K})$ from the poles of the GRPA susceptibility matrix. When the determinant $\text{Det}(1-U\chi^0 D)$ vanishes, the GRPA susceptibility diverges and a modulation field acquires a non-zero expectation value even in an infinitesimal external field.

Thus for any given interaction strength, filling and flow momentum, we can identify the dispersion of the collective mode from GRPA. In the following sections, we use the GRPA result for the collective mode spectrum and analyse the mechanisms of flow-induced instabilities.

3.4 Depairing Instability

The system undergoes a depairing instability when the self-consistently calculated superfluid order parameter, Δ_0, vanishes in the mean field theory. At the critical flow momentum, the energy cost of flow outweighs the energy-lowering from condensation and the system goes into an unpaired normal state.

This instability is close to, but not identical with, the quasiparticles becoming gapless due to the flow-induced Doppler shift. In two dimensions, we find that these two phenomena occur at the same flow momentum. In three dimensions however, superfluidity persists beyond the point where quasiparticles become gapless. The system cannot arbitrarily lower its energy as the negative energy states are fermionic in nature. Thus in three dimensions, there is a stable (albeit small) window of *gapless superfluidity*, as is known to occur in superfluid ^{3}He in the presence of flow[58]. Thus, this instability may be thought of as being closely related to the Landau criterion applied to Bogoliubov

QPs. This analogy should be treated with caution as the Bogoliubov QPs are fermionic excitations, unlike the bosonic excitations found in superfluids such as ^{4}He.

3.5 Landau Instability

The Landau instability is well understood in Bosonic systems[25, 27] and in Fermi gases with Galilean invariance[26]. This instability occurs when the collective mode energy hits zero and becomes negative, as shown in Fig. 3.2. In the strong coupling limit, with the collective mode dispersion given in Eq. 3.16, this happens when $\alpha_{\mathbf{K}}(\mathbf{Q}) \geq \gamma_{\mathbf{K}}(\mathbf{Q})$ and $\beta_{\mathbf{K}}(\mathbf{Q}) < -\sqrt{\alpha^2_{\mathbf{K}}(\mathbf{Q}) + \gamma^2_{\mathbf{K}}(\mathbf{Q})}$. This instability is driven by the Doppler shift term $\beta_{\mathbf{K}}(\mathbf{Q})$, which drives the collective mode energy below zero.

This instability may only lead to gradual loss of superfluidity as external couplings or non-linearities are necessary to transfer the energy of the superflow into these negative-energy modes in a way that conserves momentum. For this reason, this Landau instability may be difficult to detect in a cold-atoms experiment. Here we restrict ourselves to only finding the critical flow momentum for this instability.

We find that the Landau instability occurs either at small momenta corresponding to the sound mode going below zero, or at some finite incommensurate momentum. In the case of low filling, unless preempted by depairing, we see a Landau instability of the sound mode. For moderate values of U and filling, we see Landau instabilities at large incommensurate momenta (as in Fig. 3.2). As the filling is reduced, this incommensurate wavevector moves towards the Brillouin zone centre, so that in the low density limit, it is the long wavelength sound mode that becomes unstable.

3.6 Dynamical Instability

The underlying lattice potential allows for a new kind of superflow instability that does not occur in systems with Galilean invariance, namely 'dynamical instabilities'[27]. This

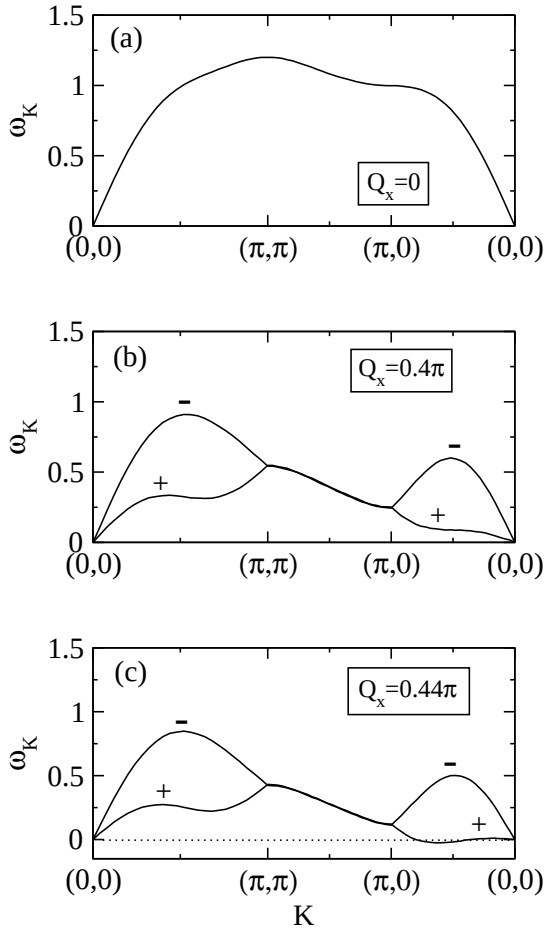

Figure 3.2: Landau instability - Collective mode spectrum (from GRPA) in 2D with $U/t = 7$ at a filling of $f = 0.4$ fermions per site. Collective mode dispersion is shown at (a) zero flow, (b) just below, and (c) just above, the critical flow momentum for the Landau instability. The $+(-)$ sign indicates the mode is at wavevector $+\mathbf{K}(-\mathbf{K})$ which has an x-component along (opposite to) the flow direction so that it is Doppler shifted down (up) in energy. The collective mode frequency becomes negative at an incommensurate wavevector.

corresponds to the frequency of the collective mode passing through zero, and subsequently becoming complex. In the strong coupling limit, this happens when $|\alpha_{\mathbf{K}}(\mathbf{Q})|$ becomes smaller than $|\gamma_{\mathbf{K}}(\mathbf{Q})|$. The appearance of complex collective mode frequencies leads to exponential growth of fluctuations around the uniformly flowing state. This instability is particularly simple to understand for weakly interacting bosons. In this case, the instability coincides with the point where the effective mass of the bosons changes sign as a function of the superflow momentum[27], leading to runaway growth of long-wavelength phase and density fluctuations, eventually destroying superfluidity.

For strongly interacting bosons the situation is more interesting. It has been shown[28] that with increasing interaction strength at a commensurate filling (integer number of bosons per site), the dynamical instability occurs at a smaller and smaller superflow momentum. The critical flow momentum eventually vanishes at the superfluid-Mott insulator transition, scaling as the inverse of the divergent correlation length associated with this Mott transition.

In our case of a lattice fermionic superfluid with strong interactions, we find a new kind of a dynamical instability, associated with the onset of density-wave order when the mode energies become complex at nonzero wavevectors. We find two kinds of such dynamical instabilities - commensurate and incommensurate.

3.6.1 Dynamical commensurate instability

The dynamical commensurate instability occurs for a range of densities close to half-filling, for all interaction strengths. The associated wavevector is the Brillouin zone corner - (π, π) in 2D (as shown in Fig. 3.3)and (π, π, π) in 3D. This corresponds to an instability towards the checkerboard CDW state, with a density modulation of opposite signs on the two sublattices of the square (or cubic) lattice.

Fig. 3.1 provides a physical picture of this instability as a manifestation of competition between superfluid and CDW orders. As described in Chapter 2, the superfluid and

CDW phases are degenerate at half-filling. Tuned away from half-filling, the CDW phase is a low-lying excitation above the superfluid ground state. At the critical flow momentum, the energy cost of superflow makes the superfluid and CDW phases comparable in energy. The system prefers to develop CDW correlations, and superfluidity is lost. This suggests the exciting possibility that superfluidity and CDW order may co-exist beyond this instability. To determine the fate of the system beyond this instability, we perform an extended mean-field theory allowing for both superfluidity and CDW order. The calculation is presented in Appendix B.3. While a 'supersolid' phase with coexisting orders is found within mean-field theory, this state appears to be unstable to long wavelength fluctuations. More work is needed to clarify the nature of this state.

From our strong coupling analysis in Chapter 2, the Doppler shift in the collective mode vanishes at Brillouin zone corner. At this wavevector, superflow renormalizes the dispersion via its effect on $\alpha_{\mathbf{K}}(\mathbf{Q}), \gamma_{\mathbf{K}}(\mathbf{Q})$. It is this renormalization that drives the dynamical commensurate instability.

3.6.2 Dynamical incommensurate instability

This instability is accompanied by the onset of incommensurate ordering patterns, as the collective mode frequency becomes complex at an incommensurate wavevector(Fig. 3.4). It occurs when there is a maximum in the bare susceptibility χ^0 at a wavevector connecting two minima in the quasiparticle dispersion. The interaction renormalizes such a maximum into a divergence, leading to an instability.

It can be understood in analogy with exciton condensation in indirect band-gap semiconductors[59]. The analogue of the conduction-band electrons and valence-band holes are Bogoliubov quasiparticles of opposite spins. In the case of exciton condensation, the band gap sets an energy gap to creating particle-hole pairs. Yet, the Coulomb interaction drives bound state formation and further, a Bose-condensation transition of these pairs. In our case, there is a gap to creating quasiparticle pairs. Yet, interactions

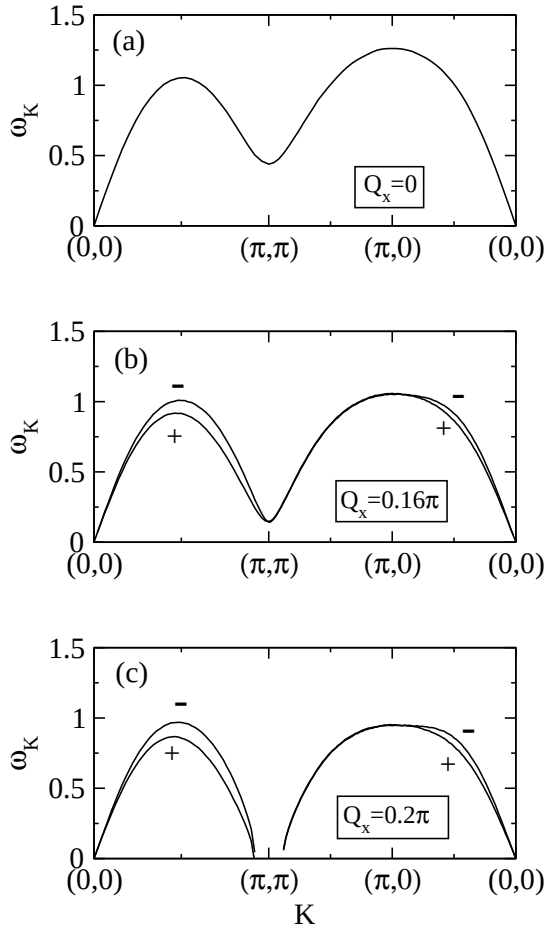

Figure 3.3: Dynamical Instability (Commensurate)- Collective mode spectrum (from GRPA) for $U/t = 5$, filling $f = 0.8$ fermions per site on a 2D square lattice. The $+(-)$ sign indicates the mode is at wavevector $+\mathbf{K}(-\mathbf{K})$ which has an x-component along (opposite to) the flow direction. As the flow momentum Q is increased, the collective mode frequency at $\mathbf{K} = (\pi, \pi)$ decreases until it hits zero and becomes complex. This gives rise to a dynamical instability associated with the "checkerboard" CDW order. The part of the dispersion, around (π, π), which corresponds to unstable modes is not shown.

of intermediate-strength cause the condensation of quasiparticle-pairs, as shown in Fig. 3.5.

This is the leading instability at intermediate densities and at intermediate values of the interaction strength. This instability does not happen in either the strong-coupling limit, where the Anderson pseudospin description is appropriate[51], nor in the weak-coupling BCS superfluid limit, where the instability at intermediate densities is due to depairing. This dynamical instability is a nontrivial intermediate-coupling phenomenon and is one of the most interesting findings of our study.

3.7 Stability phase diagrams

Taking the aforementioned instabilities into account, we map out superflow stability phase diagrams in 2D (Fig. 3.6) and 3D (Fig. 3.7). These plots show the first instability that is encountered with increasing flow, for different values of filling. We only consider densities less than half-filling, as the system is particle-hole symmetric. Values of U for the plots have been chosen so as to illustrate all possibilities.

As can be seen from the plots, the depairing instability is weak-coupling low-density phenomenon. As U is increased, the mean-field Δ_0 grows and a larger flow velocity is required for depairing to take place. At the same time, sound velocity decreases (see Fig. 2.5(b) in Chapter 2). As a result, for intermediate and large U values, the Landau instability of the sound mode precedes the depairing instability. The incommensurate dynamical instability occurs only at intermediate densities and interaction strengths, as large interactions seem to prefer commensurate order. The commensurate dynamical "checkerboard" CDW instability comes into play around quarter-filling for all values of the interaction strength and remains the dominant instability all the way to half-filling. At half-filling, the critical flow momentum vanishes reflecting the degeneracy between the SF and CDW states.

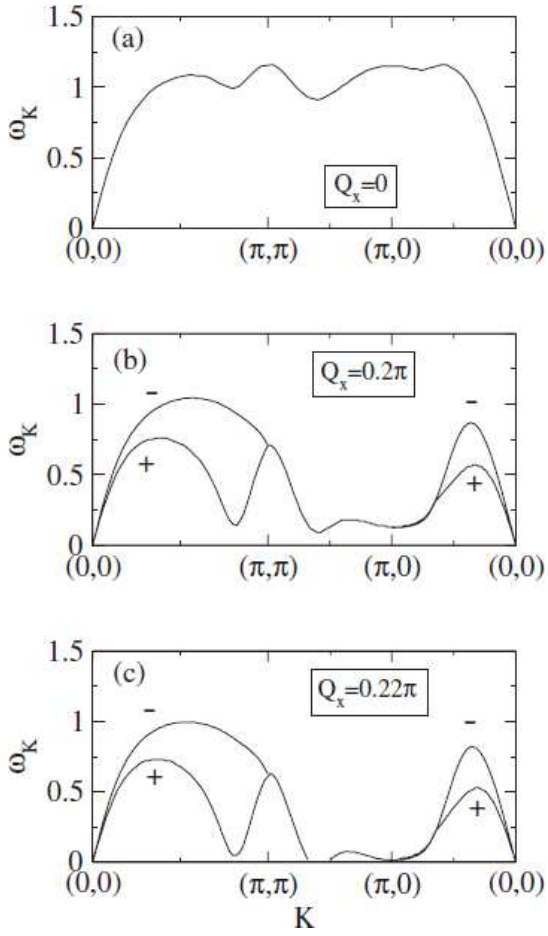

Figure 3.4: Dynamical Instability (Incommensurate) - Collective mode spectrum (from GRPA) for $U/t = 3$, filling $f = 0.6$ fermions per site on a 2D square lattice. The $+(-)$ sign indicates the mode is at wavevector $+\mathbf{K}(-\mathbf{K})$ which has an x-component along (opposite to) the flow direction. As the flow momentum Q_x is increased, the collective mode frequency becomes complex at an incommensurate wavevector.

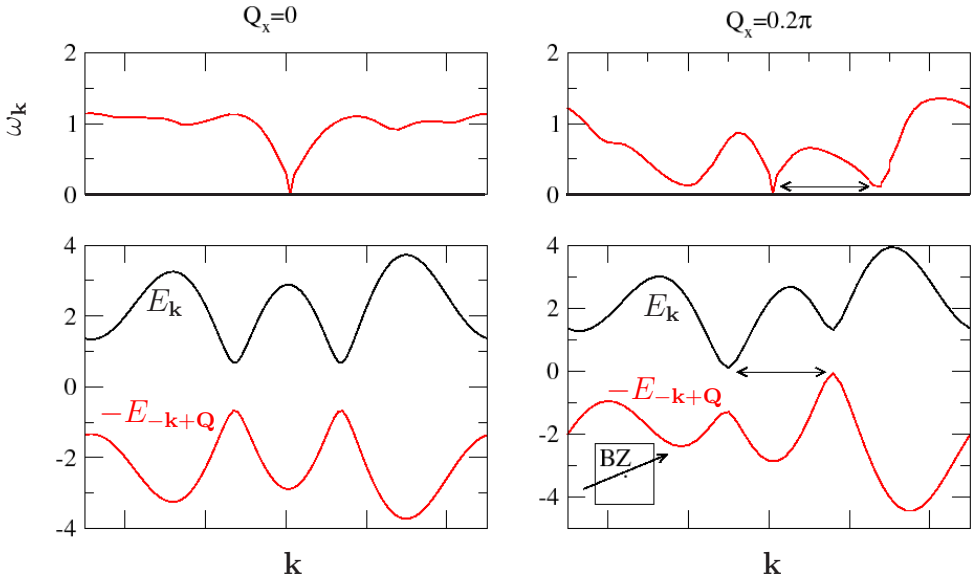

Figure 3.5: Dynamical incommensurate instability - analogy with exciton condensation: 2D, U/t=3. f=0.3. Left: At zero flow, the collective mode dispersion (top) and the Bogoliubov quasiparticle spectrum (bottom) along a cut in the Brillouin zone(shown in inset at bottom right). We have performed a particle hole transformation on one spin species, shown in red (see energy denominators in Eq. B.7). Right: On the verge of a dynamical incommensurate instability, the collective mode (top) and the quasiparticle spectrum(bottom). Quasiparticle spectrum resembles an indirect band-gap semiconductor. Dynamical instability is set to occur at the wavevector which connects the top of the 'valence band' with the bottom of the 'conduction band'.

In the low density limit, the system is similar to a continuum Fermi gas. In 3D, the density of states at the Fermi level vanishes. At low interaction strength, this leads to the pairing gap Δ being exponentially suppressed. The sound velocity, on the other hand, is proportional to the Fermi velocity, so that $v_s \sim f^{1/3}$ (f is the filling, i.e., average number of fermions per site). This leads to a rather sharp drop of the sound velocity at low densities but the gap drops to zero much faster. Therefore, in the 3D case, at weak interaction and low filling, a small imposed flow will drive Δ to zero before the flow velocity exceeds the sound velocity, leading to a depairing instability as can be be seen

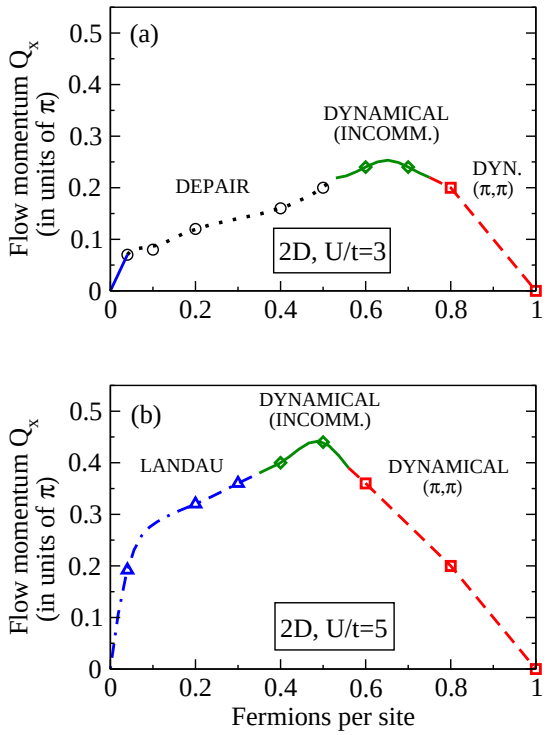

Figure 3.6: Stability phase diagram for a 2D square lattice case with (a) $U/t = 3$ and (b) $U/t = 5$. For every filling, the plot shows the first instability that is encountered as flow is increased. The solid blue line in the low density limit in (a) indicates the region where we expect to see a Landau instability, but finite size effects prevent us from accessing the area. At very large interaction strengths, the phase diagram is similar to $U/t = 5$, except that the incommensurate dynamical instabilities disappear.

in Fig. 3.7.

In contrast, in the low density continuum limit in 2D, the density of states goes to a constant, which means the pairing gap stays finite as $f \to 0$. With imposed flow, the first instability that one encounters is then the Landau instability, which will happen when the flow velocity exceeds the sound velocity which scales as $v_s \sim f^{1/2}$. We have not been able to numerically uncover the Landau instability in this regime due to severe finite size effects.

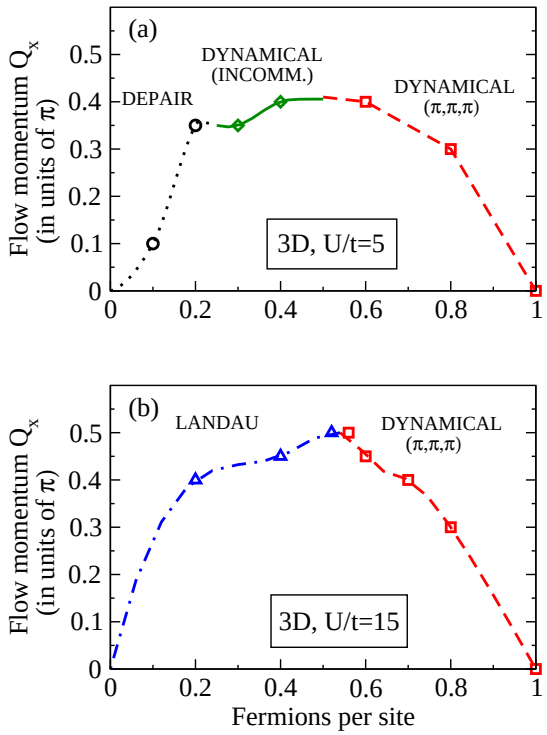

Figure 3.7: Stability phase diagram for a 3D cubic lattice with (a) $U/t = 5$ and (b)$U/t = 15$. For each filling, the instability first encountered as the flow is increased is shown.

3.8 Implications for experiments

There is great interest in the simulation of the Hubbard model in cold Fermi gases as a way to answering long-standing standing questions about the origin of superconductivity in the high-T_c cuprates. In the context of cold atoms, the repulsive Hubbard model could be difficult to simulate due to the presence of negative energy bound states which makes the Fermi gas prone to three-body losses. As a result, the attractive Hubbard model is currently the holy grail of cold atom experiments. However, this is not a straightforward task. It has not been well-established that the Hubbard model can be realized by loading fermions with an attractive contact interaction onto an optical lattice. As this is unexplored territory for experiments, there could be unforeseen problems. Secondly, experimentally ascertaining that the Hubbard model has indeed been realized

is a challenge. Superfluid order can be easily measured, but it is not easy to see if the fermions are confined to the lowest band alone. Our results can be extremely useful in this respect. Flow-induced checkerboard CDW order is easy to detect and provides conclusive evidence that the fermions form a one-band attractive Hubbard model.

The superflow instabilities of a Fermi gas with Galilean invariance have been investigated in Ref. [26]. For studying the attractive Hubbard model, an optical lattice can be achieved by using a pair of counterpropogating laser beams. The lattice potential should be deep enough so that higher bands are not accessed. Superfluid flow can then be simulated by frequency-detuning one pair of lattice beams, which creates a "running" optical lattice in the corresponding direction. Issues arising from the inhomogeneous harmonic trapping potential can be circumvented by studying the central region of the trap in which the potential is relatively flat. Once the atoms have been loaded onto a deep optical lattice, the trap can even be made very shallow so as to obtain a larger 'central' region. If the fermions are in a superfluid state, the atoms will not move with the running lattice. However, if a CDW phase emerges, atoms will be transported along with the lattice. Experimentally, the lattice should be moved sufficiently slowly so that the superfluid will adiabatically acquire a phase gradient.

Our findings may be experimentally verified in different ways:

(i) The effect of flow on collective modes (or the density-density response or the structure factor) can be measured using Bragg scattering measurements. This measurement has been successful for the case of a two-component Fermi gas with Galilean invariance[54]. In fact, this has been shown to be in excellent agreement with RPA results[55].

(ii) The density correlations that arise at a dynamical instability can be directly measured/imaged. This can be done by suddenly ramping up the lattice potential to freeze atoms on each site and to image the resulting distribution of atoms. Even before the onset of an instability, such a snapshot could reveal density fluctuations with some

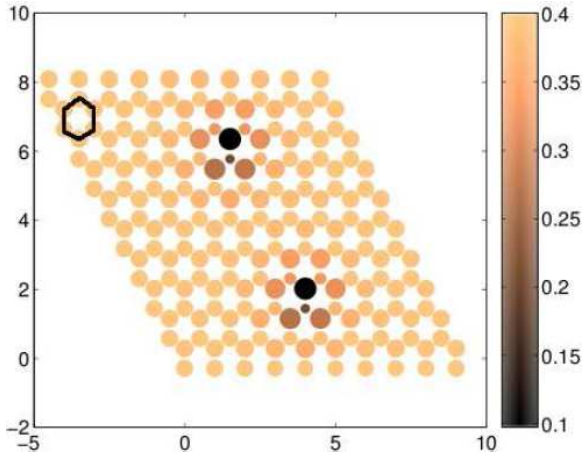

Figure 3.8: Simulation of CDW order in the vortex core in the *honeycomb* lattice Hubbard model: Plot of Δ_i, the superfluid order parameter, and density ρ_i as a function of position for U/t=5, t'/t=0.15 (next-nearest neighbour hopping) and filling of 1.1 fermions per site. Colour at each site represents the amplitude of Δ_i, and the size of the markers is proportional to ρ_i. As a guide to the eye, the honeycomb unit cell is shown at top left. Two vortices can be seen where the magnitude of Δ_i is minimum. There is uniform superfluid order away from the vortices and increased CDW correlations in the vortex core.

typical correlation length. On approaching the transition, this correlation length should diverge. Right at the onset of the dynamical commensurate instability, such a snapshot measurement will reveal clear checkerboard density correlations.

(iii) A third approach is to simply measure the critical velocity for dissipationless flow, as a function of various parameters, as has been done for Galilean invariant fermions in Ref. [26]. The resulting stability phase diagram can be compared with our result.

(iv) An analogy with vortex-core magnetism seen in the cuprates[1, 2] can be used to reveal competing orders in the Hubbard model. Superconductors proximate to competing phases such as the high-T_c cuprates, $TiSe_2$[7] and FeSe[60] can reveal competing orders in the vortex core. This can be understood by thinking of the vortex core as the region in which the critical superflow velocity has been locally exceeded. In the cold atoms

context, in the Hubbard model, vortices induced by 'stirring' the superfluid will show CDW correlations in the core region (see Fig. 3.8).

(v) In a solid state superconductor, when the magnetic field is increased beyond H_{c1}, vortices begin to appear. The density of vortices increases up until H_{c2} when the vortex lattice melts leading to the complete loss of superconductivity. Cold atom experiments can exhibit new features that are not seen in such solid state systems. A rotating gas with weak attractive interactions can be loaded onto an optical lattice. Slightly tightening the harmonic trapping potential can induce a density profile in this system with the central region having a higher density of fermions. Now, increasing the interaction strength using the Feshbach resonance can lead to rings which show different behaviour. The central region can develop CDW order and not carry any angular momentum. The surrounding region can be superfluid, and carry superfluid currents. The size of such a central CDW region will depend on the radius of the trapping potential and can possibly be much larger than the size of a vortex in a uniform system. Alternatively, such a CDW region can be thought of as arising from the melting of a vortex lattice in the centre of the trap, due to the large local density of vortices.

We hope experiments with ultracold gases can study many systems with competing orders. They can reveal novel phases such as supersolids with microscopic coexistence of phases, and precisely study the nature of phase transitions. With input from experiments, theoretical techniques such as the GRPA method can be refined and new insights obtained.

Part II

Competing phases in low dimensional magnets

Chapter 4

Dimer-Néel transition in bilayer antiferromagnets

4.1 Absence of long-range order and field-induced Néel order in BMNO

The recent synthesis of $Bi_3Mn_4O_{12}(NO_3)$(BMNO)[61] has aroused interest in honeycomb lattice antiferromagnets. We first present a brief overview of the properties of this material; this motivates and sets the stage for discussing paramagnetic ground states in this part of the thesis. BMNO is a $S = 3/2$ honeycomb bilayer system, with a Curie-Weiss temperature of -257K. In spite of the large value of S and the large Curie-Weiss temperature, this material remarkably shows no long range order down to 0.4K.

Fig. 4.1(a) shows a plot of the magnetic susceptibility versus temperature. At large temperatures, the susceptibility shows Curie-Weiss behaviour with a large negative Curie-Weiss temperature. This indicates the presence of antiferromagnetic exchange interactions at an energy scale of about 70 K. Yet, no sharp features corresponding to a phase transition are seen down to temperatures much lower than this interaction scale. As seen from Fig. 4.1(b), nor does the specific heat show any singularities down to the lowest

temperatures. (There is a small feature at 95 K, but it arises from a defect MnO_2 phase, which undergoes a Néel transition at that temperature). This suggests that the ground state in BMNO is a 'spin liquid' which does not break any symmetries.

The structure of BMNO is shown in Fig. 4.1(c,d). Each layer in this material is composed of MnO_6 octahedra arranged in a honeycomb lattice, with these honeycomb planes forming AA-stacked bilayers. Each octahedron has an Mn^{4+} ($3d^3$ $4s^0$) ion surrounded by Oxygen atoms in octahedral coordination. The octahedral crystal field splits the 3d levels in the Mn atom into three t_{2g} and two e_g levels. The three valence electrons occupy the t_{2g} levels, with strong Hund's coupling forcing the spins to be parallel. Effectively, BMNO forms a $S = 3/2$ honeycomb lattice bilayer with antiferromagnetic exchange interactions. The $S = 3/2$ nature of the spins has been confirmed by the Curie-Weiss fit to the high temperature susceptibility data.

The absence of long-range order has been confirmed by Electron Spin Resonance (ESR) measurements[62] which ESR shows a sharp absorption line that persists down to lowest temperatures. This indicates that spin is not pinned to any lattice direction - such pinning would lead to a diffuse peak when averaged over the different crystal orientations of the powder sample. We conclude that BMNO should be described by an effective model of Heisenberg $S = 3/2$ spins with antiferromagnetic interactions. In addition to nearest neighbour (J_1) exchange which favours antiferromagnetism, there should be other strong interactions that frustrate Néel order. The relative strengths of the interactions present in this material are not known. Next-nearest neighbour (J_2) interactions as shown in Fig. 4.1(d) have been suggested as the most natural source of frustration[61]. There have been two attempts to determine the microscopic interactions from first principcles. Density functional theory calculations[63] indicate that the most important interaction is bilayer coupling (J_c). Another approach using unrestricted Hartree-Fock calculations[64] suggests that in-plane J_4 interactions are the most important, however this calculation ignores interlayer couplings. More work is needed to clarify this issue.

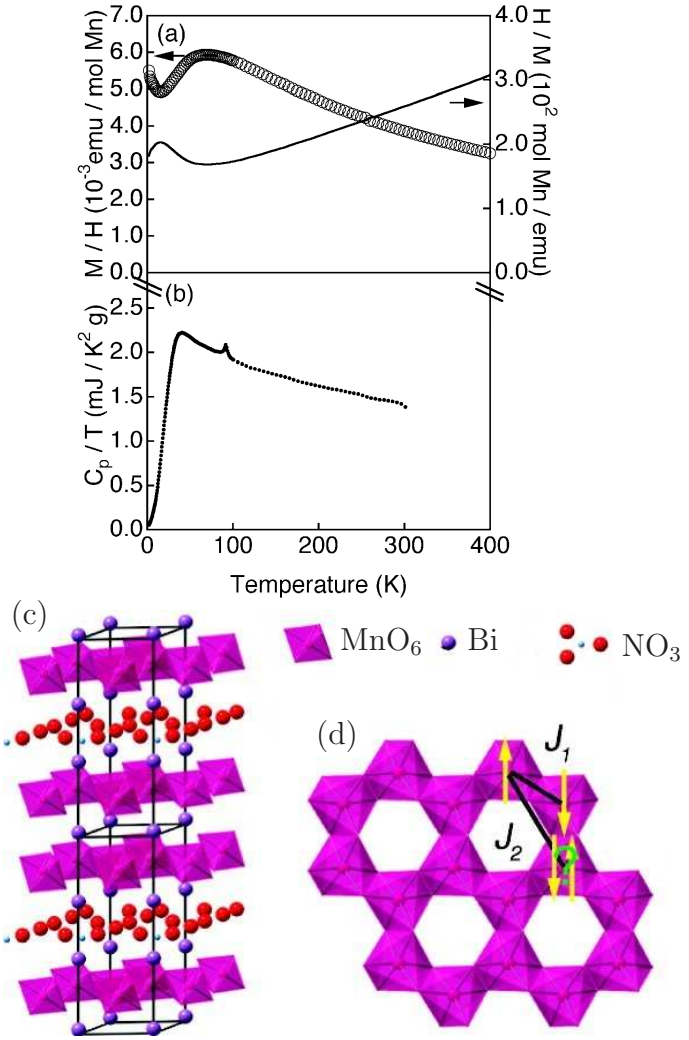

Figure 4.1: (a) Magnetic suscpetibility (and inverse susceptibilty) vs. temperature, (b) Specific heat vs. temperature. The sharp feature in specific heat at ∼90 K arises from a defect MnO_2 phase. (c) Structure of $Bi_3Mn_4O_{12}(NO_3)$, showing bilayer nature. (d) Each honeycomb layer built of MnO_6 octahedra. Reprinted with permission from JACS **131**, 8313 ©2009 American Chemical Society.

Remarkably, neutron powder diffraction measurements[65] reveal that BMNO develops Néel order in an applied magnetic field of about 6T. This raises several crucial questions such as the mechanism of field-induced Néel ordering, whether or not there is a preferred plane of ordering, the role of disorder etc.

Some theoretical calculations, including the work described in this thesis, have attempted to explain the physics seen in BMNO[66, 67, 37]. However, a satisfactory description of the material has not yet emerged. Any such description should identify the source of frustration, explain the nature of the ground state and the mechanism by which a magnetic field induces Néel order.

In this chapter, inspired by the physics of BMNO, we examine a bilayer $J_1 - J_c$ model with an interlayer dimer ground state which does not break any symmetries. We study the antiferromagnetic bilayer with spin-S on both square and honeycomb lattices. In Chapter 5, we examine the proposition that next-nearest neighbour exchange may frustrate Néel order. In Chapter 6, we shows that these two scenarios are consistent with field-induced Néel order. Finally, we point out the future directions for experimental and theoretical investigations of $Bi_3Mn_4O_{12}(NO_3)$ in Chapter 6.

4.2 Dimer states in bilayer antiferromagnets

Dimerized magnetic materials provide the simplest example of a magnetically disordered state, in which pairs of spins are entangled forming a singlet. The resulting state, described as a collection of singlets on selected bonds, is called a dimer phase or a 'Valence Bond Solid' (VBS). Some prominent materials which show such valence bond order are $TlCuCl_3$ which shows a field-induced Néel transition analogous to Bose-Einstein condensation[68, 69], and $SrCu_2(BO_3)_2$ which realizes the Shastry Sutherland model[70, 71, 72]. Many other materials are also known to support dimer phases[68, 73, 74]. Theoretically, various model Hamiltonians[75, 76, 77, 78] which give rise to dimer phases have

been studied. Novel dimer phases which break various symmetries of the underlying lattice have also been explored.

Dimerized magnets also provide a new means of studying the physics of Bose-Einstein condensation. In the dimer phase, the elementary excitations involve breaking a singlet bond to make a triplet. Typically, these triplet excitations acquire a dispersion and behave as bosons. In an applied magnetic field, these bosons undergo Bose-Einstein condensation leading to magnetically ordered phases[69, 79, 80]. In this chapter, we will study such a Bose condensation transition between a dimer phase and a Néel antiferromagnet.

We study a simple model which exhibits a dimer ground state - the bilayer Heisenberg antiferromagnet with a Hamiltonian given by

$$H = J_\perp \sum_i \mathbf{S}_{i,1} \cdot \mathbf{S}_{i,2} + J_1 \sum_{\langle ij \rangle} \sum_{\ell=1,2} \mathbf{S}_{i,\ell} \cdot \mathbf{S}_{j,\ell}. \tag{4.1}$$

Here, i labels sites in one layer, $\ell = 1, 2$ is the layer index, and $\langle ij \rangle$ represents nearest neighbor pairs of spins within each layer. For $J_\perp \gg J_1$, the first term in H dominates and the ground state is composed of isolated interlayer singlets with $\mathbf{S}_{i,1} + \mathbf{S}_{i,2} = 0$ for every i. If $J_\perp \ll J_1$, the system will order magnetically provided the second (intralayer) term in the Hamiltonian is not too frustrated by the lattice geometry. Here, we restrict our attention to cases where each layer is itself a bipartite lattice so that the ground state for $J_\perp \ll J_1$ has long-range Néel order. At some critical value of $(J_\perp/J_1)$, there is a phase transition between dimer and Néel phases. We will approach this phase transition from the dimer side and study how condensation of triplet excitations gives rise to Néel order.

As an example of a zero-temperature phase transition, the dimer-Néel transition has been carefully studied for the case of the $S = 1/2$ square lattice bilayer. Numerically exact Quantum Monte Carlo (QMC) simulations[76] have been used to obtain critical exponents. With a clear understanding of the quantum phase transition being established,

the effect of disorder on the critical properties has been extensively studied[81, 82, 83]. Also, various analytical approaches have been used to study this $S = 1/2$ square bilayer problem[84, 85, 86, 87], giving reasonable agreement with QMC results.

However, there has been relatively little work on understanding the higher spin generalizations of the Hamiltonian in Eq. 4.1, and generalizations to other lattice geometries. There is a need to systematically pursue this direction, especially in the context of materials such as the S=1 triangular lattice dimer compound $Ba_3Mn_2O_8$[88]. In this chapter, we study this Hamiltonian for $S = 1/2, 1, 3/2$ spins on square and honeycomb bilayers using the bond operator method generalized to arbitrary spin[89]. We use a variational method to include corrections beyond the standard bond operator mean field theory. This analysis was performed in conjunction with QMC simulations[90], performed by Sergei V. Isakov. Indeed, we study the square and honeycomb lattice geometries precisely because they are unfrustrated and therefore, amenable to QMC simulations. Our variational method gives reasonable agreement when compared to QMC benchmarks, giving us confidence in our method and allowing to identify the essential physics of the spin-S problem.

This chapter is organized as follows. We first present an outline of the bond operator representation generalized to arbitrary spin-S. We then discuss bond operator mean field theory results for the square and honeycomb lattice models. The mean field analysis yields scaling relations for the dimer-Néel transition which surprisingly also hold for the QMC results. The next section describes our variational approach to deal with corrections beyond mean field theory. We identify two regimes, $S = 1/2$ and $S > 1/2$, where different correction terms dominate. We present our analysis for each regime. Finally, we discuss implications for experiments and future directions.

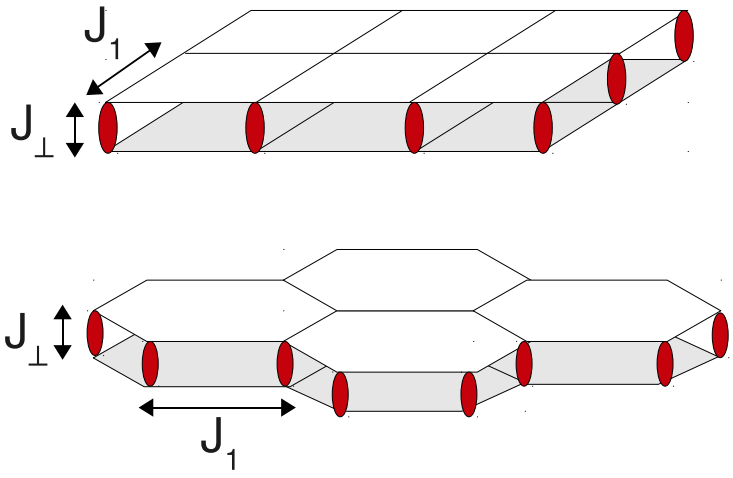

Figure 4.2: The interlayer dimer state on square and honeycomb bilayers with singlet correlations between layers. The in-plane exchange J_1 and the interplane exchange $J_\perp$ act as shown.

4.3 Bond operator representation

The dimer ground state and its magnetic ordering instabilities are naturally described by the bond operator formalism which was first proposed for $S = 1/2$ antiferromagnets[91]. In this scheme, the spin operators are represented in a new basis consisting of singlet and triplet states on the interlayer bonds $(i, 1)$-$(i, 2)$. In the limit where the intralayer coupling $J_1 = 0$, the state with lowest energy consists of localized singlets on these bonds, with a gap $J_\perp$ to the triplet excitations. A nonzero J_1 allows a pair of neighbouring bonds $(i, 1)$-$(i, 2)$ and $(j, 1)$-$(j, 2)$ to exchange their singlet/triplet character. Such a 'triplet hopping' process converts the localized triplet modes into dispersing 'triplons', with three-fold degenerate bands due to the underlying $SU(2)$ rotational symmetry of the Hamiltonian. As J_1 is increased (or alternatively, $J_\perp$ is decreased), the gap to creating triplon excitations decreases. At a critical value of $(J_\perp/J_1)_c$, the minimum of the triplon dispersion hits zero leading to Bose condensation of triplons which gives rise to Néel order. Generalizations of this approach to spin-1 magnets have been proposed earlier[92, 93]. Here, we adopt the recent generalization of this approach to higher spin[89] to study

bilayer Heisenberg antiferromagnets.

In a spin-S bilayer systems, in the limit $J_\perp \gg 1$, we have isolated interlayer bonds. The bond can be in one of the following states: a singlet, a 3-fold degenerate triplet, a 5-fold quintet, etc. We introduce one boson for each of these states:

$$\begin{aligned} |s_i\rangle &\equiv s_i^\dagger|0\rangle, \\ |t_{i,m\in\{-1,0,1\}}\rangle &\equiv t_{i,m}^\dagger|0\rangle, \\ |q_{i,m\in\{-2,\cdots,2\}}\rangle &\equiv q_{i,m}^\dagger|0\rangle, \\ &\vdots \end{aligned}$$

The index i here runs over all interlayer bonds, and m labels the S_z-component of the total spin on the interlayer bond. These boson operators form the basis for a bond operator representation. To restrict to the physical Hilbert space of spins, every interlayer bond should have exactly one boson,

$$s_i^\dagger s_i + \sum_{m=-1,0,1} t_{i,m}^\dagger t_{i,m} + \sum_{n=-2,\cdots,2} q_{i,n}^\dagger q_{i,n} + \cdots = 1. \tag{4.2}$$

In terms of bond operators, the exchange interaction on an interlayer bond is given by

$$J_\perp\ \mathbf{S}_{i,1}\cdot\mathbf{S}_{i,2} \;=\; \varepsilon_s s_i^\dagger s_i + \varepsilon_t \sum_{m=-1,0,1} t_{i,m}^\dagger t_{i,m} + \varepsilon_q \sum_{m=-2,\cdots,2} q_{i,m}^\dagger q_{i,m} + \cdots \tag{4.3}$$

where $\varepsilon_s = -J_\perp S(S+1)$, $\varepsilon_t = J_\perp\{1 - S(S+1)\}$, and $\varepsilon_q = J_\perp\{3 - S(S+1)\}$.

The bond operator theory re-expresses the spin operators and their interactions in terms of these bond bosons. In the limit $J_\perp \gg 1$, the singlets, triplets, quintets, etc. form a hierarchy with the energy spacing between each tier of order $J_\perp$. In this chapter, we restrict our analysis to the low energy subspace of singlets, triplets and quintets on each bond, and neglect higher spin states as the are much higher in energy.

We first perform conventional bond operator mean field theory retaining only singlet and triplet modes, ignoring triplet interactions and higher excited states and imposing the constraint in Eq. 4.2 on average. We then consider, in turn, the effect of triplet-triplet interactions for $S = 1/2$ and the effect of quintet states for $S > 1/2$.

4.4 Singlet-Triplet mean field theory

At mean field level, the interlayer dimer state is described by a uniform condensate of the singlet bosons, with $\langle s_i \rangle = \langle s_i^\dagger \rangle = \bar{s}$. Retaining only triplet excitations, the spin operators at each site are derived in Ref. [89]. The explicit expressions are

$$\begin{aligned} S^+_{i,\ell} &= (-1)^\ell \sqrt{\frac{2S(S+1)}{3}} \bar{s} \{ t_{i,-1} - t^\dagger_{i,1} \} + \frac{1}{\sqrt{2}} \{ t^\dagger_{i,1} t_{i,0} + t^\dagger_{i,0} t_{i,-1} \}, \\ S^z_{i,\ell} &= (-1)^\ell \sqrt{\frac{S(S+1)}{3}} \bar{s} \{ t_{i,0} + t^\dagger_{i,0} \} + \frac{1}{2} \{ t^\dagger_{i,1} t_{i,1} - t^\dagger_{i,-1} t_{i,-1} \}. \end{aligned}$$

Using these expressions, the Hamiltonian takes the form

$$\begin{aligned} H_{\rm mf} &= \varepsilon_s N_\perp \bar{s}^2 + \varepsilon_t \sum_{i,m} t^\dagger_{i,m} t_{i,m} - \mu \sum_i \left(\sum_m t^\dagger_{i,m} t_{i,m} + \bar{s}^2 - 1 \right) \\ &+ \frac{2S(S+1)}{3} \bar{s}^2 \sum_{\langle i,j \rangle} \left[\{ t_{i,0} + t^\dagger_{i,0} \} \{ t_{j,0} + t^\dagger_{j,0} \} + \left(\{ t_{i,-1} - t^\dagger_{i,1} \} \{ t^\dagger_{j,-1} - t_{j,1} \} + h.c. \right) \right], \end{aligned}$$

where μ is a Lagrange multiplier which enforces the constraint in Eq. 4.2 on average. $N_\perp$ is the number of interlayer bonds. We have dropped quartic terms in the triplet operators (which corresponds to ignoring triplet-triplet interactions).

In the rest of this chapter, we use the following two basis sets to represent triplet states: $\{ |t_{-1}\rangle_i, |t_0\rangle_i, |t_1\rangle_i \}$ or $\{ |t_x\rangle_i, |t_y\rangle_i, |t_z\rangle_i \}$. The former basis labels states by the z-projection of spin, while the latter labels states by the direction in which its spin projection is zero. We can go from one basis to another using $|t_0\rangle_i = |t_z\rangle_i$ and $|t_{\pm 1}\rangle_i = (\mp |t_x\rangle_i - i |t_y\rangle_i)/\sqrt{2}$. Below, we will use the index m to represent an element of the first basis and u to represent an element of the second.

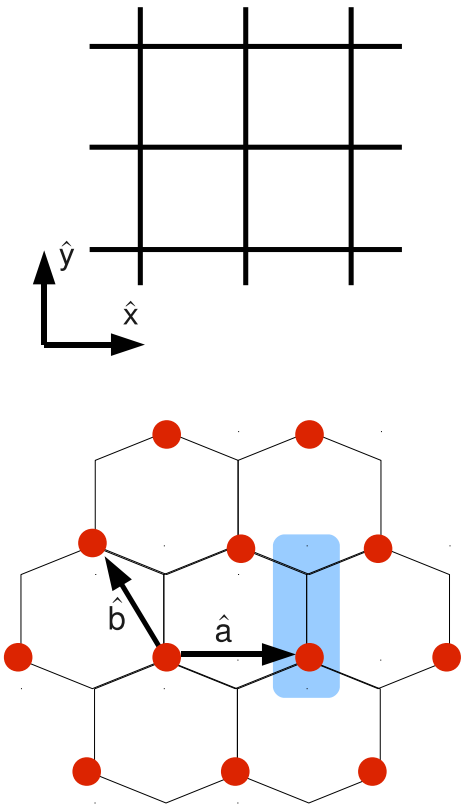

Figure 4.3: Top view of bilayers. (Top) Square lattice with primitive lattice vectors $\hat{x}$ and $\hat{y}$ shown. (Bottom) Honeycomb lattice. The shaded region is the unit cell composed of two sites. Sites marked with a red circle belong to the A sublattice. Unmarked sites belong to the B sublattice. The primitive lattice vectors $\hat{a}$ and $\hat{b}$ are shown.

4.4.1 Square lattice bilayer

The square lattice bilayer with its relevant couplings and primitive lattice vectors is shown in Fig. 4.3. At mean field level, the Hamiltonian of Eq. 4.1 may be written as

$$H_{\square}^{(0)} = -J_{\perp} N_{\perp} S(S+1)\bar{s}^2 - \mu \bar{s}^2 N_{\perp} + \mu N_{\perp} - \frac{3N_{\perp}A}{2} + \sum_{\mathbf{k},u\in\{x,y,z\}}{}' \psi^{\dagger}_{\mathbf{k},u} \begin{pmatrix} A+2\epsilon_{\mathbf{k}} & 2\epsilon_{\mathbf{k}} \\ 2\epsilon_{\mathbf{k}} & A+2\epsilon_{\mathbf{k}} \end{pmatrix} \psi_{\mathbf{k},u}, \tag{4.4}$$

where $\psi_{\mathbf{k},u} = [t_{\mathbf{k},u} \quad t^{\dagger}_{-\mathbf{k},u}]^T$. The primed summation indicates that if $\mathbf{k}$ is included in the sum, then $-\mathbf{k}$ is excluded. The coefficients in the Hamiltonian matrix are

$$A = J_\perp\{1 - S(S+1)\} - \mu, \tag{4.5}$$

$$\epsilon_{\mathbf{k}} = \frac{2S(S+1)}{3}\bar{s}^2(\cos(k_x) + \cos(k_y)) \tag{4.6}$$

Diagonalizing this Hamiltonian matrix by a bosonic Bogoliubov transformation (see Appendix C.1), we obtain eigenvalues $\lambda_{\mathbf{k}} = \sqrt{A(A + 4\epsilon_{\mathbf{k}})}$ for the energies of the independent 'triplon' modes. Each of these modes adds a zero point contribution to the ground state energy, yielding

$$E^{(0)}_{\square} = -J_\perp N_\perp S(S+1)\bar{s}^2 - \mu\bar{s}^2 N_\perp + \mu N_\perp - \frac{3N_\perp A}{2} + 3{\sum_{\mathbf{k}}}' \lambda_{\mathbf{k}}. \tag{4.7}$$

We minimize this ground state energy with respect to μ and $\bar{s}$, via $\partial E^{(0)}_{\square}/\partial\mu = 0$ and $\partial E^{(0)}_{\square}/\partial\bar{s}^2 = 0$. This yields the two equations

$$\bar{s}^2 = \frac{5}{2} - \frac{3}{N_\perp}{\sum_{\mathbf{k}}}' \frac{A + 2\epsilon_{\mathbf{k}}}{\lambda_{\mathbf{k}}}, \tag{4.8}$$

$$\mu = -J_\perp S(S+1) + \frac{6}{N_\perp}{\sum_{\mathbf{k}}}' \frac{A\epsilon_{\mathbf{k}}}{\bar{s}^2\lambda_{\mathbf{k}}}. \tag{4.9}$$

Using the values of $\bar{s}$ and μ thus obtained, we may calculate the gap to triplet excitations. The dimer-Néel transition occurs when the triplon gap vanishes at $J_\perp = J_{\perp c}$. Using Eqns. 4.8,4.9 above, we arrive at the following two results at the critical point.

(i) The value $\bar{s}$ at the dimer-Néel critical point is independent of spin and given by

$$\bar{s}_{\rm c}^2 = \frac{5}{2} - \frac{3}{2N_\perp}{\sum_{\mathbf{k}}}' \frac{4 + (\cos k_x + \cos k_y)}{\sqrt{4 + 2(\cos k_x + \cos k_y)}}. \tag{4.10}$$

A numerical evaluation shows $\bar{s}_c \approx 0.904$.

(ii) We find the location of the dimer-Néel critical point

$$J_{\perp c} = S(S+1)\left[\frac{40}{3} - \frac{32}{N_\perp}{\sum_{\mathbf{k}}}' \frac{1}{\sqrt{4 + 2(\cos k_x + \cos k_y)}}\right]. \tag{4.11}$$

A numerical evaluation yields $J_{\perp c} \approx 3.047S(S+1)$. For $S = 1/2$, this mean field result, $J_{\perp c}[S = 1/2] \approx 2.286$, is slightly smaller than the QMC value[84, 76]. For higher spin,

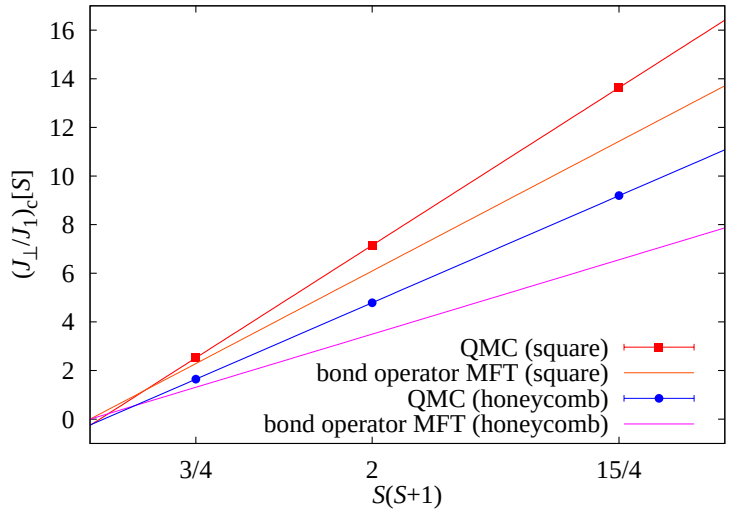

Figure 4.4: $J_{\perp c}/J_1[S]$ as a function of $S(S+1)$ for the bilayer square and honeycomb lattices. QMC data is from the simulations of S. V. Isakov[90]. MFT stands for Mean Field Theory. Lines are linear fits. Note that the curves cross approximately at $S(S+1) = 0$.

the mean field estimates, $J_{\perp c}[S=1] \approx 6.095$ and $J_{\perp c}[S=3/2] \approx 11.428$, are significantly smaller than the corresponding QMC results. This comparison is summarized in Table 4.1. Remarkably, as seen from Fig. 4.4, the scaling result $J_{\perp c} \sim S(S+1)$ derived from mean field theory seems to be reasonably accurate even for the exact QMC results. However, the associated prefactor differs from the QMC value. As S increases, mean field theory suffers from a systematic discrepancy. We note that this scaling of $J_{\perp c}$ with $S(S+1)$ has been pointed out in Ref.[94] on the basis of a series expansion calculation. Subsequent sections of this chapter deal with incorporating corrections beyond mean field theory with a view to bridging this systematic deviation.

4.4.2 Honeycomb lattice bilayer

The honeycomb lattice is composed of two interpenetrating triangular lattices, as shown in Fig. 4.3. Operators therefore come with an additional sublattice index which distin-

guishes A and B sublattices. The mean field Hamiltonian is given by

$$H^{(0)}_{\hexagon} = -N_\perp J_\perp S(S+1)\bar{s}^2 - N_\perp \mu \bar{s}^2 + N_\perp \mu - \frac{3N_\perp C}{2} + {\sum_{\mathbf{k},u}}' \psi^\dagger_{\mathbf{k},u} M_{\mathbf{k}} \psi_{\mathbf{k},u},$$

where $C = (J_\perp\{1 - S(S+1)\} - \mu)$. $N_\perp$ denotes the number of interlayer bonds in the honeycomb bilayer. The operator $\psi_{\mathbf{k},u}$ and the Hamiltonian matrix $M_{\mathbf{k}}$ are given by

$$\psi_{\mathbf{k},u} = \begin{pmatrix} t_{\mathbf{k},A,u} \\ t_{\mathbf{k},B,u} \\ t^\dagger_{-\mathbf{k},A,u} \\ t^\dagger_{-\mathbf{k},B,u} \end{pmatrix}, \quad M_{\mathbf{k}} = \begin{pmatrix} C & \beta_{\mathbf{k}} & 0 & \beta_{\mathbf{k}} \\ \beta^*_{\mathbf{k}} & C & \beta^*_{\mathbf{k}} & 0 \\ 0 & \beta_{\mathbf{k}} & C & \beta_{\mathbf{k}} \\ \beta^*_{\mathbf{k}} & 0 & \beta^*_{\mathbf{k}} & C \end{pmatrix}, \tag{4.12}$$

where $\beta_{\mathbf{k}} = 2\frac{S(S+1)}{3}\bar{s}^2\gamma_{\mathbf{k}}$, with $\gamma_{\mathbf{k}} = 1 + e^{-ik_b} + e^{-ik_a - ik_b}$, and we have defined $k_a \equiv \mathbf{k}\cdot\hat{a}$ and $k_b \equiv \mathbf{k}\cdot\hat{b}$. Diagonalizing this Hamiltonian (see Appendix C.3), we obtain two eigenvalues for every $\mathbf{k}$. The eigenvalues are given by

$$\lambda_{\mathbf{k},1/2} = \sqrt{C^2 \mp 2C|\beta_{\mathbf{k}}|}. \tag{4.13}$$

The mean field ground state energy is given by

$$E^{(0)}_{\hexagon} = -N_\perp J_\perp S(S+1)\bar{s}^2 - N_\perp \mu \bar{s}^2 + N_\perp \mu - \frac{3N_\perp C}{2} + 3{\sum_{\mathbf{k}}}'(\lambda_{\mathbf{k},1} + \lambda_{\mathbf{k},2}).$$

As before, we demand $\partial E^{(0)}_{\hexagon}/\partial\mu = 0$ and $\partial E^{(0)}_{\hexagon}/\partial\bar{s}^2 = 0$. This leads to the two mean field equations

$$\begin{aligned} \bar{s}^2 &= \frac{5}{2} - \frac{3}{N_\perp}{\sum_{\mathbf{k}}}' \left[\frac{C - |\beta_{\mathbf{k}}|}{\lambda_{\mathbf{k},1}} + \frac{C + |\beta_{\mathbf{k}}|}{\lambda_{\mathbf{k},2}}\right], \\ \mu &= -\frac{2CS(S+1)}{N_\perp}{\sum_{\mathbf{k}}}'|\gamma_{\mathbf{k}}|\left[\frac{1}{\lambda_{\mathbf{k},1}} - \frac{1}{\lambda_{\mathbf{k},2}}\right] - J_\perp S(S+1). \end{aligned} \tag{4.14}$$

Using the values of $\bar{s}$ and μ thus obtained, we may calculate the gap to triplet excitations. The dimer-Néel transition occurs when the triplon gap vanishes at $J_\perp = J_{\perp c}$. Using the above equations, we arrive at the following two results at the critical point.

(i) The value $\bar{s}$ at the dimer-Néel critical point is independent of spin and given by

$$\bar{s}_c^2 = \frac{5}{2} + \frac{3}{2N_\perp}{\sum_{\mathbf{k}}}'\left[\frac{|\gamma_{\mathbf{k}}| - 6}{\sqrt{9 - 3|\gamma_{\mathbf{k}}|}} - \frac{|\gamma_{\mathbf{k}}| + 6}{\sqrt{9 + 3|\gamma_{\mathbf{k}}|}}\right]. \tag{4.15}$$

A numerical evaluation shows $\bar{s}_c \approx 0.872$.

(ii) We find the location of the dimer-Néel critical point

$$\frac{J_{\perp c}}{S(S+1)} = 10 - \frac{36}{N_\perp} {\sum_{\mathbf{k}}}' \left[\frac{1}{\sqrt{9-3|\gamma_{\mathbf{k}}|}} + \frac{1}{\sqrt{9+3|\gamma_{\mathbf{k}}|}} \right]. \tag{4.16}$$

A numerical evaluation yields $J_{\perp c} \approx 1.748 S(S+1)$. For $S = 1/2$, the mean field result, $J_{\perp c}[S = 1/2] \approx 1.311$, is somewhat smaller than the QMC value. For higher spin, the mean field critical points, $J_{\perp c}[S = 1] \approx 3.496$ and $J_{\perp c}[S = 3/2] \approx 6.555$, are significantly smaller than the corresponding QMC results. This is summarized in Table 4.2. Remarkably, as shown in Fig. 4.4, the scaling result $J_{\perp c} \sim S(S+1)$ from mean field theory appears to be valid even for the exact QMC results on the honeycomb lattice. However, the associated prefactor is different, which leads to a systematic discrepancy increasing with S.

4.5 Beyond mean field theory: Variational analysis

Corrections to the mean field Hamiltonian arise from triplet-triplet interactions, coupling to higher spin objects such as quintets, heptets, etc. As a function of S, we find two regimes where different correction terms dominate. For S=1/2, the only correction stems from triplet-triplet interactions, while for higher spin, the dominant correction comes from coupling to quintet states. These two cases are separately discussed in the following two sections.

As a function of S, we identify the leading correction and take it into account using a variational approach. Our variational ansatz assumes that the correction terms preserve the structure of the mean field Hamiltonian - their only effect is to renormalize the parameters $\bar{s}$ and μ. With the leading correction, the Hamiltonian for the square/honeycomb lattice takes the form

$$H_{\square/\hexagon} = H^{(0)}_{\square/\hexagon}(\bar{s}, \mu) + \Delta H_{\square/\hexagon}(S). \tag{4.17}$$

We treat $\Delta H(S)$ as a perturbation acting upon $H^{(0)}$. The unperturbed Hamiltonian depends on the parameters $\bar{s}$ and μ. As a function of these two parameters, we evaluate the ground state energy E_{var} to leading order in perturbation theory.

We choose μ to enforce single boson occupancy per site on overage. The perturbations ΔH, for both regimes, preserve total boson number. Thus, it suffices to evaluate total boson number using $H^{(0)}$. This gives us the constraint

$$\bar{s}^2 + \sum_{i,m} \langle t^\dagger_{i,m} t_{i,m} \rangle = N_\perp, \tag{4.18}$$

where the expectation value is evaluated with respect to $H^{(0)}$. (For the honeycomb lattice case, there is an additional sum over the sublattice degree of freedom in the above equation). This leads precisely to the mean field number constraint in Eq. 4.8 or Eq. 4.14, which can now be used to determine μ. The parameter $\bar{s}$ is chosen to minimize the ground state energy, evaluated to leading order in perturbation theory. For $S = 1/2$, we find that the leading correction is obtained within first order perturbation theory in ΔH. For $S > 1/2$, the dominant perturbing terms require us to go to second order in perturbation theory. In the next two sections, we discuss these correction terms in detail.

4.6 $S = 1/2$ case

4.6.1 Triplet interactions on square lattice

For $S = 1/2$, there are no higher spin bosons beyond the singlet-triplet sector. The only correction to mean field theory stems from triplet-triplet interactions. The triplet interaction terms are given by

$$\Delta H^{S=1/2}_{\square} = -\frac{1}{2} \sum_{\langle ij \rangle} \sum_{\substack{u,v,w,v',w' \\ \in \{x,y,z\}}} \epsilon_{uvw} t^\dagger_{i,v} t_{i,w} \epsilon_{uv'w'} t^\dagger_{j,v'} t_{j,w'}. \tag{4.19}$$

We note that there are no cubic terms in triplet operators. As described in Ref. [95], this makes our bilayer problem qualitatively different from other dimerized states such as the spin-1/2 staggered dimer on the square lattice. Treating this quartic interaction as a perturbation acting on $H_{\square}^{(0)}$, we evaluate the first order correction to ground state energy. To this end, we decouple $\Delta H_{\square}^{trip.int.}$ using bilinears that possess finite expectation values at the level of mean field theory:

$$\begin{aligned}\langle t_{i,v}^{\dagger} t_{i+\delta,w} \rangle &\equiv \delta_{v,w}\rho, \\ \langle t_{i,v}^{\dagger} t_{i+\delta,w}^{\dagger} \rangle &\equiv \delta_{v,w}\Delta. \end{aligned} \tag{4.20}$$

Here, i and $i+\delta$ are nearest neighbours on the square lattice. Explicit expressions for ρ and Δ are given in Appendix C.2. We note that ρ and Δ are functions of the variational parameters $\bar{s}$ and μ. The first order energy correction due to triplet interactions is given by

$$\Delta E_{\square}^{S=1/2} = \langle \Delta H_{\square}^{S=1/2} \rangle = 6N_{\perp}\left[\rho^2 - \Delta^2\right]. \tag{4.21}$$

Thus, for $S = 1/2$, the energy of the ground state to leading order in perturbation theory is given by

$$E_{\square,var}^{(S=1/2)}(\bar{s},\mu) = E_{\square}^{(0)} + \Delta E_{\square}^{S=1/2}, \tag{4.22}$$

where $E_{\square}^{(0)}$ is as defined in Eq. 4.7. The parameter $\bar{s}$ is chosen to minimize this energy.

4.6.2 Triplet interactions on the honeycomb lattice

The interaction between triplets on the honeycomb lattice is given by

$$\Delta H_{\hexagon}^{S=1/2} = -\frac{1}{2}\sum_{i,\delta} \sum_{\substack{u,v,w,v',w' \\ \in \{x,y,z\}}} \epsilon_{uvw} t_{i,A,v}^{\dagger} t_{i,A,w} \epsilon_{uv'w'} t_{i+\delta,B,v'}^{\dagger} t_{i+\delta,B,w'}.$$

The operators δ are such that the sites (i, A) and $(i+\delta, B)$ are nearest neighbours. This interaction term contributes to the ground state energy at first order in perturbation theory. To evaluate this correction, we quadratically decompose the interaction using the following two bilinears:

$$\begin{aligned}\langle t^\dagger_{i,A,v} t_{i+\delta,B,w}\rangle &\equiv \delta_{v,w}\rho,\\ \langle t^\dagger_{i,A,v} t^\dagger_{i+\delta,B,w}\rangle &\equiv \delta_{v,w}\Delta,\end{aligned} \tag{4.23}$$

with the expectation values to be evaluated in the unperturbed Hamiltonian $H^{(0)}_{\hexagon}$. The first order correction to ground state energy is given by

$$\Delta E^{S=1/2} = \frac{9}{2} N_\perp [\rho^2 - \Delta^2]. \tag{4.24}$$

The parameter $\bar{s}$ is chosen to minimize the energy

$$E^{S=1/2}_{\hexagon,var}(\bar{s},\mu) = E^{(0)}_{\hexagon} + \Delta E^{S=1/2}_{\hexagon}. \tag{4.25}$$

4.7 $S > 1/2$ case

For $S > 1/2$, the bond operator representation involves higher spin objects. We expect the leading corrections to mean field theory to arise from coupling to quintet states, as we argue below. Upon including quintet terms, the spin operators at a site i are given by (see Eq. 21 of Ref. [89])

$$\begin{aligned} S^+_{i,\ell=1,2} &= (-1)^\ell \sqrt{\frac{2S(S+1)}{3}}\bar{s}\{t_{i,-1} - t^\dagger_{i,1}\} \\ &+ (-1)^\ell \sqrt{\frac{(2S-1)(2S+3)}{5}}\Big[\{t^\dagger_{i,-1} q_{i,-2} - q^\dagger_{i,2} t_{i,1}\} \\ &+ \frac{1}{\sqrt{2}}\{t^\dagger_{i,0} q_{i,-1} - q^\dagger_{i,1} t_{i,0}\} + \frac{1}{\sqrt{6}}\{t^\dagger_{i,1} q_{i,0} - q^\dagger_{i,0} t_{i,-1}\}\Big] \\ &+ \frac{1}{\sqrt{2}}\{t^\dagger_{i,1} t_{i,0} + t^\dagger_{i,0} t_{i,-1}\} + \sqrt{\frac{3}{2}}\{q^\dagger_{i,1} q_{i,0} + q^\dagger_{i,0} q_{i,-1}\} + q^\dagger_{i,2} q_{i,1} + q^\dagger_{i,-1} q_{i,-2}, \end{aligned}$$

$$
\begin{aligned}
S^z_{i,\ell=1,2} \;=\; & (-1)^\ell \sqrt{\frac{S(S+1)}{3}} \{t_{i,0} + t^\dagger_{i,0}\} \\
& + (-1)^\ell \sqrt{\frac{(2S-1)(2S+3)}{5}} \left[\frac{1}{\sqrt{3}} \{t^\dagger_{i,0} q_{i,0} + q^\dagger_{i,0} t_{i,0}\} \right. \\
& + \left. \frac{1}{2} \{t^\dagger_{i,1} q_{i,1} + q^\dagger_{i,1} t_{i,1} + t^\dagger_{i,-1} q_{i,-1} + q^\dagger_{i,-1} t_{i,-1}\} \right] \\
& + \frac{1}{2} \{t^\dagger_{i,1} t_{i,1} - t^\dagger_{i,-1} t_{i,-1} + q^\dagger_{i,1} q_{i,1} - q^\dagger_{i,-1} q_{i,-1}\} + q^\dagger_{i,2} q_{i,2} - q^\dagger_{i,-2} q_{i,-2}.
\end{aligned}
$$

We rewrite the Hamiltonian of Eq. 4.1 using these spin expressions. The correction terms beyond mean field theory that involve quintet states may be grouped as

$$\Delta H^{S>1/2} \sim \hat{D}_{tttt} + \bar{s}\hat{E}_{ttq}(S^2) + \hat{F}_{ttqq}(S^2) + \hat{G}_{qqqq}(S^0). \tag{4.26}$$

The subscripts indicate the composition of the terms in terms of bond operators. The scaling of each term with S is indicated in parentheses . For example, $\hat{E}_{ttq}(S^2)$ is composed of terms which involve two triplet operators and one quintet operator. The coefficients of these terms scale as S^2.

For large values of S, the dominant correction will arise from terms which scale as S^2. As quintets are high-energy excitations, we only retain the lowest order terms which are linear in quintet operators given by $\bar{s}\hat{E}_{ttq}$. (For the case of $S = 1$, we have checked that this term dominates over triplet-triplet interactions encoded by $\hat{D}_{tttt}$). In the neighbourhood of the dimer-Néel transition, we assert that $\hat{R}_{ttq}(S^2)$ will remain the dominant correction term for any $S > 1/2$ even if higher spin states such as heptets, nonets, etc., are included. As the dimer-Néel transition occurs via condensation of triplet excitations, it is reasonable that the dominant corrections come from quintets which are immediately higher in energy than triplets. Heptets, nonets, etc. occur at much higher energies and are unlikely to affect the triplet condensation point. To argue this, we first note that the Hamiltonian of Eq.4.1 can change the spin of a bond by ± 1 at most (this can be seen from the rotation properties of a single spin operator acting on a bond eigenstate). For example, on any one particular bond, the Hamiltonian connects a triplet state to

singlet, triplet and quintet states. The matrix element connecting the triplet to a nonet state (or a state of even higher spin) is zero. Similarly, on a given bond, the heptet state has non-zero matrix elements only with quintet, heptet and nonet states. The resulting terms in the Hamiltonian involving heptets, nonets, etc. will *not* contribute at second order in perturbation theory, but will only appear at higher order. As an illustration, upon including heptets, the Hamiltonian can have a term of the form $h^\dagger_{i,m} q_{i,n} t^\dagger_{j,m'} t_{j,n'}$. Clearly, this term does not contribute to ground state energy at first or second order. In addition, at whichever order it contributes, the energy denominators will involve large heptet excitation energies which will further suppress the energy contribution.

In summary, in the vicinity of the dimer-Néel transition for any value of $S > 1/2$, the leading correction to bond operator mean field theory comes from $\bar{s}\hat{R}_{ttq}(S^2)$. We write

$$\Delta H^{(S>1/2)} \approx \Delta H^{(\mathrm{q})} \equiv \bar{s}\hat{R}_{ttq}(S^2). \tag{4.27}$$

For the square/honeycomb lattice, we obtain

$$\Delta H^{S>1/2}_{\square/\hexagon} \approx \bar{s}\hat{E}_{ttq}(S^2). \tag{4.28}$$

In order to treat this term perturbatively, we take the quintet states to be local excitations. The energy cost of creating a quintet is given by Eq. 4.3. We measure this energy cost from the Lagrange multiplier μ, to get

$$\varepsilon_q - \mu = J_\perp\{3 - S(S+1) - \mu\} \tag{4.29}$$

as the energy cost of a quintet excitation.

4.7.1 Coupling to quintets on the square lattice

The terms in $\bar{s}\hat{E}_{ttq}(S^2)$ may be organized as

$$\bar{s}\hat{E}_{ttq}(S^2) = \bar{s}\sum_i \sum_{n=-2,\cdots,2} \left[q^\dagger_{i,n} \sum_\delta \hat{T}^{[n]}_{i,i+\delta} + h.c. \right]. \tag{4.30}$$

The operator $\hat{T}^{[n]}_{i,i+\delta}$ is composed of triplet bilinears. The index δ sums over the four nearest neighbour vectors on the square lattice. The explicit form of these operators is given in Appendix C.2. The operator $\hat{E}_{ttq}(S^2)$ does not contribute to ground state energy at first order, as it is linear in quintet operators. The energy correction, at second order, is given by

$$\Delta E^{S>1/2}_{\square} = \bar{s}^2 \sum_{\sigma \neq 0} \sum_{\substack{i,n,\delta \\ i',n',\delta'}} \frac{\langle 0|q_{i',n'}(\hat{T}^{[n]}_{i',i'+\delta'})^\dagger|\sigma\rangle\langle\sigma|q^\dagger_{i,n}\hat{T}^{[n]}_{i,i+\delta}|0\rangle}{E_0 - E_\sigma}. \tag{4.31}$$

The index σ sums over all excited states of $H^{(0)}_{\square}$, the variational Hamiltonian. The only intermediate states that contribute are those with a single quintet. In our variational formalism, we take the quintets to be local excitations. This constrains us to $(i = i')$, $(n = n')$. This leaves us with

$$\Delta E^{S>1/2}_{\square} = \bar{s}^2 \sum_{\nu \neq 0} \sum_{i,n} \frac{\langle 0|\sum_{\delta'}(\hat{T}^{[n]}_{i,i+\delta'})^\dagger|\nu\rangle\langle\nu|\sum_{\delta}\hat{T}^{[n]}_{i,i+\delta}|0\rangle}{E_0 - E_\nu}. \tag{4.32}$$

The intermediate states $|\nu\rangle$ which contribute involve a single quintet excitation. Within the triplet sector, at zero temperature, the intermediate states can have either (a) no triplon quasiparticles, or (b) two triplon quasiparticles. The contribution from states with no triplon quasiparticles vanishes due to global spin-rotational symmetry of the Hamiltonian. The energy correction from two triplon intermediate states is evaluated (see Appendix C.2), to obtain the energy correction, $\Delta E^{[S>1/2]}_{\square}$.

Being second order in $\hat{E}_{ttq}(S^2)$, the energy correction from quintet coupling naïvely scales as S^4. However, the energy denominator involves the energy of quintet states which is proportional to $J_\perp$. Close to the dimer-Néel transition, at mean field level, $J_\perp$ approximately scales as S^2 (see Eq. 4.11). We expect small perturbative corrections to preserve this scaling of $J_{\perp c}$ with S^2. Thus, near the dimer-Néel transition, $\Delta E^{S>1/2}_{\square}$ scales as $S^4/S^2 \sim S^2$. The ground state energy to leading order in perturbation theory is given

S	QMC	MFT	MFT + triplet interactions	MFT + quintet coupling
0.5	2.5220(1)	2.286	2.52	-
1	7.150(2)	6.095	6.40	7.13
1.5	13.634(3)	11.428	11.74	13.75

Table 4.1: Value of $J_{\perp c}$ on the square lattice from different methods for different values of S. The column QMC gives results of QMC simulations performed by S. V. Isakov[90]. The QMC data for S=1/2 has been reported earlier in Ref. [76]. MFT stands for Mean Field Theory. The column 'MFT+Triplet interactions' gives variational results appropriate for S=1/2. The column 'MFT+quintet coupling' gives variational results appropriate for S > 1/2.

by

$$E^{S>1/2}_{\square,var}(\bar{s},\mu) = E^{[2]}_{\square} + \Delta E^{S>1/2}_{\square}. \tag{4.33}$$

This energy is a function of $\bar{s}$ and μ. As discussed earlier, μ is tuned to enforce single boson occupancy per site, while $\bar{s}$ is chosen to minimize E_{var}.

Having determined $\bar{s}$ and μ variationally, we can find the gap to triplon excitations as a function of $J_\perp$. The Dimer-Néel transition is indicated by the vanishing of the triplon gap in the variationally obtained state. As summarized in Table 4.1, the renormalized critical points obtained in this manner are within 1% of the QMC results. This precise quantitative agreement is perhaps fortuitous, and will certainly change depending on the nature of the approximations made. The important problem we have resolved is to show that the large discrepancy between QMC and simple bond operator mean field theory for $S > 1/2$ can be accounted for by virtual quintet excitations. Also, this high degree of quantitative agreement indicates that the neglected correction terms compete with each other to yield a small net correction. Precisely how this happens is not clear, and could be explored in future studies.

4.7.2 Coupling to quintets on the honeycomb lattice

On the honeycomb lattice, the terms in $\bar{s}\hat{E}_{ttq}(S^2)$ may be written as

$$\bar{s}\hat{E}_{ttq} = \bar{s}\sum_i \sum_{n=-2,\cdots,2} \left[q^\dagger_{i,A,n} \sum_\delta \hat{A}^{[n]}_{i,i+\delta} + q^\dagger_{i,B,n} \sum_\delta \hat{B}^{[n]}_{i,i-\delta} + h.c. \right]. \tag{4.34}$$

The operators $\hat{A}_{i,i+\delta}$ and $\hat{B}_{i,i-\delta}$ are triplet bilinears centred on nearest neighbour bonds. We give their explicit forms in momentum space in Appendix C.4. The terms in $\hat{E}_{ttq}(S^2)$ contribute to ground state energy only at second order in perturbation theory. The energy correction may be written as

$$\begin{aligned} \Delta E^{S>1/2}_{\hexagon} &= \bar{s}^2 \sum_{\sigma\neq 0} \sum_{i,n} \frac{\langle 0| \left[q_{i,A,n} \sum_{\delta'} \hat{A}^{[n]}_{i,i+\delta'} \right] |\sigma\rangle\langle\sigma| \left[q^\dagger_{i,A,n} \sum_\delta \hat{A}^{[n]}_{i,i+\delta} \right] |0\rangle}{\{E_0 - E_\sigma\}} \\ &+ \ (A \to B), \end{aligned} \tag{4.35}$$

where the index σ sums over all excited states of H_{var}. As the terms in $\hat{E}_{ttq}(S^2)$ involve one quintet operator, only intermediate states with a single occupied quintet state will contribute.

$$\begin{aligned} \Delta E^{S>1/2}_{\hexagon} = \bar{s}^2 \sum_{\nu\neq 0} \sum_{i,n} & \frac{\langle 0| \sum_{\delta'} (\hat{A}^{[n]}_{i,i+\delta'})^\dagger |\nu\rangle\langle\nu| \sum_\delta \hat{A}^{[n]}_{i,i+\delta} |0\rangle}{\{E_0 - E_\nu\}} \\ + \bar{s}^2 \sum_{\nu\neq 0} \sum_{i,n} & \frac{\langle 0| \sum_{\delta'} (\hat{B}^{[n]}_{i,i-\delta'})^\dagger |\nu\rangle\langle\nu| \sum_\delta \hat{B}^{[n]}_{i,i-\delta} |0\rangle}{\{E_0 - E_\nu\}}. \end{aligned} \tag{4.36}$$

We evaluate these overlaps in momentum space, as described in Appendix C.4. The intermediate state $|\nu\rangle$ could have either (i) no triplon quasiparticles, or (ii) two triplon quasiparticles. However, the contribution from states with no triplons vanishes due to global spin rotational symmetry. The explicit expression for $\Delta E^{S>1/2}_{\hexagon}$ is given in Appendix C.4.

Thus, the energy of the ground state to leading order in quintet coupling, is given by

$$E^{S>1/2}_{\hexagon,var} = E^{(0)}_{\hexagon} + \Delta E^{S>1/2}_{\hexagon}. \tag{4.37}$$

We choose $\bar{s}$ to minimize this energy. The vanishing of the triplet gap in the variationally determined state signals the dimer-Néel transition. Our results for $J_{\perp c}$ on the honeycomb

S	QMC	MFT	MFT + triplet interactions	MFT + quintet coupling
0.5	1.645(1)	1.311	1.59	-
1	4.785(1)	3.496	3.80	4.91
1.5	9.194(3)	6.555	6.86	9.79

Table 4.2: Value of $J_{\perp c}$ on the honeycomb lattice from different methods for different values of S. The column QMC gives results of QMC simulations performed by S. V. Isakov[90]. MFT stands for Mean Field Theory.

lattice are shown in Table 4.2. While the renormalized critical points for $S = 1, 3/2$ are within 6% of the QMC value, the agreement in this case is not as good as on the square lattice.

4.8 Discussion

We have studied the Néel to dimer transition in Heisenberg antiferromagnets on bilayer square and honeycomb lattices for different spin values using the bond operator method. Going beyond bond operator mean field theory, we find two regimes in which different correction terms dominate. We take these corrections into account corrections using a variational approach. Our results agree well with QMC simulations, giving us confidence in our method. The critical bilayer exchange $J_{\perp c}$ scales as $S(S+1)$ within, both, bond operator mean field theory and QMC simulations. However, there is a systematic deviation between bond operator mean field theory and QMC, with the deviation itself scaling as $\sim S^2$. Our variational extension of bond operator theory successfully captures this systematic deviation and gives a more precise estimate of $J_{\perp c}$.

$Bi_3Mn_4O_{12}(NO_3)$ provides an example of a bilayer honeycomb antiferromagnet[61] with $S = 3/2$, where strong interlayer exchange couplings $\sim 2J_1$ have been inferred from electronic structure calculations[63]. Despite this strong bilayer coupling, our study in-

dicates that this material would be deep in the Néel ordered phase if there are no other frustrating interactions. We thus rule out large bilayer coupling as the cause of the observed lack of magnetic order in $Bi_3Mn_4O_{12}(NO_3)$. One recent example of a dimer system with $S = 1$ is the triangular dimer material[88, 96] $Ba_3Mn_2O_8$. Our approach could be applied to understand the triplon spectrum and the effect of quintet corrections in this material. In particular, our work shows that extracting exchange couplings from fitting experimental data to bond operator mean field theory will not yield precise estimates when $S > 1/2$. Our work provides a starting point to think about the physics of high spin Heisenberg antiferromagnets in a variety of model systems and materials.

Chapter 5

Lattice nematic phases on the honeycomb lattice

We begin this chapter with a brief introduction to the intermediate-U physics of the honeycomb lattice Hubbard model. This provides another motivation for the study of frustration on the honeycomb lattice.

5.1 Intermediate-U phase of the honeycomb lattice Hubbard model

A parallel motivation for the study of frustrated magnets is their utility as model systems for the physics of strongly correlated electrons. In the limit of strong coupling, Hubbard-like electronic models can be mapped onto appropriate pseudospin models which may be frustrated. This confluence of magnetism and strongly correlated electron systems is seen in the recently discovered spin-gapped phase in the honeycomb lattice Hubbard model. At weak coupling, electrons on the honeycomb lattice have low density of states at the Fermi level; consequently, the system remains a 'semi-metal' with point-like Fermi surfaces. At strong coupling, the Hubbard repulsion leads to Mott insulating phase

with antiferromagnetic order driven by superexchange. In the intermediate regime($3.5 \lesssim U/t \lesssim 4.3$), determinantal Monte-carlo simulations by Meng et al.[97] have revealed a spin-gapped insulating phase which interpolates between the semimetal and the Mott insulator. The nature of this intervening state has been debated with great interest.

At half-filling, in the limit of large U/t, the low energy description is restricted to the subspace of singly occuppied sites. An effective description can be given in terms of a spin-1/2 Heisenberg model of localized spins[98, 99]. Superexchange between nearest neighbour sites leads to antiferromagnetic J_1 coupling. Exchange interactions with further neighbours are suppressed by factors of t/U. On the honeycomb lattice which is bipartite, the resulting ground state is a Néel antiferromagnet. As U/t is decreased, however, longer range exchange interactions become important. Approaching the intermediate U/t regime from the strong-coupling side, the leading correction is expected to next-nearest neighbour exchange. This gives rise to the effective Hamiltonian,

$$H = J_1 \sum_{\langle ij \rangle} \mathbf{S}_i \cdot \mathbf{S}_j + J_2 \sum_{\langle\langle ij \rangle\rangle} \mathbf{S}_i \cdot \mathbf{S}_j. \tag{5.1}$$

where J_1 and J_2 denote nearest neighbour exchange and next-nearest neighbour exchange respectively. In terms of the Hubbard model parameters, the exchange constants[100] are given by

$$J_1 = \frac{4t^2}{U} - \frac{16t^4}{U^3}; \quad J_2 = \frac{4t^4}{U^3}. \tag{5.2}$$

This J_2 coupling is a frustrating term which disfavours Néel order. The degree of frustration is tuned by the frustration paramter J_2/J_1. The spin-gapped phase of the Hubbard model is expected to be realized for intermediate values of frustration, around $J_2/J_1 \gtrsim 0.07$.

Various techniques have been used to study this $J_1 - J_2$ model with a view to understanding the spin-gapped phase of the honeycomb lattice Hubbard model. The $J_1 - J_2$ model is not amenable to Quantum Monte Carlo simulations due to frustration-induced sign problems. This makes it a difficult proposition to determine its ground state for

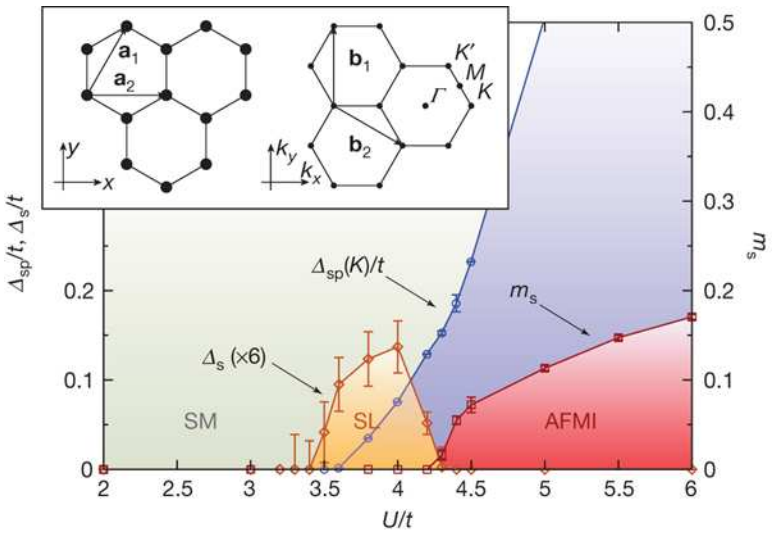

Figure 5.1: Monte Carlo study of the honeycomb lattice Hubbard model from Ref.[97]: plots of Δ_s (spin gap), Δ_{sp} (single particle gap) and m_s (magnetization) as functions of U/t. Density is fixed at half-filling. A spin-gapped phase occurs between the semimetal and antiferromagnetic Mott insulating phases. Reprinted by permission from Macmillan Publishers Ltd: Nature **464**, 847 ©2011.

intermediate values of the frustration parameter J_2/J_1. Two proposals have been put forward: a Z_2 spin liquid and a plaquette RVB state.

Initially, it was suggested that the spin-gapped phase is a spin-liquid that does not break any symmetries[97]. Projective symmetry group analysis has been used to identify the number of distinct spin liquid states[101, 102]. A 'zero-flux state'[101] was proposed on the basis of a Schwinger-boson analysis and a 'sublattice pairing state'[102] was suggested using a slave-fermion approach. These two descriptions were shown to be equivalent[102]. A variational Monte Carlo calculation[100] analysed various possible spin-liquid candidates and concluded that the sublattice pairing state has the lowest energy for $0.08 < J_2/J_1 < 0.3$.

Another candidate for the spin-gapped state of the Hubbard model is the 'plaquette RVB' state shown in Fig. 1.3(c). Exact diagonalization studies[36, 34] on the $J_1 - J_2$ model have found this to be the ground state for $0.16 \lesssim J_2/J_1 \lesssim 0.4$. This state breaks

translational symmetry, and is therefore not a spin liquid. As the Z_2 spin liquid and the plaquette RVB state have been suggested by two different approaches, the nature of the spin-gapped state has not yet been established. Precise calculations using an unbiased approach may help resolve the true ground state.

In this chapter, we study the honeycomb lattice $J_1 - J_2$ model in various limits. We are inspired by experiments on $Bi_3Mn_4O_{12}(NO_3)$and by the intermediate-U physics of the honeycomb lattice Hubbard model. For the case of spin-1/2, we postulate a 'Nematic Valence Bond Solid' (NVBS) ground state for large values of the frustration parameter. Various studies of the $J_1 - J_2$ model which were inspired by the honeycomb lattice Hubbard model, have confirmed the occurrence of an NVBS ground state for $J_2/J_1 \gtrsim 0.4$[36, 34, 100]. In Chapter 6, we predict within a quantum melting picture that the spin-gapped phase will develop Néel order in an applied magnetic field.

We hope that calculations of the J_1-J_2 model will soon clarify the spin-gapped state of the Hubbard model. Conversely, the honeycomb lattice Hubbard model provides a simple system that can be analyzed numerically using determinental Monte Carlo techniques. Further numerical studies of the Hubbard model may help us understand the physics of frustrated magnetism on the honeycomb lattice.

5.2 Lattice nematics and the honeycomb lattice $J_1 - J_2$ model: Introduction

Bipartite lattices, such as cubic and honeycomb lattices, do not possess geometric frustration. They are composed of two sublattices; each site interacts with its nearest neighbours which belong to the other sublattice. With antiferromagnetic interactions, such systems invariably exhibit Néel ground states with opposite spins residing on the two sublattices. However, large additional interactions can break the bipartite nature of the Hamiltonian by favouring anti-alignment of spins within the same sublattice. If Néel order is thus

disfavoured, various states compete to be the true ground state and in the process, novel phases can emerge.

This effect is particularly well-studied in the case of the square lattice. Both next-nearest neighbour(J_2) exchange and third-nearest neighbour(J_3) interactions can frustrate Néel order. Both these interactions lead to novel states which break Ising-like symmetries. In the classical limit of the square lattice J_1-J_2 model[33, 103], the ground state remains Néel ordered for $J_2 < J_1/2$. However, when J_2 exceeds $J_1/2$ there is a large set of degenerate ground states in which the two sublattices are individually perfectly Néel ordered with an arbitrary relative angle between their ordering vectors. Within this classical manifold, quantum $\mathcal{O}(1/S)$ fluctuations and weak thermal fluctuations select collinear ground states with ordering wavevectors $\mathbf{Q} = (\pi, 0)$ or $(0, \pi)$. Being two-dimensional, this model exhibits exponentially decaying spin correlations at any non-zero temperature consistent with the Mermin-Wagner theorem, but the broken lattice rotational symmetry survives at low temperatures. Upon further heating, this 'lattice nematic' undergoes a phase transition into the high temperature paramagnetic phase via an Ising transition[33, 104]. For the extreme quantum case of $S = 1/2$, despite a large number of numerical studies[105, 106, 107], the ground state phase diagram has not been fully understood.

Nematic order arising from fluctuations has also been explored in the J_1-J_3 model on the square lattice[108]. In this case, there is a Néel-spiral Lifshitz transition for $J_3 > J_1/4$. The classical ground state manifold is doubly degenerate, composed of two spirals with wavevectors (Q, Q) and $(Q, -Q)$ which are related by a $\pi/2$ rotation of the lattice. At any non-zero temperature, the magnetic spiral ordering is lost. However, the Ising nematic order remains up until a nematic-paramagnetic transition temperature.

In analogy with the square lattice models, we study non-geometric frustration on the honeycomb lattice in its simplest realization - the Heisenberg model with frustration

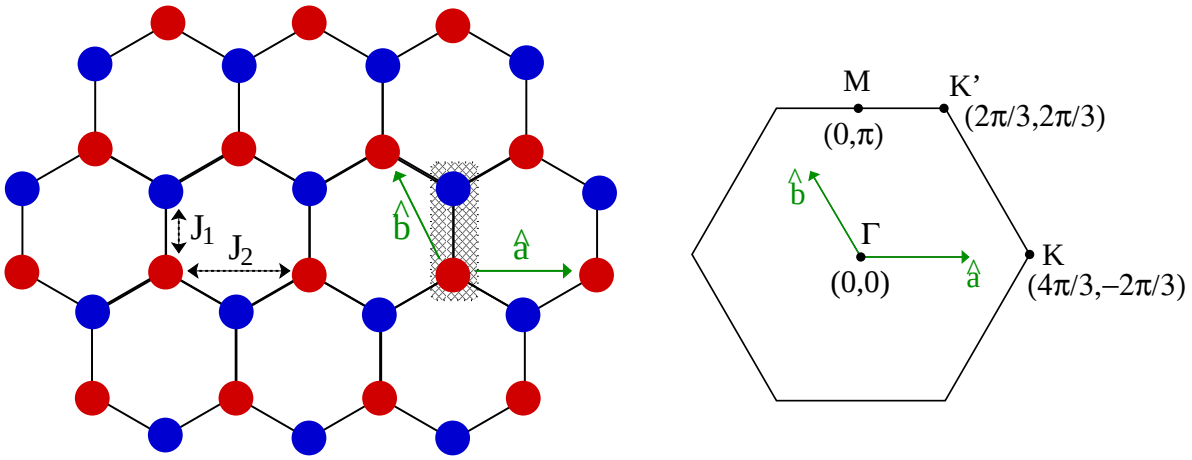

Figure 5.2: Left: The honeycomb lattice made of two interpenetrating sublattices - sublattice A(B) is shown in red(blue). Nearest neighbour(J_1) and next-nearest neighbour bonds (J_2) are as indicated. The shaded area marks the unit cell, $\hat{a}$ and $\hat{b}$ are the primitive lattice vectors. Right: The first Brillouin zone, with the high-symmetry points labelled.

arising from the next-nearest neighbour (J_2) couplings.

$$H = J_1 \sum_{\langle ij \rangle} \mathbf{S}_i \cdot \mathbf{S}_j + J_2 \sum_{\langle\langle ij \rangle\rangle} \mathbf{S}_i \cdot \mathbf{S}_j. \tag{5.3}$$

where $\langle . \rangle$ and $\langle\langle . \rangle\rangle$ denote nearest and next-nearest neighbour bonds respectively. Interest in this model stems from (a) possible relevance to the frustrated magnet $Bi_3Mn_4O_{12}(NO_3)$[61], and (b) relevance to the intermediate coupling physics of the honeycomb lattice Hubbard model[97, 100, 36, 34]. This model Hamiltonian is not exactly solvable, nor does it lend itself to quantum Monte Carlo methods on account of frustration-induced sign problems. In order to make progress, we study this model in various limits. We begin with a classical analysis of the $J_1 - J_2$ model. We then discuss the effects of weak quantum fluctuations within a large-S expansion. We next consider thermal fluctuations. Finally, in the extreme quantum case of $S = 1/2$, we use bond operator theory to study some aspects of the system. In all three cases, frustration leads to a three-fold degeneracy associated with the breaking of lattice rotational symmetry .

5.3 Classical ground state

As a first step, we take the spins to be 'classical' - as three-dimensional vectors with all components commuting with each other. This corresponds to the (S$\rightarrow \infty$) limit of the quantum spin-S model. We take the ground state to be a coplanar spiral state, in keeping with the general argument that quantum and thermal fluctuations favour a coplanar state over a non-coplanar state[109, 110]. By this reasoning, a collinear state would be even more favoured, but in our case, the collinear Néel state is frustrated by J_2 interactions. We have verified using classical Monte Carlo simulations[66] that the ground state is indeed coplanar. We note that non-coplanar ground states exist at the special point $J_2/J_1 = 0.5$, at which additional degrees of freedom allow for non-coplanar ordering[111].

As the Hamiltonian is invariant under global spin rotations, coplanar ordering could occur in any plane in spin space. The plane of ordering would be spontaneously chosen by the system, we pick the plane to be the XZ plane (in spin space) below. The spins on each sublattice may be characterized as

$$\mathbf{S}_A(\mathbf{r}) = S\left[\cos(\mathbf{Q}\cdot\mathbf{r})\hat{z} + \sin(\mathbf{Q}\cdot\mathbf{r})\hat{x}\right]; \quad \mathbf{S}_B(\mathbf{r}) = -S\left[\cos(\mathbf{Q}\cdot\mathbf{r}+\phi)\hat{z} + \sin(\mathbf{Q}\cdot\mathbf{r}+\phi)\hat{x}\right] \tag{5.4}$$

where $\mathbf{Q}$ is the spiral wavevector, $\mathbf{r}$ denotes sites of the triangular sublattice, and $\phi+\pi$ is the angle between A and B spins within a unit cell. This notation is chosen so that the Néel state corresponds to $\mathbf{Q} = (0,0)$ and $\phi = 0$, with spins aligned along $\pm\hat{z}$. Evaluating the Hamiltonian of Eq. 5.3 in the classical spiral state, we find the energy per spin to be

$$\frac{E_{\rm cl}}{N} = -\frac{J_1 S^2}{2}[\cos\phi + \cos(\phi - Q_b) + \cos(\phi - Q_a - Q_b)] + J_2 S^2\left[\cos Q_a + \cos Q_b + \cos(Q_a + Q_b)\right], \tag{5.5}$$

where $\hat{a} = \hat{x}$, and $\hat{b} = -\hat{x}/2 + \hat{y}\sqrt{3}/2$, are unit vectors depicted in Fig. 5.2. Minimizing this classical energy, we find that the minimum energy solution for $J_2/J_1 < 1/6$ corresponds to $\mathbf{Q}^* = (0,0), \phi = 0$. For this range of frustration, the classical ground state is the Néel state. For $J_2/J_1 > 1/6$, the minimum energy solutions correspond to $\mathbf{Q}^*$

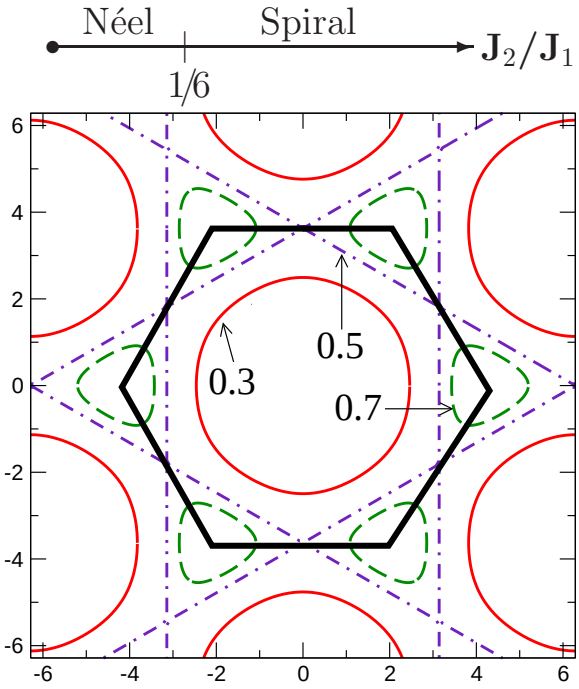

Figure 5.3: Top: Phase diagram of the classical $J_1 - J_2$ model. Bottom: The manifold of classically degenerate spiral wavevectors is drawn for $J_2/J_1 = 0.3$ (red, thin solid), $J_2/J_1 = 0.5$ (purple, dash-dotted), and $J_2/J_1 = 0.7$ (green, dashed). Black (thick solid) hexagon is the first Brillouin zone.

satisfying the relation

$$\cos Q_a^* + \cos Q_b^* + \cos(Q_a^* + Q_b^*) = \frac{1}{2}\left[\left(\frac{J_1}{2J_2}\right)^2 - 3\right], \tag{5.6}$$

while ϕ^* is determined completely by

$$\sin\phi^* = 2\frac{J_2}{J_1}(\sin Q_b^* + \sin(Q_a^* + Q_b^*)), \tag{5.7}$$

$$\cos\phi^* = 2\frac{J_2}{J_1}(1 + \cos Q_b^* + \cos(Q_a^* + Q_b^*)). \tag{5.8}$$

The spiral wavevector is not uniquely fixed by the above relations. As shown in Fig. 5.3, the set of classically degenerate solutions to Eq. 5.6 (which we label $\mathbf{Q}^*$) forms a closed contour around $\mathbf{Q} = (0,0)$ for $1/6 < J_2/J_1 < 1/2$. For $J_2/J_1 > 1/2$, it forms a closed contour around $(Q_a, Q_b) \equiv \pm(2\pi/3, 2\pi/3)$. In the limit $J_2/J_1 \to \infty$, the two triangular sublattices of the honeycomb lattice approximately decouple. In this limit,

we find $\mathbf{Q}^* \to \pm(2\pi/3, 2\pi/3)$ which is the ordering wavevector of the 120° state on the triangular lattice. We next discuss how quantum or thermal fluctuations select specific spin spirals from this manifold of classical ground state spirals.

5.4 Weak quantum fluctuations: spin wave analysis

Using Holstein-Primakoff (HP) spin wave theory, we calculate the leading quantum correction to the energy of the spiral state defined in Eq. 5.4. We first define new spin operators $\tilde{\mathbf{S}}$ via

$$\begin{pmatrix} \tilde{S}^x_\nu(\mathbf{r}) \\ \tilde{S}^y_\nu(\mathbf{r}) \\ \tilde{S}^z_\nu(\mathbf{r}) \end{pmatrix} = \begin{pmatrix} \cos\theta_\nu(\mathbf{r}) & 0 & -\sin\theta_\nu(\mathbf{r}) \\ 0 & 1 & 0 \\ \sin\theta_\nu(\mathbf{r}) & 0 & \cos\theta_\nu(\mathbf{r}) \end{pmatrix} \begin{pmatrix} S^x_\nu(\mathbf{r}) \\ S^y_\nu(\mathbf{r}) \\ S^z_\nu(\mathbf{r}) \end{pmatrix} \tag{5.9}$$

where $\nu = A, B$ labels the sublattice, $\theta_A(\mathbf{r}) = \mathbf{Q}\cdot\mathbf{r}$, and $\theta_B(\mathbf{r}) = \mathbf{Q}\cdot\mathbf{r} + \phi$. This transforms our spiral state into a ferromagnet with spins pointing along the Z axis. We work in this new basis with the parameters of the original spiral absorbed into the Hamiltonian. Reexpressing the Hamiltonian in terms of the new $\tilde{S}$ operators and rewriting these spin operators in terms of HP bosons, we arrive at the following Hamiltonian which includes the leading spin wave correction to the classical spiral energy,

$$H_{\text{qu}} = E_{\text{cl}} + 2S \sum_{\mathbf{k}>0} \left[\vec{b}_{\mathbf{k}}{}^\dagger M_{\mathbf{k}} \vec{b}_{\mathbf{k}} - 2A_{\mathbf{k}} \right]. \tag{5.10}$$

Here $\vec{b}^\dagger = \left(b^\dagger_A(\mathbf{k})\ b^\dagger_B(\mathbf{k})\ b_A(-\mathbf{k})\ b_B(-\mathbf{k}) \right)$, $\sum_{\mathbf{k}>0}$ indicates that the sum runs over half the first Brillouin zone (so that $\mathbf{k}$ and $-\mathbf{k}$ are not both included). The Hamiltonian matrix $M_{\mathbf{k}}$ takes the form

$$M_{\mathbf{k}} = \begin{pmatrix} A_{\mathbf{k}} & B_{\mathbf{k}} & C_{\mathbf{k}} & D_{\mathbf{k}} \\ B^*_{\mathbf{k}} & A_{\mathbf{k}} & D^*_{\mathbf{k}} & C_{\mathbf{k}} \\ C_{\mathbf{k}} & D_{\mathbf{k}} & A_{\mathbf{k}} & B_{\mathbf{k}} \\ D^*_{\mathbf{k}} & C_{\mathbf{k}} & B^*_{\mathbf{k}} & A_{\mathbf{k}} \end{pmatrix}, \tag{5.11}$$

with $A_{\mathbf{k}}$-$D_{\mathbf{k}}$ given by

$$\begin{aligned}
A_{\mathbf{k}} &= \frac{J_1}{2}[\cos\phi+\cos(\phi-Q_b)+\cos(\phi-Q_a-Q_b)] - J_2[\cos Q_a + \cos Q_b + \cos(Q_a+Q_b)] \\
&+ \frac{J_2}{2}[(\cos Q_a + 1)\cos k_a + (\cos Q_b + 1)\cos k_b + (\cos(Q_a+Q_b)+1)\cos(k_a+k_b)], \\
B_{\mathbf{k}} &= \frac{J_1}{4}[(\cos\phi - 1) + (\cos(\phi - Q_b) - 1)e^{-ik_b} + (\cos(\phi - Q_a - Q_b) - 1)e^{-i(k_a+k_b)}], \\
C_{\mathbf{k}} &= \frac{J_2}{2}[(\cos(Q_a) - 1)\cos(k_a) + (\cos(Q_b) - 1)\cos(k_b) + (\cos(Q_a+Q_b) - 1)\cos(k_a+k_b)], \\
D_{\mathbf{k}} &= \frac{J_1}{4}[(\cos\phi + 1) + (\cos(\phi - Q_b) + 1)e^{-ik_b} + (\cos(\phi - Q_a - Q_b) + 1)e^{-i(k_a+k_b)}].
\end{aligned}$$

Diagonalizing this problem via a generalized Bogoliubov transformation, we obtain the spin wave corrected spiral energy as

$$E_{\rm qu} = E_{\rm cl} + 2S\sum_{\mathbf{k}>0}[\lambda_-(\mathbf{k}) + \lambda_+(\mathbf{k}) - 2A_{\mathbf{k}}] \tag{5.12}$$

The eigenvalues $\lambda_\pm(\mathbf{k})$ are given by

$$\lambda_\pm(\mathbf{k}) = \sqrt{\alpha_{\mathbf{k}} \pm \beta_{\mathbf{k}}}, \tag{5.13}$$

where

$$\alpha_{\mathbf{k}} = A_{\mathbf{k}}^2 - C_{\mathbf{k}}^2 + |B_{\mathbf{k}}|^2 - |D_{\mathbf{k}}|^2, \tag{5.14}$$

$$\beta_{\mathbf{k}} = \sqrt{4|A_{\mathbf{k}}B_{\mathbf{k}} - C_{\mathbf{k}}D_{\mathbf{k}}|^2 + (D_{\mathbf{k}}B_{\mathbf{k}}^* - B_{\mathbf{k}}D_{\mathbf{k}}^*)^2}. \tag{5.15}$$

The quantum correction E_{qu} is not uniform over the classical ground state manifold. It breaks the classical degeneracy and selects a subset of the classical manifold as the quantum ground state, by an 'order by disorder' mechanism[112]. Minimizing E_{qu} over the classical manifold, we find the following results for $\mathbf{Q}^{**}$, the spiral wavevector selected by quantum fluctuations. The associated ϕ^{**} is determined by Eqns. 5.7, 5.8.

For $1/6 < J_2/J_1 < 1/2$: The ground state is a spiral state S_1, with

$$\begin{aligned}
Q_b^{**} &= \cos^{-1}(\frac{J_1^2}{16J_2^2} - \frac{5}{4}), \\
Q_a^{**} &= 0.
\end{aligned} \tag{5.16}$$

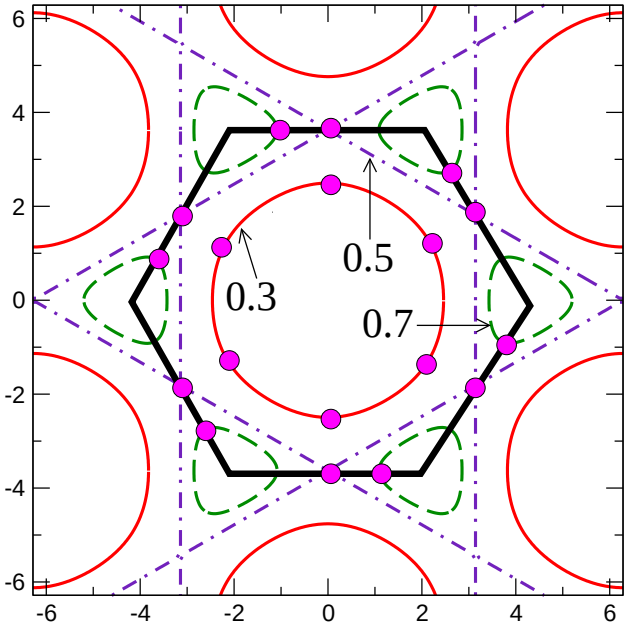

Figure 5.4: Order by disorder: For each value of $J_2/J_1 > \frac{1}{6}$, quantum fluctuations pick six distinct spirals from the classical ground state manifold. The selected spiral wavevectors are indicated by purple (solid) dots for $J_2/J_1 = 0.3$, 0.5 and 0.7.

While the above relations specify a single spiral state, there are a total of six symmetry related spirals, the other five being obtained by $2\pi/6$ rotations of the above $\mathbf{Q}^{**}$. As J_2/J_1 is increased from 1/6 to 1/2, the wavevector $\mathbf{Q}^{**}$ moves from the centre of the Brillouin zone towards an edge centre (see Fig. 5.4).

For $1/2 < J_2/J_1 < \infty$: The ground state is a spiral S_2, with

$$\begin{aligned} Q_b^{**} &= \pi - \cos^{-1}\left(\frac{J_1}{4J_2} + \frac{1}{2}\right), \\ Q_a^{**} &= 2\cos^{-1}\left(\frac{J_1}{4J_2} + \frac{1}{2}\right). \end{aligned} \tag{5.17}$$

There are six symmetry related S_2 spirals, the other five being obtained by $2\pi/6$ rotations of the above $\mathbf{Q}^{**}$. As J_2/J_1 is increased beyond 1/2, the wavevector $\mathbf{Q}^{**}$ moves from an edge centre along the edge towards a corner of the Brillouin zone (see Fig. 5.4).

The spin wave correction to the ground state energy is shown in Fig. 5.5. The sharp features at $J_2/J_1 \approx 1/6$ and 1/2 indicate transitions from Néel-S_1 spiral and S_1-S_2 spirals

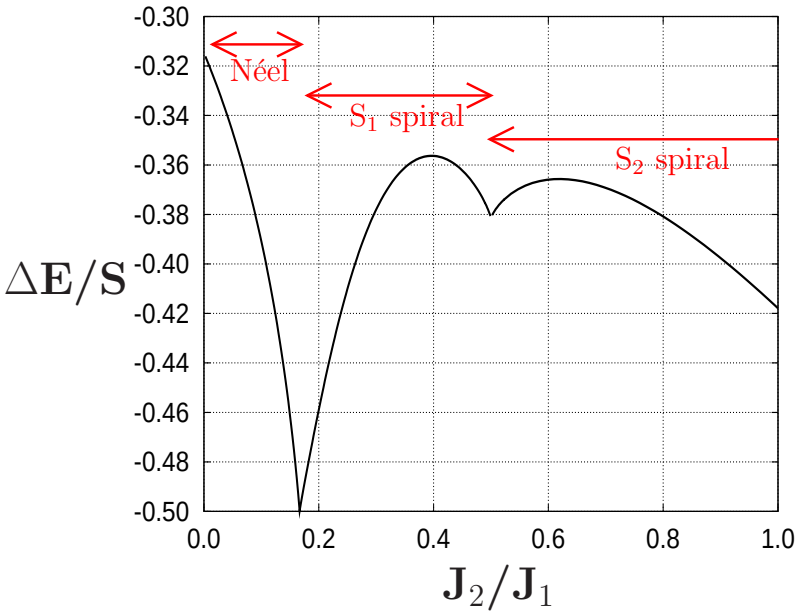

Figure 5.5: E_{qu}, quantum correction to ground state energy (in units of J_1) as a function of J_2/J_1. The nature of the ground state changes from Néel to S_1 spiral to S_2 spiral as described in the text.

respectively. When $J_2/J_1 \to \infty$, the honeycomb lattice decouples into two independent triangular lattices; in this limit we find that $Q_a^* = Q_b^* = 2\pi/3$, while ϕ^* is undetermined since spins on the two sublattices can be rotated independently.

5.4.1 Rotational symmetry breaking

In both S_1 and S_2 spirals, the quantum selected ground state appears to be six-fold degenerate. The ground state spirals come in three pairs of the form $\{(\mathbf{Q}^{**}, \phi^{**}), (-\mathbf{Q}^{**}, -\phi^{**})\}$, where we label spirals by the two parameters $\mathbf{Q}$ and ϕ as defined in Eq. 5.4. However, within each pair, the spirals $(\mathbf{Q}^{**}, \phi^{**})$ and $(-\mathbf{Q}^{**}, -\phi^{**})$ are not distinct as they are related by a global spin rotation. As can be seen from Eq. 5.4, rotating the spins by π about the Y axis is equivalent to the transformation $(\mathbf{Q}, \phi) \to (-\mathbf{Q}, -\phi)$.

Thus, after properly accounting for global spin-rotational symmetry, the quantum-selected ground state is three-fold degenerate with the three ground states related by $2\pi/3$ rotations of the lattice. The system will spontaneously break this three-fold ro-

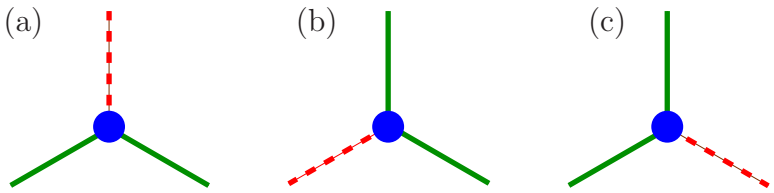

Figure 5.6: Lattice rotational symmetry breaking by quantum fluctuations: This figure shows the three nearest neighbour bonds of a site on the A-sublattice. (a), (b) and (c) correspond to the three spiral states selected by quantum fluctuations. $\mathbf{S}_i \cdot \mathbf{S}_j$ is the same on two bonds (shown with green solid lines) and different on the third (shown with red dashed line). Choosing one of (a), (b) and (c) is equivalent to choosing the direction of the 'unequal' bond.

tational symmetry of the honeycomb lattice at zero temperature by picking one of the three quantum-selected spirals. This three-fold symmetry breaking has a clear physical signature. A site of the honeycomb lattice has three nearest neighbour bonds, with each ground state spiral picking out one of these. This can be seen from the dot product $\mathbf{S}_i \cdot \mathbf{S}_j$ on the three nearest bonds of a site on sublattice A:

$$\mathbf{S}_A(\mathbf{r}) \cdot \mathbf{S}_B(\mathbf{r}) = -S^2 \cos\phi \tag{5.18}$$

$$\mathbf{S}_A(\mathbf{r}) \cdot \mathbf{S}_B(\mathbf{r} - \hat{b}) = -S^2 \cos(Q_b - \phi) \tag{5.19}$$

$$\mathbf{S}_A(\mathbf{r}) \cdot \mathbf{S}_B(\mathbf{r} - \hat{a} - \hat{b}) = -S^2 \cos(Q_a + Q_b - \phi). \tag{5.20}$$

In both S_1 and S_2 spirals, we find that two of these bond objects are equal, while the third bond is not, as shown in Fig. 5.6. The three-fold degeneracy of the ground state corresponds to the three ways of choosing this unequal bond direction. We note that these local correlations of $\mathbf{S}_i \cdot \mathbf{S}_j$ are invariant under lattice translations. Thus, for $J_2/J_1 > 1/6$, quantum fluctuations lead to a spiral ground state that breaks lattice rotational symmetry. If spiral magnetic order is lost due to long-wavelength fluctuations, the resulting state is a 'lattice nematic'. For small values of S, we expect quantum fluctuations to give rise to a lattice nematic ground state.

5.4.2 Stability of spiral order

Apart from selecting specific wavevectors, spin wave fluctuations will also renormalize spiral order, and may even render the spiral states unstable. Within our spin wave analysis, the leading spin wave correction to the spiral order parameter is given by

$$S - \frac{1}{N/2}\sum_{\mathbf{r}}\langle \tilde{S}^z_\nu(\mathbf{r})\rangle = \frac{1}{N/2}\sum_{\mathbf{k}}\langle b^\dagger_\nu(\mathbf{k}) b_\nu(\mathbf{k})\rangle, \tag{5.21}$$

where N is the total number of sites in the honeycomb lattice. We find that this correction diverges as $\log(N)$ since the spin wave energy vanishes on the entire classical manifold of degenerate spiral wavevectors. This line zero of the Holstein Primakoff spin waves ('Bose surface') is not protected by any symmetry arguments. We only expect to have gapless modes at the quantum-selected wavevectors. Spin-wave interactions, which we have ignored, may therefore gap out the spin waves at all other wavevectors and stabilize the spiral state for large enough S. For small spin values, however, spin wave fluctuations may 'melt' the spiral order, possibly leading to other competing phases. The resulting state may retain the Bose surface leading to interesting consequences[113].

5.5 Weak thermal fluctuations

In this section, we consider thermal fluctuations of spins about the classical spiral state. As our system is two-dimensional, any non-zero temperature will restore spin rotational symmetry and wipe out spiral order, in accordance with the Mermin-Wagner theorem. However, if the zero-temperature ground state breaks a discrete symmetry in addition to spiral order, there could still be a finite-temperature phase transition associated with discrete symmetry-breaking. Such phase transitions are known to occur on the square lattice $J_1 - J_2$[33] and $J_1 - J_3$[108] model. In both these cases, the ground state is a spiral which also breaks an Ising symmetry thereby leading to a finite temperature Ising-like phase transition. These Ising-like phase transitions may be understood as follows. At

finite temperature, the system traverses through state space as a function of time. The softer the fluctuations about a particular state, the system will spend more time in its vicinity[114]. If there are two such states α and β which allow for the greatest entropy, the system will remain in the vicinity of one of them, say α. The soft fluctuations about α may wash out any magnetic order that existed at zero temperature. Yet, at finite temperature, there is a residual tendency to stay in the vicinity of α rather than β. Above the phase transition temperature, this preference for one of the states vanishes.

In the honeycomb lattice case, the spiral ground state breaks three-fold lattice rotational symmetry and will similarly have a finite-temperature phase transition. We consider the low-temperature limit in which deviations from the classical ground state are small. Within the canonical ensemble picture, we evaluate the free energy of fluctuations about each classical ground state. The state(s) with minimum free energy allow for the highest entropy gain.

Assuming the system is in one of classical ground states, the spin at a site will point in the direction given by the spiral order, which we call this the local $\tilde{Z}$ axis. Upon including thermal fluctuations, there are two degrees of freedom for the spin vector corresponding to θ and ϕ directions (in standard spherical co-ordinates). The partition function of the system is given by

$$Z = \sum_{\text{config.}} \exp\left[-\beta E_{config.}\right] = \int \mathcal{D}\{\theta_i\}\mathcal{D}\{\phi_i\} exp\left[-\beta E_{\{\theta_i\},\{\phi_i\}}\right]. \tag{5.22}$$

We denote a fluctuation configuration as $\{\theta_1, \phi_1, \theta_2, \phi_2, \ldots, \theta_N, \phi_N\}$, where θ_i, ϕ_i are the displacement angles at site i. We denote the energy of this configuration by $E_{\{\theta_i\},\{\phi_i\}}$. In the low temperature limit, only configurations with small energy cost will contribute. As θ_i and ϕ_i are small, we take our $E_{\{\theta_i\},\{\phi_i\}}$ to be a quadratic function of the displacement angles (there are no linear terms as we are in a classical equilibrium state). To compute the free energy, we go to a basis in which $E_{\{\theta_i\},\{\phi_i\}}$ is diagonal.

$$Z = \int \mathcal{D}\{x_j\} exp\left[-\beta\left(x_j \lambda_j x_j\right)\right]. \tag{5.23}$$

where x_j's are the co-ordinates in the new basis and λ_j are the corresponding eigenenergies. As only small fluctuations contribute, we approximate the limits of x_j to be $(-\infty, \infty)$. This allows us to evaluate this free energy using Gaussian integrals,

$$Z \approx \prod_j \sqrt{\frac{\beta}{\lambda_j}}, \tag{5.24}$$

ignoring multiplicative constants. The free energy is given by

$$F = -\frac{1}{\beta} \ln Z \approx \sum_j \ln(\lambda_j). \tag{5.25}$$

The eigenenergies λ_j are simply the spin wave energies evaluated in large-S quantum case in Eq. 5.13. The generalized co-ordinates x_j are spin wave amplitudes. The Holstein-Primakoff approach further quantizes these fluctuations, but here we only require the eigenenergies. The free energy selects six spiral wavevectors from the classical manifold as follows:

For $1/6 < J_2/J_1 \lesssim 0.237$: The thermally selected wavevector $\mathbf{Q}^{th}$ lies on the line joining the Γ point to a K point (Brillouin zone centre to the Brillouin zone corner).

For $0.237 \lesssim J_2/J_1 \lesssim 0.549$: $\mathbf{Q}^{th}$ coincides with $\mathbf{Q}^{**}$ obtained in the case zero-temperature weak-quantum fluctuations (large-S Holstein Primako result).

For $J_2/J_1 \gtrsim 0.549$: $\mathbf{Q}^{th}$ again lies on the line joining the Γ point to a K point. In the limit of very large J_2/J_1, $\mathbf{Q}^{th}$ approaches the K point.

Irrespective of the location of $\mathbf{Q}^{th}$, thermal fluctuations select six symmetry related wavevectors. All the arguments of Sec. 5.4.1 also hold here. Accounting for global spin rotation symmetry, there are three distinct spiral states with minimum free energy. The object $\mathbf{S}_i \cdot \mathbf{S}_j$ is equal along two nearest neighbour bonds but not on the third. The three chosen spirals correspond to the three choices for the unique bond. Thus, as long as $J_2/J_1 > 1/6$, the thermal state breaks lattice rotational symmetry which is a discrete symmetry in the same universality class as the 3-state Potts model[115]. Thus, we expect the classical honeycomb $J_1 - J_2$ model to exhibit a thermal phase transition in the 3-state

Potts model universality class. This has been confirmed by a Landau theory analysis and classical Monte Carlo simulations done by A. Paramekanti[66].

5.6 Extreme quantum case: Nematic VBS

For large values of J_2/J_1, we have seen that the ground state of the classical model is highly degenerate. Weak quantum and thermal fluctuations break this degeneracy in such a way as to break the lattice rotational symmetry of the honeycomb lattice. In this section, we demonstrate that strong quantum fluctuations may also result in lattice nematic order. For the case of spin-1/2 where quantum fluctuations are largest, we propose a 'Nematic Valence Bond Solid' (NVBS) ground state which is the natural analogue of the large-S lattice nematic state. This state consists of singlet dimers arranged on the honeycomb lattice as shown in Fig. 5.7(a). There are three possible arrangements related by a $2\pi/3$ rotation of the lattice, depicted in Fig. 5.7(a-c). The NVBS state has been discussed earlier on the basis of an exact diagonalization study[111] in the vicinity of $J_2 = 0.4J_1$.

An alternate way to understand this NVBS state is to think of it as arising from coupling together frustrated spin $S = 1/2$ J_1-J_2 chains, as shown in Fig. 5.7(d). If we imagine the interchain couplings being tuned to zero, this would lead to decoupled Majumdar-Ghosh chains[116], which are known to possess dimer order with a spin gap. In particular, the dimerized state is the exact ground state of the single chain at $J_2 = 0.5J_1$. The NVBS arises from incorporating interchain couplings while leaving the singlet gap intact. The choice of the direction along which these chains run is arbitrary, so that there are three degenerate ground states that break lattice rotational symmetry. This state has been discussed earlier as the exact ground state of a Heisenberg model with multispin interactions[117].

With singlet dimers arranged on the the indicated bonds, the lowest energy excitations

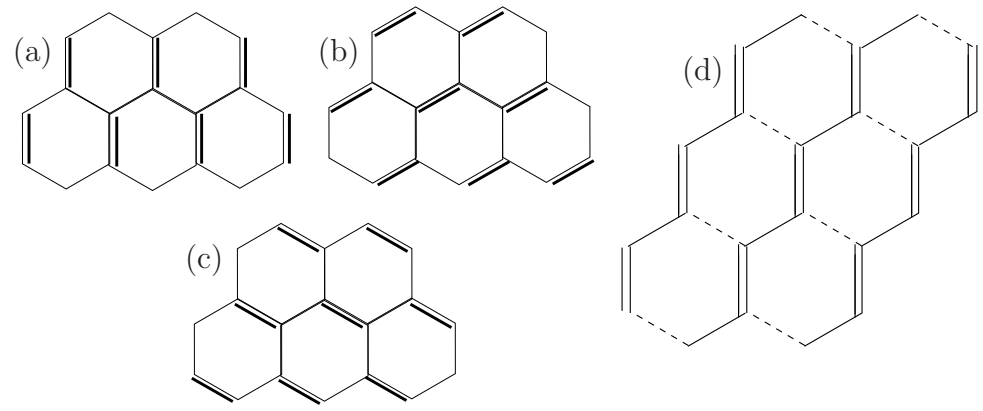

Figure 5.7: 'Nematic Valence Bond Solid' (NVBS) - the double bonds represent singlet correlations. This state preserves spin rotational and translation symmetries. Along single bonds, spins are uncorrelated. (a), (b) and (c) are three degenerate states related by $2\pi/3$ lattice rotations. (d) shows the NVBS state as being composed of Majumdar-Ghosh chains, coupled by the dashed bonds.

correspond to breaking the singlets to form triplets. The triplets can then disperse forming a 'triplon' band. The energetics and stability of such a dimer state with triplon excitations is naturally studied using the bond operator formalism proposed in Ref.[91], as follows. Instead of working in the naïve basis of $S = 1/2$ operators on every site, we switch to a basis of singlet and triplet bosonic operators defined as

$$\begin{aligned} s^\dagger|0\rangle &= \frac{1}{\sqrt{2}}(|\uparrow\downarrow\rangle - |\downarrow\uparrow\rangle) \\ t_x^\dagger|0\rangle = \frac{-1}{\sqrt{2}}(|\uparrow\uparrow\rangle - |\downarrow\downarrow\rangle); \quad t_y^\dagger|0\rangle &= \frac{i}{\sqrt{2}}(|\uparrow\uparrow\rangle + |\downarrow\downarrow\rangle); \quad t_z^\dagger|0\rangle = \frac{1}{\sqrt{2}}(|\uparrow\downarrow\rangle + |\downarrow\uparrow\rangle), \end{aligned}$$

on the double (dimer) bonds in Fig. 5.7(a). Equivalently, we could define these operators on the dimer bonds of Fig. 5.7(b,c). The vacuum $|0\rangle$ is not a physical state. It can be shown that spin commutation relations are preserved when the singlets and triplets are taken to be obey Bose statistics. To preserve the Hilbert space, we have a local constraint

$$s_{\mathbf{r}}^\dagger s_{\mathbf{r}} + \sum_{\alpha=x,y,z} t_{\mathbf{r},\alpha}^\dagger t_{\mathbf{r},\alpha} = 1. \tag{5.26}$$

We will satisfy this constraint on average, using a Lagrange multiplier μ to tune boson

occupancy. The original spin operators can be rewritten in terms of these singlet/triplet operators as

$$\hat{S}_{\{i,\nu=A,B,\gamma=x,y,z\}} = \frac{(-1)^{\nu}}{2}(s_i^{\dagger}t_{i,\gamma} + s_i t_{i,\gamma}^{\dagger}) - \frac{i}{2}\sum_{\beta,\delta=x,y,z}\epsilon_{\gamma\beta\delta}t_{i,\beta}^{\dagger}t_{i,\delta}, \tag{5.27}$$

where $(-1)^{\nu}$ is -1 when $\nu = A$ and $+1$ when $\nu = B$. $\epsilon_{\gamma\beta\delta}$ is the Levi-Civita symbol. The NVBS state is described by the Bose condensation of singlet bosons, allowing us to replace the operator s_i with a number $\bar{s}$ close to unity . Thus, on every dimerized bond, the probability of finding singlet correlations is $\bar{s}^2$. The probability of having a triplet is $1-\bar{s}^2$, a small number. The $J_1 - J_2$ Hamiltonian can be rewritten using this expression for the spin operators. The resulting terms can be arranged as

$$H = \bar{s}^2 L_{tt} + \bar{s} M_{ttt} + N_{tttt}. \tag{5.28}$$

The terms in L_{tt}, M_{ttt} and N_{tttt} are respectively quadratic, cubic and quartic in triplet operators. As the ground state has a very low density of triplets, terms with larger number of triplet operators are progressively less important. As a first step, we only keep the quadratic L_{tt} terms. This is the conventional bond-operator mean-field approach[91] which is known to work well in other contexts[84, 76]. The Hamiltonian in momentum space is given by

$$H_{BO}^{[2]} = C + \sum_{\mathbf{k}>0}\begin{bmatrix} t_{\gamma}^{\dagger}(\mathbf{k}) & t_{\gamma}(-\mathbf{k}) \end{bmatrix}\begin{bmatrix} G_{\mathbf{k}} & F_{\mathbf{k}} \\ F_{\mathbf{k}}^{*} & G_{\mathbf{k}} \end{bmatrix}\begin{bmatrix} t_{\gamma}(\mathbf{k}) \\ t_{\gamma}^{\dagger}(-\mathbf{k}) \end{bmatrix}.$$

where μ is the Lagrange multiplier introduced to satisfy the constraint in Eq. 5.26. The terms in the Hamiltonian are given by

$$\begin{aligned} G_{\mathbf{k}} &= \frac{J_1}{4} - \mu - \frac{\bar{s}^2}{4}J_1(\epsilon_{\mathbf{k}} + \epsilon_{-\mathbf{k}}) + \frac{\bar{s}^2}{4}J_2(\eta_{\mathbf{k}} + \eta_{-\mathbf{k}}) \\ F_{\mathbf{k}} &= -\frac{\bar{s}^2}{4}J_1(\epsilon_{\mathbf{k}} + \epsilon_{-\mathbf{k}}) + J_2\frac{\bar{s}^2}{4}(\eta_{\mathbf{k}} + \eta_{-\mathbf{k}}) \\ C &= -\frac{3N}{4}J_1\bar{s}^2 - N\mu\bar{s}^2 + N\mu - 3\sum_{\mathbf{k}>0}G_{\mathbf{k}}, \end{aligned} \tag{5.29}$$

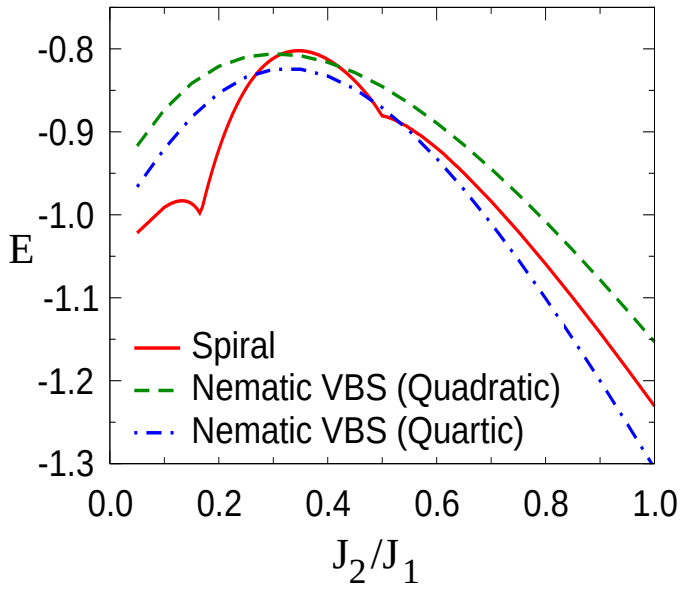

Figure 5.8: Ground state energy (in units of J_1) as a function of J_2/J_1. The red (solid) line is the energy of the spiral state including leading order spin wave corrections, the green (dashed) line is the NVBS energy up to quadratic order in triplon operators, and the blue (dash-dotted) line indicates NVBS energy up to quartic order in triplon operators

where

$$\begin{aligned} \epsilon_{\mathbf{k}} &= e^{-ik_b} + e^{-i(k_b+k_a)} \\ \eta_{\mathbf{k}} &= 2[\cos(k_a) + \cos(k_b) + \cos(k_a + k_b)]. \end{aligned}$$

Diagonalizing the Hamiltonian by a bosonic Bogoliubov transformation gives the dispersion the 'triplon' modes:

$$E_k = \sqrt{G_k^2 - |F_k|^2}. \tag{5.30}$$

The energy of NVBS state obtained from Eq. 5.29 is plotted as the green dashed line in Fig. 5.8. While this quadratic theory gives a consistent picture of our lattice nematic state, higher order terms may lower its energy significantly. We take these into account by means of a self consistent Hartree-Fock approach[91],[118]. This approach has been shown to work well on the star lattice wherein it gives results that reconcile exact-diagonalization and Gutzwiller-projected wavefunction studies[119],[120]. The terms in

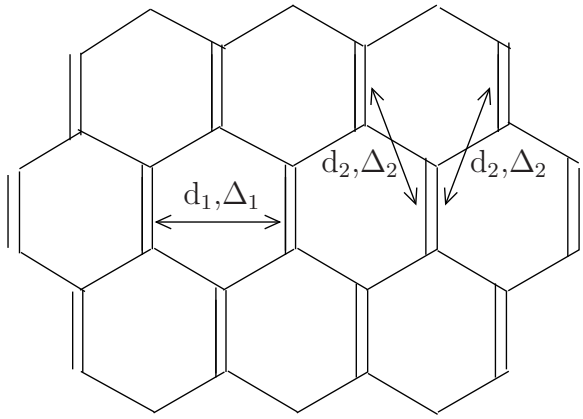

Figure 5.9: Quartic bond operator theory: $d_{1,2}$ and $\Delta_{1,2}$ are Hartree-Fock-Bogoliubov mean field parameters in the bond operator mean field theory (see text for details). These operators are defined between bonds as shown.

M_{ttt}, of cubic order, do not contribute in this scheme since we assume that the triplon operators themselves are not condensed. The quartic part of the Hamiltonian is given by

$$H_{BO}^{[4]} = \frac{-1}{2N} \sum_{\mathbf{k},\mathbf{k}',\mathbf{q}} \epsilon_{\mu\beta\gamma}\epsilon_{\mu\kappa\delta}(J_1\epsilon_{\mathbf{k}-\mathbf{k}'} + J_2\eta_{\mathbf{k}-\mathbf{k}'})t^\dagger_\beta(\mathbf{k}+\mathbf{q})t_\gamma(\mathbf{k}'-\mathbf{q})t^\dagger_\kappa(\mathbf{k}')t_\delta(\mathbf{k}).$$

Guided by the symmetry of the NVBS phase, we postulate the following real-space order parameters:

$$d_1 = \frac{1}{3}\langle t^\dagger_{\mathbf{r},\gamma} t_{\mathbf{r}+\delta_1,\gamma}\rangle; \quad d_2 = \frac{1}{3}\langle t^\dagger_{\mathbf{r},\gamma} t_{\mathbf{r}+\delta_2,\gamma}\rangle \tag{5.31}$$

$$\Delta_1 = \frac{1}{3}\langle t_{\mathbf{r},\gamma} t_{\mathbf{r}+\delta_1,\gamma}\rangle; \quad \Delta_2 = \frac{1}{3}\langle t_{\mathbf{r},\gamma} t_{\mathbf{r}+\delta_2,\gamma}\rangle \tag{5.32}$$

where $\delta_1 = \pm\hat{a}$, and $\delta_2 = \pm\hat{b}, \pm(\hat{a}+\hat{b})$. These order parameters are defined on bonds as shown in Fig. 5.9. They are the only bilinears that couple to $\bar{s}^2$ at quadratic level. We calculate these order parameters d_1, d_2, Δ_1 and Δ_2 self-consistently, and thereby obtain the energy of the NVBS. This is plotted in Fig. 5.8 as the blue (dot-dashed) line.

Fig. 5.8 compares the energy of the NVBS state with the energy of the spiral state. The energy of the spiral state in the figure includes spin-wave corrections, setting $S = 1/2$. Although spin wave fluctuations are calculated in the large-S limit, the Holstein-Primakoff approach is known to work reasonably well even for S=1/2[49, 50]. We have ignored

spin-wave interactions which may somewhat renormalize the energy of the spiral state. At quadratic level, the NVBS phase is energetically favoured over the spiral in a small window near $J_2 \sim 0.35J_1$. Upon including quartic corrections, the energy of the NVBS state is lower than that of the spiral state for $J_2 \gtrsim 0.25J_1$, except for a small window around $J_2 = 0.5J_1$. Since the spiral order is anyway likely to be suppressed by low-lying spin wave modes, our results suggest NVBS order over a wide window of frustration.

We note that this bond operator formalism does not take into account the fluctuations of the singlets themselves; the kinetic energy lowering from such resonating singlet valence bonds might favor plaquette order as indicated by some exact diagonalization studies[36, 34].

5.7 Relation to previous work

Earlier investigations have considered various aspects of the honeycomb lattice $J_1 - J_2$ model. The classical phase diagram has been discussed within an extended $J_1 - J_2 - J_3$ model[121, 111]. Our work has built upon these calculations by systematically including quantum and thermal fluctuations. A later calculation of thermal fluctuations using classical Monte Carlo simulations[67] agrees well with our results.

We have shown that in various limits, weak thermal/quantum fluctuations lead to lattice nematic order, similar to the case of the square lattice $J_1 - J_2$ and $J_1 - J_3$ models. The main differences of our honeycomb lattice problem compared with these cases are:

(i) The classical ground degeneracy in the square $J_1 - J_2$ model arises from the arbitrary relative orientation between Néel vectors of each sublattice. In the square $J_1 - J_3$ model, the classical ground state is only doubly degenerate. In contrast, in the honeycomb problem, the classical ground state manifold is a one-parameter family of distinct spirals. As a consequence, the spin wave spectrum is gapless at all classical ordering wavevectors, leading to a 'Bose surface'. Although the Bose surface could be

destroyed by spin-wave interactions, we expect it to be stable atleast at large S. Apart from making the honeycomb spiral more susceptible to quantum melting, such a Bose surface is interesting in its own right[113].

(ii) While the square lattice models give rise to Ising symmetry breaking, the honeycomb model breaks a threefold rotational symmetry and is in the same universality class as a 3-state Potts model.

(iii) There is no simple $S = 1/2$ quantum analogue of the nematic states on the square lattice. On the other hand, the honeycomb nematic smoothly maps onto the Nematic Valence Bond Solid state in the extreme quantum limit.

In the $S = 1/2$ case, the honeycomb lattice $J_1 - J_2$ model has been extensively studied in the context of the honeycomb lattice Hubbard model. Quantum Monte Carlo studies have hinted that the Hubbard model at intermediate coupling has a spin-liquid ground state. Approaching this spin liquid phase from the strong coupling limit, the $J_1 - J_2$ model is expected to capture the relevant physics. Exact diagonalization studies[36, 34] and variational Monte Carlo calculations[100] have confirmed our prediction of an NVBS ground state for $J_2/J_1 \gtrsim 0.3$. In Chapter 6, we will discuss the implications of our results in the context of the material $Bi_3Mn_4O_{12}(NO_3)$.

Chapter 6

Field-induced Néel order on the honeycomb lattice

6.1 Introduction

In the previous two chapters, we have discussed two models of antiferromagnetism on the honeycomb lattice - next-nearest neighbour exchange and bilayer coupling. Both models embody competition between Néel and non-Néel phases - next-nearest neighbour exchange leads to spiral ground states with lattice nematic order, while bilayer coupling gives rise to an interlayer dimer state that does not break any symmetries. In this chapter, we examine these models in an applied magnetic field. We show that both these models, within some parameter range, show field-induced Néel order. Thus, an applied field provides an additional axis to tune competition between Néel and non-Néel orders. We place our discussion in the context of experiments on $Bi_3Mn_4O_{12}(NO_3)$(BMNO). We point out connections to numerical investigations of the honeycomb lattice Hubbard model which indicate a possible spin liquid ground state at intermediate interaction strengths.

The recently synthesized $S = 3/2$ antiferromagnet BMNO is believed to have a mag-

netically disordered ground state[61, 62, 65](see Chapter 4 for an overview) . At a critical applied magnetic field, it undergoes a phase transition into Néel order. The experiments on BMNO raise two questions:

(i) What frustrates Néel order in BMNO?

(ii) How does the applied field induce Néel order?

We begin this chapter by discussing bilayer coupling as a route to suppressing Néel order. When the bilayer coupling is large enough, an interlayer dimer state arises. Field-induced Néel order arises due to Bose-condensation of triplon excitations. However, this scenario is unlikely to be relevant to BMNO as a very large bilayer coupling is required to stabilize the interlayer dimer state. We then discuss frustration due to next-nearest neighbour exchange. Within a quantum-melting picture, this scenario can explain the disordered ground state and field-induced Néel order. We point out connections to numerical studies of the honeycomb lattice Hubbard model. Finally, we comment on the role of disorder in BMNO.

6.2 Bilayer coupling

The Mn sites in a unit cell of $Bi_3Mn_4O_{12}(NO_3)$ form an AA stacked bilayer honeycomb lattice. If the interplane antiferromagnetic exchange J_c is large compared to J_1, adjacent spins on the two layers will dimerize as shown in Fig.6.1, leading to loss of Néel order. We study this scenario in the simplified $J_1 - J_c$ model, ignoring other exchange interactions in the honeycomb plane. Chapter 4 presents a detailed analysis of this interlayer dimer state using the bond-operator formalism. In the limit of large J_c/J_1, each interlayer bond becomes independent with the spectrum $E_j = -J_c(S(S+1) - j(j+1)/2)$, with $j = 0, 1, \ldots, 2S$ denoting the total spin state of the bond. We are primarily interested in the dimer-Néel transition which is driven by condensation of triplon modes. Keeping this in mind, we restrict our attention to the low energy Hilbert space spanned by the

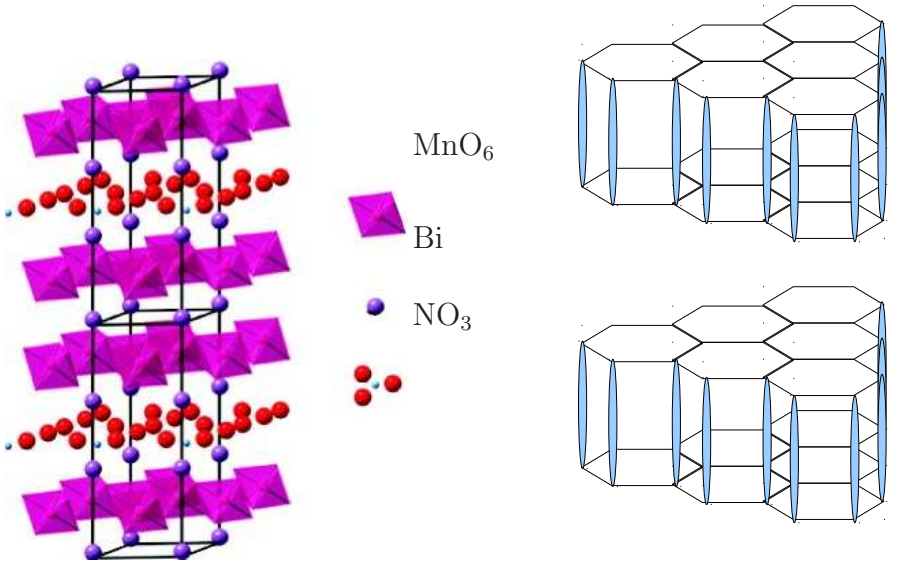

Figure 6.1: Left: Crystal structure of BMNO, showing bilayer nature. Reprinted with permission from JACS **131**, 8313 ©2009 American Chemical Society. Right: Cartoon picture of interlayer VBS state (blue ellipsoids indicate bonds with singlet correlations).

singlet($j = 0$) and triplet($j = 1$) states. This will suffice for our purpose of demonstrating field-induced Néel order, with higher energy quintet states only renormalizing the location of the critical transition point.

Within a single bilayer, we denote an interlayer bond as $\{i, \nu\}$, where i labels the unit cell of the honeycomb lattice and $\nu = A, B$ is the sublattice index. Each bond can be in a singlet or a triplet state, denoted as

$$|s\rangle_{i,\nu}, \quad |t_0\rangle_{i,\nu}, \quad |t_{+1}\rangle_{i,\nu}, \quad |t_{-1}\rangle_{i,\nu}. \tag{6.1}$$

We label the triplet states as $|t_m\rangle$ where $m = -1, 0, 1$ is the z-component of the spin angular momentum.

The bond-operator formalism replaces each of these singlet and triplet states with a boson, with the constraint that the number of bosons on an interlayer bond should be unity. The interlayer dimer state is described by a uniform Bose-condensate of the singlet bosons, while excitations about this state correspond to breaking singlets to form

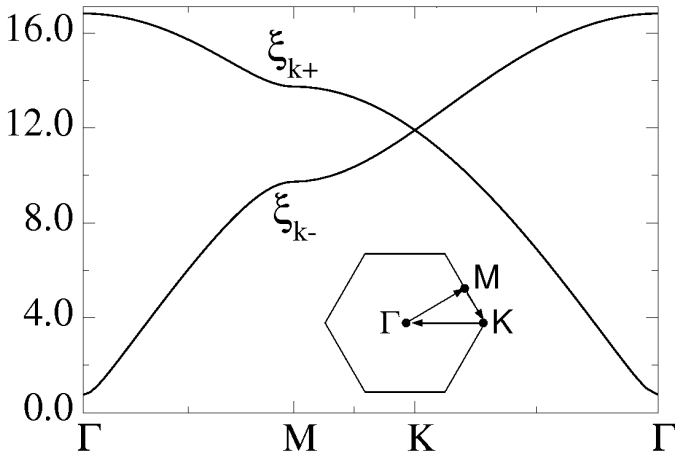

Figure 6.2: Triplon dispersion along depicted path in the Brillouin zone in the interlayer dimer state for$S = 3/2$ and $J_c/J_1 = 3.8$ (in units where $J_1 = 1$).

triplets. As the energy cost of making a triplet is $\sim J_c$, there is an energy gap to forming triplets. These triplet bosons disperse over the lattice and form 'triplon' bands. At the level of bond-operator mean-field theory, the dispersion of these triplon excitations is given by Eq. 4.13 of Chapter 4.

Fig. 6.2 shows the triplon dispersion in the dimer phase, obtained using bond-operator mean-field theory, for the case of $S = 3/2$, relevant to BMNO. We ignore triplet-triplet interactions and quintet corrections - we assume that the location of the minimum in the triplet bands is not affected by these corrections terms. As can be seen from Fig. 6.2, the lowest triplon excitation occurs at $\mathbf{k} = 0$ (the Γ point). When a magnetic field $B\hat{z}$ is applied, the singlet bosons are unaffected. However, the triplets being $S = 1$ objects, acquire a Zeeman shift in energy given by $\Delta E = -mB$, where $m = -1, 0, 1$ is the z-component of spin angular momentum. The triplet state with $m = +1$ is lowered in energy. At a critical magnetic field, this triplet mode becomes gapless and also undergoes Bose-condensation. The resulting state has Néel order, which can be seen as follows.

The $m = +1$ triplet with wavevector Bose-condenses at the wavevector $\mathbf{k} = 0$, which corresponds to uniform condensation within a sublattice. From the expressions for the

eigenvectors(derived in Appendix C.3), we see that the condensing triplet eigenvector has opposite signs on the two sublattices. The resulting state at bond $\{i,\nu\}$ is a linear combination of the singlet and the $(m=+1)$ triplet. Up to an overall phase, we may write

$$|\psi\rangle_{i,\nu} \approx |s\rangle_{i,\nu} + (-1)^{\nu} c_0 e^{i\phi} |t_{+1}\rangle_{i,\nu}. \tag{6.2}$$

where $(-1)^{\nu}$ is 1 when $\nu = A$ and -1 when $\nu = B$. The quantity $(-1)^{\nu} c_0 e^{i\phi}$ is the amplitude of the triplet condensate. The amplitude comes with a factor of $(-1)^{\nu}$ since the condensing eigenvector has opposite signs on the two sublattices. Within the singlet-triplet sector, the spin operators are given by

$$\begin{aligned} S^{+}_{i,\ell} &= (-1)^{\ell}\sqrt{\frac{2S(S+1)}{3}}\{s_i^{\dagger}t_{i,-1} - s_i t_{i,1}^{\dagger}\} + \frac{1}{\sqrt{2}}\{t_{i,1}^{\dagger}t_{i,0} + t_{i,0}^{\dagger}t_{i,-1}\}, \\ S^{z}_{i,\ell} &= (-1)^{\ell}\sqrt{\frac{S(S+1)}{3}}\{s_i^{\dagger}t_{i,0} + s_i t_{i,0}^{\dagger}\} + \frac{1}{2}\{t_{i,1}^{\dagger}t_{i,1} - t_{i,-1}^{\dagger}t_{i,-1}\}. \end{aligned}$$

Using this spin-wavefunction on a bond, we evaluate the following expectation values:

$$\begin{aligned} \langle S^{x}_{1/2}\rangle &\approx \mp(-1)^{\nu} c_0 \sqrt{S(S+1)}\cos(\phi), \\ \langle S^{y}_{1/2}\rangle &\approx \mp(-1)^{\nu} c_0 \sqrt{S(S+1)}\sin(\phi), \\ \langle S^{z}_{1/2}\rangle &\approx \frac{c_0^2}{2}. \end{aligned} \tag{6.3}$$

We have ignored multiplicative constants. As seen from these expressions, triplon condensation leads to Néel order within the XY plane along with uniform polarization along the Z axis. The phase of the triplon condensate ϕ determines the orientation of Néel ordering within the plane.

We have shown that the interlayer dimer state undergoes a field-induced Néel transition. With respect to BMNO, bilayer coupling can therefore account for (i) the absence of long range order and for field-induced Néel ordering. However, as we show in Chapter 4, we need a large value of bilayer coupling to stabilize the dimer state. Within the $J_1 - J_c$ model, we need $J_c/J_1 \gtrsim 9$ to reach the dimer state(see Table. 4.2 in Chapter

4). If we include other exchange interactions in the honeycomb plane, the strength of bilayer coupling required may somewhat decrease. However, we don't expect it to change significantly. In BMNO, density functional calculations[63] estimate $J_c/J_1 \approx 2$. Even though this is fairly large, the value is much lower than that required for dimerization. Thus, we rule out bilayer coupling as the source of frustration in BMNO and discuss another possibility in the next section.

6.3 Nearest-neighbour exchange

Next nearest neighbour (J_2) exchange is the simplest interaction that can frustrate Néel order in a honeycomb plane. It is also the most plausible source of frustration in BMNO. Indeed, the $J_1 - J_2$ model has been discussed as a possible minimal model for BMNO[61, 67]. In this section, we examine whether the $J_1 - J_2$ model can explain (i) the absence of long range order at zero field, and (ii) field-induced Néel ordering.

In an applied magnetic field, we have the $J_1 - J_2 - B$ model:

$$H = J_1 \sum_{\langle ij \rangle} \mathbf{S}_i \cdot \mathbf{S}_j + J_2 \sum_{\langle\langle ij \rangle\rangle} \mathbf{S}_i \cdot \mathbf{S}_j - B \sum_i S_i^z, \tag{6.4}$$

where $\langle . \rangle$ and $\langle\langle . \rangle\rangle$ denote nearest and next-nearest neighbour bonds respectively, and B is a Zeeman field.

The classical analysis ($S = \infty$) at $B = 0$ is presented in Chapter 5. For $J_2/J_1 < 1/6$, the classical ground state is Néel ordered. When a magnetic field is applied (along Z axis), the spins start off in the XY plane and cant along the field direction until they are fully polarized at $B = B_{pol}$. This uniform canting leads to maximum energy lowering from the Zeeman term. As shown in Fig. 6.3, for $B < B_{pol}$, the spin components transverse to the magnetic field have staggered Néel order.

The canting of spins in an applied magnetic field is easily explained when the field strength is much lower than the exchange energy scales. To understand the classical ground state at large field strength, we study the fully polarized phase at large fields.

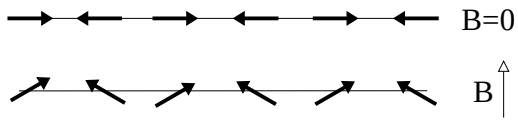

Figure 6.3: Canted Néel state: In an applied magnetic field, spins cant uniformly along the field. The components of the spin perpendicular to the applied field show Néel order.

As the magnetic field is lowered, magnon excitations of the ferromagnet come down in energy. At $B = B_{pol}$, the lowest lying magnon mode condenses leading to Néel or spiral order. For $J_2/J_1 < 1/6$, we have confirmed that the magnon modes condense at the wavevector corresponding to Néel order. For $J_2/J_1 > 1/6$, the condensing wavevectors correspond to the classical ground state manifold discussed in Chapter 5 for the $B = 0$ case. Thus, the classical ground state for $B < B_{pol}$ has canted Néel order for $J_2/J_1 < 1/6$ and canted spiral order for $J_2/J_1 > 1/6$. The classical phase diagram of the $J_1 - J_2 - B$ model is depicted in Fig.6.4.

For $J_2/J_1 > 1/6$, the ground state at $B=0$ is a spiral. As B increases, the spins in the spiral state cant uniformly along the applied field. In this chapter, we will not discuss the canted spiral state as it is not relevant to the physics of BMNO for the following reasons.

(i) The absence of long range order could be due to long wavelength fluctuations destroying spiral order in part of the spiral region in the classical phase diagram of Fig.6.4. However, in any part of the canted spiral region, an applied magnetic cannot give rise to Néel order.

(ii) Chapter 5 establishes that upon including quantum/thermal fluctuations, the spiral state breaks threefold lattice rotational symmetry. While magnetic order may be lost due to long wavelength fluctuations, there should be a thermal phase transition associated with rotational symmetry breaking. As no such transition is seen in BMNO[61], it is unlikely to be described by the $J_1 - J_2 - B$ model with $J_2/J_1 > 1/6$.

The regime $J_2/J_1 < 1/6$, corresponding to the classical canted Néel state, could be

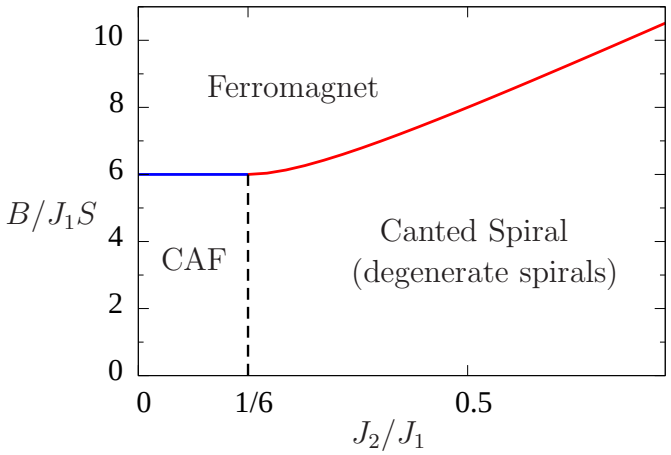

Figure 6.4: Phase diagram of the $J_1 - J_2 - B$ model on the honeycomb lattice in the classical limit. CAF stands for 'Canted Antiferromagnet'. The boundaries of the fully polarized ferromagnetic phase have been obtained from magnon condensation. Upon including quantum fluctuations in the canted spiral phase, the ground state is threefold degenerate and breaks lattice rotational symmetry as described in Chapter 5.

applicable to BMNO. We study quantum fluctuations around the canted Néel state to see if fluctuations can 'melt' magnetic order.

6.3.1 Spin-wave fluctuations

We now work with the assumption that quantum fluctuations 'melt' the order Néel in some part of the classical phase diagram, and we seek to find out if this melted phase can undergo field-induced Néel order. If we knew the nature of the melted phase, we could precisely determine the melting boundary in the $J_1 - J_2 - B$ phase diagram. As indicated in Fig.6.5, we could determine the in-field behaviour from a simple susceptibility calculation. However, as we do not know the state that results from quantum melting, we will use a heuristic criterion to determine the melting line.

In the classical limit, spins in the canted Néel state can be characterized by $\mathbf{S_r} = S(\mp\cos\chi, 0, \sin\chi)$ on the two sublattices of the honeycomb plane. We define new spin

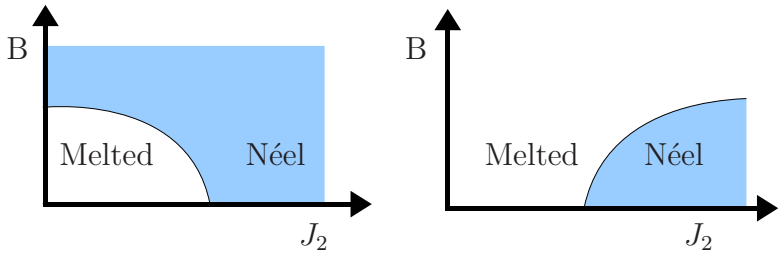

Figure 6.5: Magnetic susceptibility determines the in-field phase boundary: (Left) Phase boundary when $\chi_{N\acute{e}el} > \chi_{melted}$, (Right) Phase boundary when $\chi_{N\acute{e}el} < \chi_{melted}$.

operators, denoted by $\mathbf{T}_{i,\alpha}$, via a sublattice-dependent local spin rotation

$$\begin{pmatrix} T^x_{i,\nu} \\ T^y_{i,\nu} \\ T^z_{i,\nu} \end{pmatrix} = \begin{pmatrix} \sin\chi & 0 & -(-1)^\nu \cos\chi \\ 0 & 1 & 0 \\ (-1)^\nu \cos\chi & 0 & \sin\chi \end{pmatrix} \begin{pmatrix} S^x_{i,\nu} \\ S^y_{i,\nu} \\ S^z_{i,\nu} \end{pmatrix}, \tag{6.5}$$

where $\nu = A, B$, is a sublattice index and i sums over each unit cell. The term $(-1)^\nu$ is $+1$ when $\nu = A$ and -1 when $\nu = B$. In the new basis, the ground state is a ferromagnet with all spins pointing along the local T^z axis. To study spin wave fluctuations, we rewrite the T operators in terms of Holstein-Primakoff bosons as follows:

$$T^z_{i,\nu} = S - b^\dagger_{i,\nu} b_{i,\nu}; \quad T^x_{i,\nu} = \sqrt{\frac{S}{2}}(b_{i,\nu} + b^\dagger_{i,\nu}); \quad T^y_{i,\nu} = \frac{1}{i}\sqrt{\frac{S}{2}}(b_{i,\nu} - b^\dagger_{i,\nu}).$$

The Hamiltonian can be rewritten as $H \approx E_{Cl} + H_{qu}$. The classical energy E_{Cl} is proportional to S^2, and the leading order quantum correction, H_{qu}, arising from the zero-point energy of spin wave modes, is of order S. The classical energy is given by

$$E_{Cl} = NS^2 \left[-\frac{3}{2} J_1 \cos 2\chi + \frac{3}{2} J_2 - \frac{B}{S} \sin\chi \right]. \tag{6.6}$$

where N is the number of sites in the honeycomb lattice. We take the magnetic field B to be of order S, so that the Zeeman term $-BS^z_i$ is treated on the same level as the exchange terms $J_{ij}\mathbf{S}_i \cdot \mathbf{S}_j$.

The canting angle χ is set by demanding that terms of order $S^{3/2}$, which are linear in the boson operators, should vanish. Equivalently, demanding $\partial E_{CL}/\partial\chi = 0$ gives the

same result. We obtain

$$\sin\chi = \frac{B}{6J_1S}. \tag{6.7}$$

The field at which spins fully polarize is given by $B_{pol} = 6J_1S$, independent of J_2 (as long as $J_2 < 1/6$). This matches with the magnon-condensation result at large B, shown in Fig. 6.4. The leading quantum correction is given by

$$H_{qu} = -\frac{3NS}{2}J_1\cos 2\chi + 3NSJ_2 - \frac{NB}{2}\sin\chi + \sum_{\mathbf{k}>0}\psi^\dagger_{\mathbf{k}}H_{\mathbf{k}}\psi_{\mathbf{k}}, \tag{6.8}$$

where we have defined

$$\psi_{\mathbf{k}} = \begin{pmatrix} b_{\mathbf{k},A} \\ b_{\mathbf{k},B} \\ b^\dagger_{-\mathbf{k},A} \\ b^\dagger_{-\mathbf{k},B} \end{pmatrix}; \qquad H_{\mathbf{k}} = S\begin{pmatrix} I_{\mathbf{k}} & F_{\mathbf{k}} & 0 & G_{\mathbf{k}} \\ F^*_{\mathbf{k}} & I_{\mathbf{k}} & G^*_{\mathbf{k}} & 0 \\ 0 & G_{\mathbf{k}} & I_{\mathbf{k}} & F_{\mathbf{k}} \\ G^*_{\mathbf{k}} & 0 & F^*_{\mathbf{k}} & I_{\mathbf{k}} \end{pmatrix}. \tag{6.9}$$

The entries in the Hamiltonian matrix are given by

$$\begin{aligned} I_{\mathbf{k}} &= 3J_1\cos 2\chi - 6J_2 + 2J_2\{\cos k_a + \cos k_b + \cos(k_a + k_b)\} + \frac{B}{S}\sin\chi, \\ F_{\mathbf{k}} &= J_1\gamma_{\mathbf{k}}\sin^2\chi \equiv |F_{\mathbf{k}}|e^{i\eta_{\mathbf{k}}}, \\ G_{\mathbf{k}} &= -J_1\gamma_{\mathbf{k}}\cos^2\chi, \end{aligned}$$

where $\gamma_{\mathbf{k}} = 1 + \mathrm{e}^{-i\mathbf{k}\cdot\hat{b}} + \mathrm{e}^{-i\mathbf{k}\cdot(\hat{a}+\hat{b})}$, with unit vectors $\hat{a}$ and $\hat{b}$ as shown in Fig.5.2 of Chapter 5. This Hamiltonian can be diagonalized by a bosonic Bogoliubov transformation. The eigenvalues are given by

$$\Omega^{\pm}_{\mathbf{k}} = S\sqrt{(I_{\mathbf{k}} \pm |F_{\mathbf{k}}|)^2 - |G_{\mathbf{k}}|^2}. \tag{6.10}$$

The Bogoliubov transformation matrix is given by

$$P_{\mathbf{k}} = \begin{pmatrix} U_{2\times2} & 0 \\ 0 & U_{2\times2} \end{pmatrix}\begin{pmatrix} C_{2\times2} & S_{2\times2} \\ S_{2\times2} & C_{2\times2} \end{pmatrix},$$

where

$$U_{2\times 2}=\frac{1}{\sqrt{2}}\begin{pmatrix} -e^{i\eta_{\mathbf{k}}} & e^{i\eta_{\mathbf{k}}} \\ 1 & 1 \end{pmatrix}; \quad C_{2\times 2}=\begin{pmatrix} \cosh\theta_{\mathbf{k}} & 0 \\ 0 & \cosh\phi_{\mathbf{k}} \end{pmatrix}; \quad S_{2\times 2}=\begin{pmatrix} \sinh\theta_{\mathbf{k}} & 0 \\ 0 & \sinh\phi_{\mathbf{k}} \end{pmatrix} \tag{6.11}$$

The angles $\theta_{\mathbf{k}}$ and $\phi_{\mathbf{k}}$ are given by

$$\tanh 2\theta_{\mathbf{k}} = \frac{|G_{\mathbf{k}}|}{I_{\mathbf{k}} - |F_{\mathbf{k}}|}; \quad \tanh 2\phi_{\mathbf{k}} = \frac{-|G_{\mathbf{k}}|}{I_{\mathbf{k}} + |F_{\mathbf{k}}|}. \tag{6.12}$$

The matrix $P_{\mathbf{k}}$ preserves the commutation relations of the bosonic operators and diagonalizes the Hamiltonian, giving $P_{\mathbf{k}}^{\dagger} H_{\mathbf{k}} P_{\mathbf{k}} = \mathrm{Diag}\{\Omega_{\mathbf{k}}^{-}, \Omega_{\mathbf{k}}^{+}, \Omega_{\mathbf{k}}^{-}, \Omega_{\mathbf{k}}^{+}\}$. Fig.6.6 shows plots of the spin-wave dispersion in the Néel state along high symmetry directions in the Brillouin zone.

6.3.2 Melting of Néel order

For finite S, quantum fluctuations are likely to destabilize Néel order even for $J_2 < J_1/6$. As J_2 is increased from zero, quantum fluctuations about the Néel state increase. At some critical value of J_2, long wavelength fluctuations will wash out Néel order. Using spin wave theory, we argue that a small nonzero B enhances the stability of the Néel order compared to the zero field case.

(i) For small nonzero B, spin canting leads to a small decrease, $\propto B^2$, in the classical staggered magnetization transverse to the field.

(ii) On the other hand, one of the two magnon modes (labelled $\Omega_{\mathbf{k}}^{+}$) acquires a nonzero gap $\propto B$ at the Γ-point as shown in Fig.6.6. Thus, the applied field suppresses low-lying spin wave fluctuations. For $B \ll 6J_1S$, we will show that the latter effect overwhelms the former, leading to enhanced stability of Néel order.

To estimate the 'melting curve', we assume that the transverse spin components have Néel order along the S^x-direction. The conventional criterion for melting driven by spin-waves can be written as ($\langle S_{i,\nu}^x \rangle = 0$), i.e., magnetic order 'melts' when the magnitude of the ordered moment is renormalized to zero. Within spin wave theory, $\langle S_{i,\nu}^x \rangle$

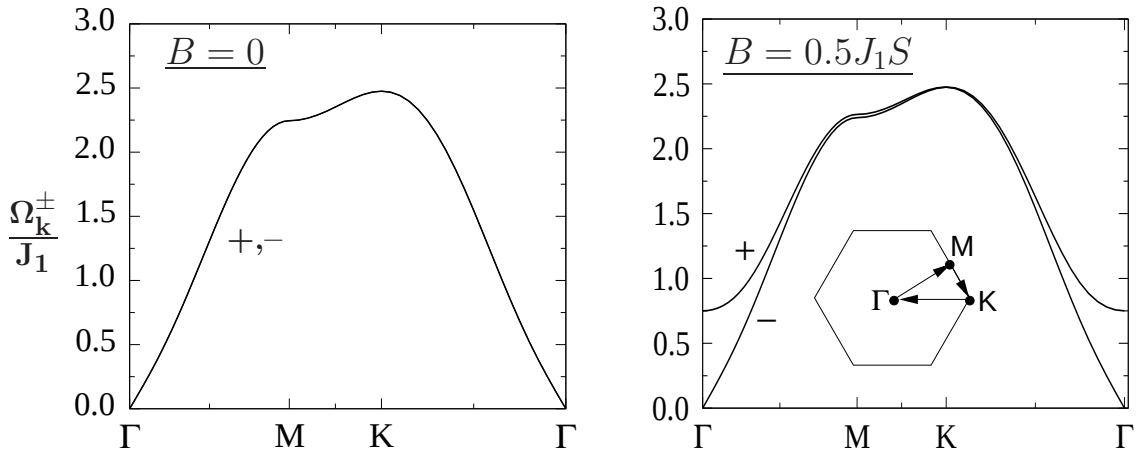

Figure 6.6: Spin-wave dispersion $\Omega_{\mathbf{k}}^{\pm}$ in the $J_1 - J_2 - B$ model along depicted path in the Brillouin zone for $J_2 = 0.15J_1$ and $S = 3/2$. Left: $(B = 0)$ - there are two Goldstone modes. Right: $(B = 0.5J_1S)$ - one low-lying mode acquires a gap due to the applied field.

(the component of the ordered moment normal to applied field) vanishes concurrently with $\langle S_{i,\nu}^z \rangle$ (component along applied field). Therefore, if we use this criterion, the state resulting from quantum melting will not have any polarization along the applied field direction. However, the ferromagnetic component along the applied field does not correspond to any symmetry breaking. We expect fluctuations to first wash out in-plane Néel ordering before killing the ferromagnetic component. Thus, we expect the conventional criterion to overestimate the critical value of J_2 required for melting.

Instead, we use a Lindemann-like criterion to describe melting: $(\sqrt{\langle S_x^2 \rangle - \langle S_x \rangle^2} \gtrsim \alpha \langle S_x \rangle)$, i.e., Néel order melts when the fluctuation in the in-plane moment is comparable to its magnitude. This is analogous to the Lindemann criterion used for melting of a crystal, which postulates that melting occurs when the deviation in position of an ion (due to thermal fluctuations) is comparable to lattice spacing[122]. Our criterion for melting of Néel order shares two features with the Lindemann criterion for crystals:

(i) It is a heuristic criterion, i.e., melting lines are only approximate and should not be treated as phase boundaries.

(ii) The criterion does not give any information about the state that results from melting. We expect the melting of Néel order to lead to a quantum disordered state such as a valence-bond solid or a spin liquid.

In evaluating the melting criterion ($\sqrt{\langle S_x^2\rangle - \langle S_x\rangle^2} \gtrsim \alpha\langle S_x\rangle$), we evaluate expectation values to order 1, even though the Hamiltonian has terms upto order S only. We set α=5 since this leads to melting of Néel order for S=1/2 at $J_2 \approx 0.08J_1$, in agreement with a recent variational Monte Carlo study[100]. We find no qualitative change upon using other values of α, or even upon using the conventional criterion $\langle S_{i,\nu}^x\rangle = 0$. The resulting Néel melting curves, at zero and nonzero temperatures, are shown in Fig.6.7 and Fig.6.8.

At zero temperature, it is straightforward to evaluate the expectation values in the melting criterion. For $T \neq 0$ however, we have to take into account a small coupling along the third dimension to allow for a stable magnetically ordered state. For a layered system with very weak interlayer coupling, we can use the two-dimensional Hamiltonian together with an infrared cutoff Λ which is of the order of the interlayer coupling. Spin wave modes with energies greater than Λ appear the same as two-dimensional spin waves. However, modes with energies below Λ can be dropped as their contribution will be suppressed by phase space factors in the three-dimensional problem. In our numerics, we impose this infrared cutoff by simply restricting to a finite system size. Finite size automatically cuts off long wavelength modes with $k < k_c \sim 2\pi/\sqrt{N}$. In our calculations, we restricted our system size to $2 \times 120 \times 120$ spins. This corresponds to $k_c \sim 0.05$, and an infrared cutoff of $\Lambda \sim 0.04JS$.

6.3.3 Field-induced Néel order

As shown in Fig.6.7 and its inset, quantum fluctuations at $B = 0$ lead to melting of Néel order even for $J_2/J_1 < 1/6$, before the classical destruction of Néel order. For nonzero B, the 'melting point' moves toward larger J_2, leading to a window of J_2 over which the quantum disordered liquid can undergo a field-induced phase transition to Néel order.

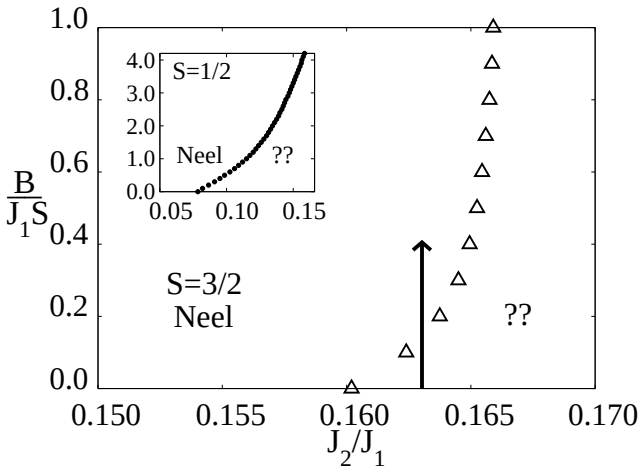

Figure 6.7: $T=0$ melting of Néel order for S=3/2 in the B-J_2 plane (open triangles) obtained using a Lindemann-like criterion, $\sqrt{\langle S_x^2\rangle - \langle S_x\rangle^2} = 5\langle S_x\rangle$. The region "??" is a quantum disordered state - possibly a valence bond solid or a quantum spin liquid. Arrow depicts a field-induced transition to Néel order. (Inset) A similar melting curve for $S=1/2$.

The window of J_2 which allows for a field-induced Néel transition appears to be small for S=3/2. However, small non-zero temperatures widen this window, as shown in Fig.6.8.

Finally, we expect field-induced Néel order even for S=1/2 (see inset to Fig.6.7). The $S = 1/2$ $J_1 - J_2$ model has been extensively studied[100, 36, 34] as an effective model for the honeycomb lattice Hubbard model at intermediate interaction strengths(see Chapter 5 for an overview). Approaching the intermediate-U phase from large values of U, we expect the $J_1 - J_2$ model with relatively small J_2 to be the appropriate effective model. We therefore expect the spin-gapped intermediate phase to also arise from quantum melting of Néel order. Our assertion of field-induced Néel order can be tested by redoing the variational and determinental Monte Carlo calculations of the honeycomb Hubbard model in an applied magnetic field.

Our results are consistent with neutron diffraction experiments[65] on $Bi_3Mn_4O_{12}(NO_3)$ which find field induced Néel order. Our results also explain recent Monte Carlo simula-

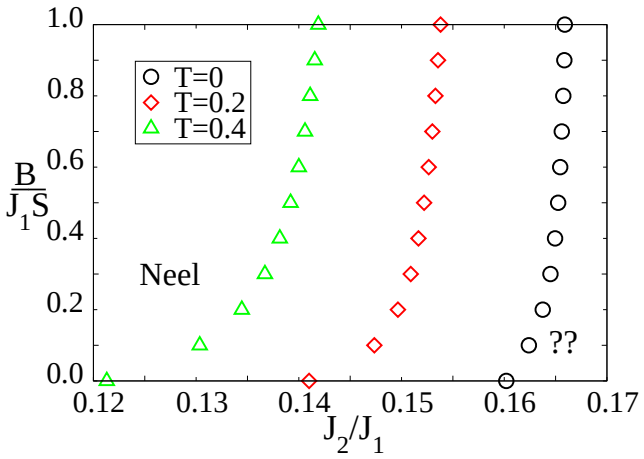

Figure 6.8: Melting of Néel order for $S = 3/2$ in the B-J_2 plane for depicted nonzero temperatures. To the left of the curve, there is stable canted Néel order. To the right, combined effects of quantum and thermal fluctuations melt the in-plane Néel order.

tions of the classical $J_1 - J_2 - B$ model[67]. In these simulations, with $J_2 = 0.175$ and at fixed temperature, increasing the magnetic field leads to Néel-like correlations. In light of our results, this cannot be an indication of long-range Néel order. Instead, increasing the magnetic field simply takes us closer to the Néel phase in the $J_2 - B$ phase diagram shown in Fig. 6.7.

6.4 Summary

Inspired by experiments on the $S = 3/2$ material $Bi_3Mn_4O_{12}(NO_3)$and numerical studies of the honeycomb lattice Hubbard model, we have considered two models of antiferromagnetism on the honeycomb lattice. Both models lead to magnetically disordered ground states which develop Néel order in an applied magnetic field.

In our first model, bilayer coupling leads to an interlayer valence-bond solid state, composed of singlet dimers on every interlayer bond. We use a simplified $J_1 - J_c$ model having only nearest neighbour exchange and bilayer coupling. We use bond-operator theory to study this state and its triplon excitations. When an applied field closes the

spin gap, the lowest lying triplon mode undergoes Bose-condensation, resulting in in-plane Néel order. Chapter 4 describes a variational extension of bond-operator theory, which shows that the bilayer coupling required to stabilize the interlayer valence-bond solid is very large ($J_c/J_1 \gtrsim 9$). Thus, bilayer coupling is highly unlikely to be the source of frustration in BMNO. However, our analysis may prove useful for the study of other bilayer antiferromagnetic systems.

In our second model, we study frustration arising from next-nearest neighbour exchange. We show that quantum fluctuations lead to 'melting' of Néel order. The resulting quantum disordered state develops Néel order in an applied field. Our calculations are relevant to studies on the honeycomb lattice Hubbard model as well. We expect that numerical studies of the spin-gapped phase at intermediate U will also show field-induced Néel order.

Further experiments are needed to understand the physics of $Bi_3Mn_4O_{12}(NO_3)$. So far, only powder samples have been analyzed. The growth of a single crystal sample could greatly improve our understanding. Experiments could try to determine whether triplon-condensation is responsible for the onset of Néel order. With a single crystal sample, neutron scattering could track magnetic excitations across the Néel transition. Careful specific heat measurements (in comparison with a non-magnetic analogue to remove phonon contributions) can determine if the Néel transition is a Bose-condensation transition.

Chapter 7

Future directions

7.1 Superflow instabilities in ultracold atom gases

We have studied the collective mode spectrum of the attractive Hubbard model, which could soon be realized in experiments with ultracold atoms. This system shows competition between superfluidity and Charge Density Wave(CDW) order, which is reflected in the collective mode spectrum. We study imposed superfluid flow as a tool to drive this competition. We classify the various mechanisms through which superflow breakdown may occur and draw stability phase diagrams.

Beyond the dynamical commensurate instability, there are indications that a time-dependent state arises. Can a supersolid phase be stabilized? Further work is needed to definitively answer this question. Adding elements such as nearest neighbour repulsion (perhaps using dipolar gases) could help to stabilize the coexistence phase. A similar question could be posed about the Landau instability. While collective mode energies are negative, external couplings or non-linearities are required to transfer momentum into these modes. A careful study of the Landau instability could give us insights into mode-mode coupling terms. In the strong-coupling pseudospin language, the Landau instability will tell us about spin wave interaction terms that were not taken into account

in our analysis.

Our study could be generalized to other lattice systems which may allow for different kinds of CDW order. For instance, the triangular and honeycomb lattices have nested Fermi surfaces at a filling of 3/4 fermions per site[123]. The competition between superfluidity and stripe-like CDW phases is an interesting direction to pursue. There are many proposals to study competing orders in cold atoms using other systems such as Bose-Fermi mixtures[123], dipolar bosons[124], polar molecules[125], etc. Experiments on ultracold gases may help us develop a deep understanding of competition and interplay between phases.

7.2 Low dimensional magnetism

In Chapter 4, we have discussed spin-S bilayer antiferromagnets with square and honeycomb lattice geometries. Using bond operator theory, we have studied the dimer-Néel transition which is driven by triplon condensation. Standard bond operator theory suffers from a systematic error as S increases. We bridge this deviation by using a variational procedure to take leading corrections into account.

A natural extension of our study would be to map out the complete phase diagram as a function of applied field and interlayer coupling strength. With increasing field, triplet bands with higher energy will sequentially condense followed by higher spin objects such as (spin-2) quintets. In the semi-classical ($S \gg 1$) picture, increasing the applied field smoothly increases the out-of-plane canting of spins all the way upto full polarization. For finite-S, there are likely to be discrete intermediate steps in between with interesting magnetic patterns(e.g., see Ref. [126]). Experimentally, quintet condensation has been observed in Ba_3MnO_8, a bilayer material with a somewhat complicated geometry[127].

Another direction to explore is the effect of magnetic frustration. As the square and honeycomb bilayers are bipartite, the triplon dispersion in the interlayer dimer phase has

a unique minimum at the wavevector corresponding to Néel order. As interlayer coupling is decreased (or when a magnetic field is applied), this triplon mode condenses leading to a dimer-Néel transition. In the limit of decoupled layers (or for large magnetic fields), the in-plane exchange terms are maximally satisfied in a Néel ground state. In non-bipartite frustrated lattices however, simple Néel ordering is not favoured. In the limit of decoupled layers, in the classical ($S = \infty$) model, the ground state has macroscopic degeneracy. As a consequence, we expect the triplon dispersion in the dimer phase to have multiple minima reflecting the ground state degeneracy - we have explicitly checked this for the case of the honeycomb lattice $J_1 - J_2 - J_c$ model. Decreasing the interlayer coupling (or applying a magnetic field) will lower the energy of this 'ring' of triplons. It is possible that correction terms such as triplon-triplon interactions may break this degeneracy to give a dimer-spiral transition. Or, the large number of low-lying triplet excitations could destroy spiral order leading to new ground states and phase transitions. This may be relevant to studies of deconfined quantum criticality. In particular, in the honeycomb lattice spin-1/2 bilayer, a deconfined quantum phase transition[128] has been proposed between an interlayer dimer state and a Nematic Valence Bond Solid (bilayer version of the NVBS state discussed in Chapter 5).

Inspired by the physics of $Bi_3Mn_4O_{12}(NO_3)$(BMNO) and the intermediate-U phase of the honeycomb lattice Hubbard model, we studied the honeycomb lattice J_1-J_2 model in Chapter 5. This model leads to 'lattice nematic' states in various limits. In the context of BMNO, the J_1-J_2 model can explain the absence of long-range order within a quantum melting picture. This description also accounts for the observed field-induced Néel order. However, the precise nature of the disordered state is not known. An analysis of spin-3/2 spin liquid states may resolve this issue. Disorder may also play a significant role in the physics of BMNO as neutron diffraction sees some evidence of glassy behaviour[65]. The role of disorder in melting Néel order could be investigated in the future.

In the honeycomb lattice Hubbard model, the nature of the intermediate spin-gapped

phase has not been conclusively established. There are two candidate ground states - sublattice-pairing spin liquid and plaquette RVB. An unbiased variational approach could be used to resolve the ground state. Determinental Quantum Monte Carlo could also be used to look for a thermal phase transition associated with translational symmetry breaking, which should occur in the plaquette RVB state.

The physics of the J_1-J_2 model at large frustration also holds interesting possibilities. In the regime $J_2/J_1 > 1/6$, the spin wave spectrum has macroscopically degenerate minima leading to a 'Bose surface'. When corrections arising from spin-wave interactions are taken into account, this Bose surface may not survive. However, a very similar model (the honeycomb lattice $J_1 - J_2$ XY model) has been shown to support a robust Bose surface[113]. In our $J_1 - J_2$ Heisenberg model, a renormalization group analysis can be used to reveal if the Bose surface is stable. A resulting 'Bose metal' phase will have interesting properties.

In the future, we hope that there will be many more material realizations of models of low dimensional magnetism which can be used to synthesize, characterize and understand novel quantum phases. The study of competing orders in such magnetic systems will help to develop a more complete understanding of quantum phases and phase transitions. We hope that lessons learnt from the study of magnetism will contribute to a fuller understanding of condensed matter physics.

Appendix A

Appendices to Chapter 2

A.1 Bare Susceptibility

To evaluate the matrix elements in Eq. 2.17, it is convenient to resolve each perturbation operator into two parts – one that creates two QPs and one that annihilates two QPs – as follows:

$\hat{\rho}^{c}_{-\mathbf{K}} = \frac{1}{2}\sum_{\mathbf{k}}(u_{\mathbf{k}+\mathbf{K}}v_{\mathbf{k}} + u_{\mathbf{k}}v_{\mathbf{k}+\mathbf{K}})\gamma^{\dagger}_{\mathbf{k}+\mathbf{K}\uparrow}\gamma^{\dagger}_{-\mathbf{k}\downarrow}$	$\hat{\rho}^{a}_{-\mathbf{K}} = \frac{1}{2}\sum_{\mathbf{k}}(u_{\mathbf{k}-\mathbf{K}}v_{\mathbf{k}} + u_{\mathbf{k}}v_{\mathbf{k}-\mathbf{K}})\gamma_{-\mathbf{k}\downarrow}\gamma_{\mathbf{k}-\mathbf{K}\uparrow}$
$\hat{\Delta}^{c}_{-\mathbf{K}} = -\sum_{\mathbf{k}} v_{\mathbf{k}}v_{\mathbf{k}+\mathbf{K}}\gamma^{\dagger}_{\mathbf{k}+\mathbf{K}\uparrow}\gamma^{\dagger}_{-\mathbf{k}\downarrow}$	$\hat{\Delta}^{a}_{-\mathbf{K}} = \sum_{\mathbf{k}} u_{\mathbf{k}}u_{\mathbf{k}-\mathbf{K}}\gamma_{-\mathbf{k}\downarrow}\gamma_{\mathbf{k}-\mathbf{K}\uparrow}$
$\hat{\Delta}^{\dagger c}_{\mathbf{K}} = \sum_{\mathbf{k}} u_{\mathbf{k}}u_{\mathbf{k}+\mathbf{K}}\gamma^{\dagger}_{\mathbf{k}+\mathbf{K}\uparrow}\gamma^{\dagger}_{-\mathbf{k}\downarrow}$	$\hat{\Delta}^{\dagger a}_{\mathbf{K}} = -\sum_{\mathbf{k}} v_{\mathbf{k}}v_{\mathbf{k}-\mathbf{K}}\gamma_{-\mathbf{k}\downarrow}\gamma_{\mathbf{k}-\mathbf{K}\uparrow}$

Here the superscript 'c' denotes creation of 2 quasiparticles, and 'a' denotes annihilation.

Since χ^0 is a symmetric matrix, it suffices to use the above to compute the following distinct elements:

$$\begin{aligned}
\chi^0_{1,1} &= \frac{1}{4N}\sum_{\mathbf{k}} \left[\frac{(u_{\mathbf{k}-\mathbf{K}}v_{\mathbf{k}} + v_{\mathbf{k}-\mathbf{K}}u_{\mathbf{k}})^2}{\omega + E_{\mathbf{k}-\mathbf{K}} + E_{-\mathbf{k}}} - \frac{(u_{\mathbf{k}}v_{\mathbf{k}+\mathbf{K}} + v_{\mathbf{k}}u_{\mathbf{k}+\mathbf{K}})^2}{\omega - E_{\mathbf{k}+\mathbf{K}} - E_{-\mathbf{k}}}\right], \\
\chi^0_{1,2} &= \frac{1}{2N}\sum_{\mathbf{k}} \left[\frac{(u_{\mathbf{k}-\mathbf{K}}v_{\mathbf{k}} + v_{\mathbf{k}-\mathbf{K}}u_{\mathbf{k}})u_{\mathbf{k}}u_{\mathbf{k}-\mathbf{K}}}{\omega + E_{\mathbf{k}-\mathbf{K}} + E_{-\mathbf{k}}} + \frac{(u_{\mathbf{k}}v_{\mathbf{k}+\mathbf{K}}+v_{\mathbf{k}}u_{\mathbf{k}+\mathbf{K}})v_{\mathbf{k}}v_{\mathbf{k}+\mathbf{K}}}{\omega - E_{\mathbf{k}+\mathbf{K}} - E_{-\mathbf{k}}}\right], \\
\chi^0_{1,3} &= \frac{1}{2N}\sum_{\mathbf{k}} \left[-\frac{(u_{\mathbf{k}-\mathbf{K}}v_{\mathbf{k}} + v_{\mathbf{k}-\mathbf{K}}u_{\mathbf{k}})v_{\mathbf{k}}v_{\mathbf{k}-\mathbf{K}}}{\omega + E_{\mathbf{k}-\mathbf{K}} + E_{-\mathbf{k}}} - \frac{(u_{\mathbf{k}}v_{\mathbf{k}+\mathbf{K}}+v_{\mathbf{k}}u_{\mathbf{k}+\mathbf{K}})u_{\mathbf{k}}u_{\mathbf{k}+\mathbf{K}}}{\omega - E_{\mathbf{k}+\mathbf{K}} - E_{-\mathbf{k}}}\right], \\
\chi^0_{2,2} &= \frac{1}{N}\sum_{\mathbf{k}} \left[\frac{u^2_{\mathbf{k}}u^2_{\mathbf{k}-\mathbf{K}}}{\omega + E_{\mathbf{k}-\mathbf{K}} + E_{-\mathbf{k}}} - \frac{v^2_{\mathbf{k}}v^2_{\mathbf{k}+\mathbf{K}}}{\omega - E_{\mathbf{k}+\mathbf{K}} - E_{-\mathbf{k}}}\right], \\
\chi^0_{2,3} &= \frac{1}{N}\sum_{\mathbf{k}} \left[-\frac{u_{\mathbf{k}}v_{\mathbf{k}}u_{\mathbf{k}-\mathbf{K}}v_{\mathbf{k}-\mathbf{K}}}{\omega + E_{\mathbf{k}-\mathbf{K}} + E_{-\mathbf{k}}} + \frac{u_{\mathbf{k}}v_{\mathbf{k}}u_{\mathbf{k}+\mathbf{K}}v_{\mathbf{k}+\mathbf{K}}}{\omega - E_{\mathbf{k}+\mathbf{K}} - E_{-\mathbf{k}}}\right], \\
\chi^0_{3,3} &= \frac{1}{N}\sum_{\mathbf{k}} \left[\frac{v^2_{\mathbf{k}}v^2_{\mathbf{k}-\mathbf{K}}}{\omega + E_{\mathbf{k}-\mathbf{K}} + E_{-\mathbf{k}}} - \frac{u^2_{\mathbf{k}}u^2_{\mathbf{k}+\mathbf{K}}}{\omega - E_{\mathbf{k}+\mathbf{K}} - E_{-\mathbf{k}}}\right].
\end{aligned} \tag{A.1}$$

A.2 Derivation of strong coupling pseudospin model

We study the strong-coupling limit of the attractive Hubbard Hamiltonian (Eq. 2.1) on a bipartite lattice. In the strong coupling limit, the chemical potential and the Hubbard attraction dominate while the hopping terms act as a small perturbation. The local Hilbert space has four states. The four states and their energies are given by

$\|-\rangle$	$-U/4$
$\|\uparrow\rangle$	$-\mu + U/4$
$\|\downarrow\rangle$	$-\mu + U/4$
$\|\uparrow\downarrow\rangle$	$-2\mu - U/4$

At half-filling, μ is zero as discussed in the Section. 2.1.1. The states $|-\rangle$ and $|\uparrow\downarrow\rangle$ are degenerate while singly occuppied states have much higher energy. Even away from half-filling, we argue that singly occuppied states have much higher energies and may be neglected in a low-energy description. This argument may be phrased as follows. Suppose there are two singly occuppied sites, one with an up spin fermion and another

with a down spin fermion. By rearranging the fermions to have one doubly occuppied site and one empty site, the system can lower its energy by U. Thus, as long as the system is unpolarized (having equal number of up and down fermions, as in our case), its low energy description will only involve sites that are doubly occuppied or empty.

In this low energy subspace, the Hilbert space for two sites is given by (column on the right gives the energy of each state)

$\|-,-\rangle$	$-U/2$
$\|-,\uparrow\downarrow\rangle$	$-2\mu - U/2$
$\|\uparrow\downarrow,-\rangle$	$-2\mu - U/2$
$\|\uparrow\downarrow,\uparrow\downarrow\rangle$	$-4\mu - U/2$

Within this two-site problem, we treat the hopping perturbatively. The states with zero occupancy ($|-,-\rangle$) and those with maximum occupancy ($|\uparrow\downarrow,\uparrow\downarrow\rangle$) are not altered by the hopping Hamiltonian. The other two states are connected in second order perturbation theory. The processes that contribute are

$$|-,\uparrow\downarrow\rangle \xrightarrow{-t} \left\{ \begin{array}{c} |\uparrow,\downarrow\rangle \\ |\downarrow,\uparrow\rangle \end{array} \right\} \xrightarrow{-t} \left\{ \begin{array}{c} |\uparrow\downarrow,-\rangle \\ |-,\uparrow\downarrow\rangle \end{array} \right\}$$

$$|-,\uparrow\downarrow\rangle \xrightarrow{-t} \left\{ \begin{array}{c} |\uparrow,\downarrow\rangle \\ |\downarrow,\uparrow\rangle \end{array} \right\} \xrightarrow{-t} \left\{ \begin{array}{c} |\uparrow\downarrow,-\rangle \\ |-,\uparrow\downarrow\rangle \end{array} \right\}$$

The amplitude of each of these processes is $-2t^2/U$. Incorporating these amplitudes, the Hamiltonian for the two site problem may be written as

$$H = \begin{pmatrix} \langle -,-| \\ \langle -,\uparrow\downarrow| \\ \langle \uparrow\downarrow,-| \\ \langle \uparrow\downarrow,\uparrow\downarrow| \end{pmatrix}^T \begin{pmatrix} -U/2 & 0 & 0 & 0 \\ 0 & -2\mu - U/2 - 2t^2/U & -2t^2/U & 0 \\ 0 & -2t^2/U & -2\mu - U/2 - 2t^2/U & 0 \\ 0 & 0 & 0 & -4\mu - U/2 \end{pmatrix} \begin{pmatrix} |-,-\rangle \\ |-,\uparrow\downarrow\rangle \\ |\uparrow\downarrow,-\rangle \\ |\uparrow\downarrow,\uparrow\downarrow\rangle \end{pmatrix}.$$

This low energy Hamiltonian may be mapped onto a spin-1/2 local moment system. On each site, the state with double occupancy is mapped onto an 'up' pseudospin and the

state with zero occupancy is mapped onto a 'down' pseudospin.

$$|-\rangle_{fermion} \rightarrow |\downarrow\rangle_{spin}; \qquad |\uparrow\downarrow\rangle_{fermion} \rightarrow |\uparrow\rangle_{spin}.$$

Our Hamiltonian maps onto a pseudospin-exchange Hamiltonian given by

$$H_{sp} = J\sum_{\langle ij\rangle} S_i^z S_j^z - \frac{J}{2}\sum_{\langle ij\rangle}\left[S_i^+ S_j^- + S_i^- S_j^+\right] - B\sum_i S_i^z, \tag{A.2}$$

with $J = 4t^2/U$ and $B = \mu$ (we have ignored a constant energy shift of $-2\mu - U/2 - t^2/U$).

This spin model has positive couplings along the spin-z direction, and negative couplings along the spin-x and spin-y directions. We transform this Hamiltonian into the symmetric Heisenberg model, by using the bipartite nature of the lattice as follows.

We divide the lattice into A and B sublattices.

$$H_{sp} = J\sum_{i\in A, j(i)\in B} S_{i,A}^z S_{j,B}^z - J\sum_{i\in A, j(i)\in B}\left[S_{i,A}^x S_{j,B}^x + S_{i,A}^y S_{j,B}^y\right] - B\sum_i\left[S_{i,A}^z + S_{i,B}^z\right], \tag{A.3}$$

where $j(i)$ indicates the nearest neighbours of site i. The nearest neighbours of site i of the A sublattice all lie on the B sublattice. We perform a SU(2) pseudospin rotation on one of the sublattices:

$$S_{i,B}^x \rightarrow -T_{i,B}^x; \quad S_{i,B}^y \rightarrow -T_{i,B}^y; \quad S_{i,B}^z \rightarrow T_{i,B}^z. \tag{A.4}$$

The transformed $\mathbf{T}$ operators, in terms of the original fermions, are identical to the Anderson pseudospin operators defined in Eq. 2.4. In terms of these operators, the Hamiltonian reduces to the Heisenberg model:

$$H_{pseudospin} = J\sum_{i\in A, j(i)\in B} \mathbf{T}_{i,A}\cdot\mathbf{T}_{j,B} - B\sum_i\left[T_{i,A}^z + T_{i,B}^z\right]. \tag{A.5}$$

The z-component of the spins corresponds to density and the magnetic field B is the chemical potential, μ. The x and y components correspond to superfluid order. all done with

Appendix B

Appendices to Chapter 3

B.1 Landau criterion

Landau first estimated the maximum superflow that a superfluid can sustain[129]. Let us consider a many particle system described by a generic Hamiltonian of the form

$$\hat{H}_0 = \sum_i \frac{\hat{\mathbf{p}}_i^2}{2m_i} + \sum_{\langle ij \rangle} \hat{V}(|\hat{\mathbf{r}}_i - \hat{\mathbf{r}}_j|). \tag{B.1}$$

We take the ground state of this system to be a superfluid, denoted by $|\psi_{GS}\rangle$. The eigenstates which embody the excitations about the superfluid ground state, have well-defined momentum. We label an excited state as $|\psi_{\mathbf{p}}\rangle$ with momentum $\mathbf{p}$ and energy $\omega_{\mathbf{p}}$, given by

$$\begin{aligned} \omega_{\mathbf{p}} &= \langle\psi_{\mathbf{p}}|\hat{H}_0|\psi_{\mathbf{p}}\rangle - \langle\psi_{GS}|\hat{H}_0|\psi_{GS}\rangle, \\ \mathbf{p} &= \langle\psi_{\mathbf{p}}|\sum_i \hat{\mathbf{p}}_i|\psi_{\mathbf{p}}\rangle. \end{aligned} \tag{B.2}$$

If there is no position-dependent constraining potential, this system possesses Galilean invariance, i.e., the eigenstates of this Hamiltonian are unchanged under a Galilean boost given by

$$\mathbf{r}_i \to \mathbf{r}_i - \mathbf{v}t; \qquad \mathbf{p}_i \to \mathbf{p}_i - m_i\mathbf{v}. \tag{B.3}$$

This is equivalent to switching to a frame that is moving with a velocity $\mathbf{v}$. With this boost, the Hamiltonian transforms as

$$\hat{H}_{flow} = \hat{H}_0 + \frac{1}{2}\Big(\sum_i m_i\Big)\mathbf{v}^2 - \mathbf{v}\cdot\{\sum_i \hat{\mathbf{p}}_i\}. \tag{B.4}$$

As seen from this expression, the eigenstates of $\hat{H}_0$ are also eigenstates of $\hat{H}_{flow}$, however the eigenenergies may be different. In the moving frame, the excited state $|\psi_{\mathbf{p}}\rangle$ has the energy

$$\begin{aligned}\omega_{\mathbf{p}}^{flow} &= \langle\psi_{\mathbf{p}}|\hat{H}_{flow}|\psi_{\mathbf{p}}\rangle - \langle\psi_{GS}|\hat{H}_{flow}|\psi_{GS}\rangle \\ &= \omega_{\mathbf{p}} - \mathbf{p}\cdot\mathbf{v}.\end{aligned} \tag{B.5}$$

In the last step above, we have used Eqs.B.4 and B.2.

Now, let us say the superfluid is forced to flow with a velocity $\mathbf{v}$ against a fixed obstacle. We work in the lab frame in which the superfluid is flowing and the obstacle is at rest. In this frame, the excitation spectrum of the superfluid is given by Eq.B.5. Due to the superfluid nature of the system, the flow will be dissipationless (for small flow velocities) with no momentum transferred to the obstacle. The underlying reason is that the superfluid does not have any gapless excitations at non-zero wavevectors. Thus, it is not possible to transfer momentum to the stationary obstacle while conserving energy. The critical superflow velocity can be determined from this reasoning - the maximum superflow velocity occurs when the excitations become gapless at non-zero wavevectors, i.e., when $\omega_{\mathbf{p}'\neq 0}^{flow} = 0$. When this condition is met, these excitations with momentum $\mathbf{p}'$ can be populated while transferring momentum to the obstacle. The obstacle will start moving with the superfluid, and superfluidity will be lost. This gives the Landau critical velocity

$$v_{crit} = \min_{\mathbf{q}\neq 0}\Big[\frac{\omega_{\mathbf{q}}}{q_{\|}}\Big], \tag{B.6}$$

where $q_{\|}$ is the component of momentum along the direction of flow.

B.2 Bare Susceptibility in the flowing superfluid

To evaluate the matrix elements of the bare susceptibility matrix (in Eq. 3.22), we resolve each perturbation operator into two parts – one that creates two QPs and one that annihilates two QPs – as follows:

$\hat{\rho}^c_{-\mathbf{K}} = \frac{1}{2}\sum_{\mathbf{k}}(u_{\mathbf{k}+\mathbf{K}}v_{\mathbf{k}} + u_{\mathbf{k}}v_{\mathbf{k}+\mathbf{K}})\gamma^\dagger_{\mathbf{k}+\mathbf{K}\uparrow}\gamma^\dagger_{-\mathbf{k}+\mathbf{Q}\downarrow}$	$\hat{\rho}^a_{-\mathbf{K}} = \frac{1}{2}\sum_{\mathbf{k}}(u_{\mathbf{k}-\mathbf{K}}v_{\mathbf{k}} + u_{\mathbf{k}}v_{\mathbf{k}-\mathbf{K}})\gamma_{-\mathbf{k}+\mathbf{Q}\downarrow}\gamma_{\mathbf{k}-\mathbf{K}\uparrow}$
$\hat{\Delta}^c_{-\mathbf{K}+\mathbf{Q}} = -\sum_{\mathbf{k}} v_{\mathbf{k}}v_{\mathbf{k}+\mathbf{K}}\gamma^\dagger_{\mathbf{k}+\mathbf{K}\uparrow}\gamma^\dagger_{-\mathbf{k}+\mathbf{Q}\downarrow}$	$\hat{\Delta}^a_{-\mathbf{K}+\mathbf{Q}} = \sum_{\mathbf{k}} u_{\mathbf{k}}u_{\mathbf{k}-\mathbf{K}}\gamma_{-\mathbf{k}+\mathbf{Q}\downarrow}\gamma_{\mathbf{k}-\mathbf{K}\uparrow}$
$\hat{\Delta}^{\dagger c}_{\mathbf{K}+\mathbf{Q}} = \sum_{\mathbf{k}} u_{\mathbf{k}}u_{\mathbf{k}+\mathbf{K}}\gamma^\dagger_{\mathbf{k}+\mathbf{K}\uparrow}\gamma^\dagger_{-\mathbf{k}+\mathbf{Q}\downarrow}$	$\hat{\Delta}^{\dagger a}_{\mathbf{K}+\mathbf{Q}} = -\sum_{\mathbf{k}} v_{\mathbf{k}}v_{\mathbf{k}-\mathbf{K}}\gamma_{-\mathbf{k}+\mathbf{Q}\downarrow}\gamma_{\mathbf{k}-\mathbf{K}\uparrow}$

Here the superscript 'c' denotes creation of 2 quasiparticles, and 'a' denotes annihilation.

Since χ^0 is a symmetric matrix, it suffices to use the above to compute the following distinct elements:

$$
\begin{aligned}
\chi^0_{1,1} &= \frac{1}{4N}\sum_{\mathbf{k}} \left[\frac{(u_{\mathbf{k}-\mathbf{K}}v_{\mathbf{k}} + v_{\mathbf{k}-\mathbf{K}}u_{\mathbf{k}})^2}{\omega + E_{\mathbf{k}-\mathbf{K}} + E_{-\mathbf{k}+\mathbf{Q}}} - \frac{(u_{\mathbf{k}}v_{\mathbf{k}+\mathbf{K}} + v_{\mathbf{k}}u_{\mathbf{k}+\mathbf{K}})^2}{\omega - E_{\mathbf{k}+\mathbf{K}} - E_{-\mathbf{k}+\mathbf{Q}}}\right], \\
\chi^0_{1,2} &= \frac{1}{2N}\sum_{\mathbf{k}} \left[\frac{(u_{\mathbf{k}-\mathbf{K}}v_{\mathbf{k}} + v_{\mathbf{k}-\mathbf{K}}u_{\mathbf{k}})u_{\mathbf{k}}u_{\mathbf{k}-\mathbf{K}}}{\omega + E_{\mathbf{k}-\mathbf{K}} + E_{-\mathbf{k}+\mathbf{Q}}} + \frac{(u_{\mathbf{k}}v_{\mathbf{k}+\mathbf{K}} + v_{\mathbf{k}}u_{\mathbf{k}+\mathbf{K}})v_{\mathbf{k}}v_{\mathbf{k}+\mathbf{K}}}{\omega - E_{\mathbf{k}+\mathbf{K}} - E_{-\mathbf{k}+\mathbf{Q}}}\right], \\
\chi^0_{1,3} &= \frac{1}{2N}\sum_{\mathbf{k}} \left[-\frac{(u_{\mathbf{k}-\mathbf{K}}v_{\mathbf{k}} + v_{\mathbf{k}-\mathbf{K}}u_{\mathbf{k}})v_{\mathbf{k}}v_{\mathbf{k}-\mathbf{K}}}{\omega + E_{\mathbf{k}-\mathbf{K}} + E_{-\mathbf{k}+\mathbf{Q}}} - \frac{(u_{\mathbf{k}}v_{\mathbf{k}+\mathbf{K}} + v_{\mathbf{k}}u_{\mathbf{k}+\mathbf{K}})u_{\mathbf{k}}u_{\mathbf{k}+\mathbf{K}}}{\omega - E_{\mathbf{k}+\mathbf{K}} - E_{-\mathbf{k}+\mathbf{Q}}}\right], \\
\chi^0_{2,2} &= \frac{1}{N}\sum_{\mathbf{k}} \left[\frac{u^2_{\mathbf{k}}u^2_{\mathbf{k}-\mathbf{K}}}{\omega + E_{\mathbf{k}-\mathbf{K}} + E_{-\mathbf{k}+\mathbf{Q}}} - \frac{v^2_{\mathbf{k}}v^2_{\mathbf{k}+\mathbf{K}}}{\omega - E_{\mathbf{k}+\mathbf{K}} - E_{-\mathbf{k}+\mathbf{Q}}}\right], \\
\chi^0_{2,3} &= \frac{1}{N}\sum_{\mathbf{k}} \left[-\frac{u_{\mathbf{k}}v_{\mathbf{k}}u_{\mathbf{k}-\mathbf{K}}v_{\mathbf{k}-\mathbf{K}}}{\omega + E_{\mathbf{k}-\mathbf{K}} + E_{-\mathbf{k}+\mathbf{Q}}} + \frac{u_{\mathbf{k}}v_{\mathbf{k}}u_{\mathbf{k}+\mathbf{K}}v_{\mathbf{k}+\mathbf{K}}}{\omega - E_{\mathbf{k}+\mathbf{K}} - E_{-\mathbf{k}+\mathbf{Q}}}\right], \\
\chi^0_{3,3} &= \frac{1}{N}\sum_{\mathbf{k}} \left[\frac{v^2_{\mathbf{k}}v^2_{\mathbf{k}-\mathbf{K}}}{\omega + E_{\mathbf{k}-\mathbf{K}} + E_{-\mathbf{k}+\mathbf{Q}}} - \frac{u^2_{\mathbf{k}}u^2_{\mathbf{k}+\mathbf{K}}}{\omega - E_{\mathbf{k}+\mathbf{K}} - E_{-\mathbf{k}+\mathbf{Q}}}\right].
\end{aligned}
\tag{B.7}
$$

B.3 Mean-field theory of coexistence phase

Beyond the dynamical commensurate instability, we expect the onset of checkerboard density correlations. This could lead to coexisting superfluidity and density order, a "flowing supersolid". We perform a mean field analysis including both orders in order to examine the existence and stability of this coexistence phase.

We decouple the Hubbard interaction using the following mean field order parameters:

$$\begin{aligned}\Delta &\equiv \frac{U}{N}\sum_{\mathbf{k}}\langle c_{-\mathbf{k}+\mathbf{Q}\downarrow}c_{\mathbf{k}\uparrow}\rangle,\\ \tilde{\rho} &\equiv \frac{U}{2N}\sum_{\mathbf{k}}\langle c^{\dagger}_{\mathbf{k}+\mathbf{\Pi}\sigma}c_{\mathbf{k}\sigma}\rangle,\\ \tilde{\Delta} &\equiv \frac{U}{N}\sum_{\mathbf{k}}\langle c_{-\mathbf{k}+\mathbf{\Pi}+\mathbf{Q}\downarrow}c_{\mathbf{k}\uparrow}\rangle,\end{aligned} \tag{B.8}$$

where $\mathbf{\Pi} \equiv (\pi, \pi)$ in 2D or (π, π, π) in 3D.

Using global phase rotation U(1) symmetry, we choose Δ to be real but we allow $\tilde{\Delta}$ to be complex. $\tilde{\rho}$, being the expectation value of the staggered density, is real.

Upto a constant, the Hamiltonian may be written as:

$$H = {\sum_{\mathbf{k}}}' \Psi^{\dagger}_{\mathbf{k}}\underline{H}(\mathbf{k})\Psi_{\mathbf{k}}, \tag{B.9}$$

where the primed summation in the Hamiltonian indicates that if $\mathbf{k}$ is included, then $\mathbf{k}+\mathbf{\Pi}$ is to be excluded. We have used

$$\Psi_{\mathbf{k}} = \begin{pmatrix} c_{\mathbf{k}\uparrow} \\ c^{\dagger}_{-\mathbf{k}+\mathbf{Q}\downarrow} \\ c_{\mathbf{k}+\mathbf{\Pi}\uparrow} \\ c^{\dagger}_{-\mathbf{k}-\mathbf{\Pi}+Q\downarrow} \end{pmatrix}; \qquad \underline{H} = \begin{pmatrix} \xi_{\mathbf{k}} & -\Delta & -\tilde{\rho} & -\tilde{\Delta} \\ -\Delta & -\xi_{-\mathbf{k}+\mathbf{Q}} & -\tilde{\Delta}^{*} & \tilde{\rho} \\ -\tilde{\rho} & -\tilde{\Delta} & \xi_{\mathbf{k}+\mathbf{\Pi}} & -\Delta \\ -\tilde{\Delta}^{*} & \tilde{\rho} & -\Delta & -\xi_{-\mathbf{k}-\mathbf{\Pi}+\mathbf{Q}} \end{pmatrix}. \tag{B.10}$$

For given U, $\mathbf{Q}$ and density, we numerically diagonalize this matrix and solve the self-consistency equations for Δ, $\tilde{\rho}$, $\tilde{\Delta}$ and the filling f. We also evaluate the uniform current in the converged solution,

$$\langle \hat{\mathcal{J}} \rangle = -2t\langle \sum_{\mathbf{k}} c^{\dagger}_{\mathbf{k}\sigma}c_{\mathbf{k}\sigma}\boldsymbol{\nabla}_{\mathbf{k}}\epsilon_{\mathbf{k}}\rangle \tag{B.11}$$

where $-2t\epsilon_{\mathbf{k}}$ is the non-interacting fermion dispersion.

A "flowing supersolid" phase is indicated by simultaneous non-zero values for Δ and $\tilde{\rho}$. As expected, we do find a "flowing supersolid" phase beyond the dynamical commensurate instability. However, as shown in Fig. B.1, the onset of density order coincides

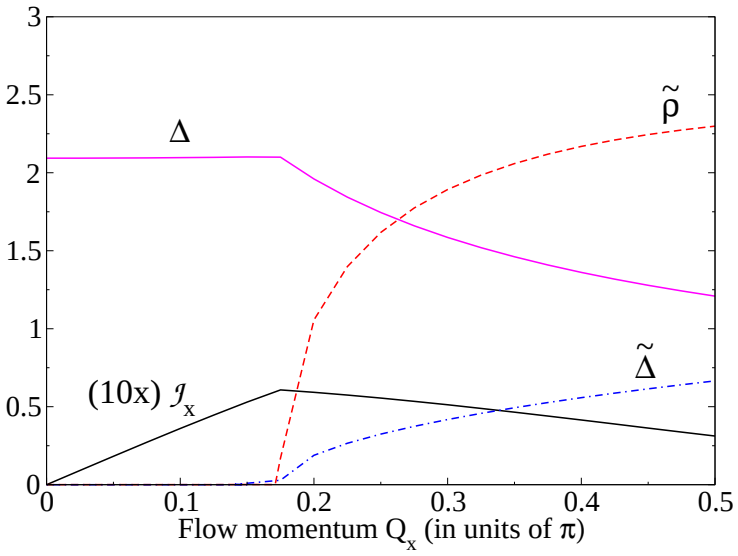

Figure B.1: Mean field theory of the "flowing supersolid" state: mean field order parameters as functions of the flow momentum in 2D for U/t=7 and with a filling of 0.8 fermions per site. Supersolid order onsets around $Q_x \approx 0.2\pi$, as both Δ and $\tilde{\rho}$ have simultaneous non-zero expectation values. This coincides with a maximum in the current as a function of the flow momentum, indicating a dynamical instability.

with a maximum in current as a function of flow momentum. This indicates that the system is dynamically unstable to long wavelength phase and density fluctuations, as we argue below.

Let us consider a one-dimensional superfluid system for simplicity. Denoting the mean field density and the phase of the superfluid order parameter by n_0 and ϕ_0 respectively, we consider fluctuations δn and $\delta\phi$. The current is some function of the gradient of the phase:

$$\langle \hat{\mathcal{J}} \rangle = \mathcal{J}\left(\frac{d\phi}{dx}\right). \tag{B.12}$$

The equations governing the dynamics of the fluctuations are the Josephson relation and the continuity equation. The former gives:

$$\frac{d\delta\phi}{dt} = -\alpha\delta n, \tag{B.13}$$

where $\alpha = d\mu/dn$ is a positive-definite quantity closely related to compressibility. The

continuity equation is:

$$\frac{dn}{dt} = -\frac{d\mathcal{J}}{dx}.$$

Substituting $n = n_0 + \delta n$ and $\frac{d\phi}{dx} = Q + \frac{d\delta\phi}{dx}$, where $Q \equiv \frac{d\phi_0}{dx}$, we obtain

$$\frac{d\delta n}{dt} = -\frac{d\mathcal{J}}{dQ}\frac{d^2\delta\phi}{dx^2}. \tag{B.14}$$

Combining this with the Josephson relation, we finally obtain:

$$\frac{1}{\alpha}\frac{d^2\delta\phi}{dt^2} = \frac{d\mathcal{J}}{dQ}\frac{d^2\delta\phi}{dx^2} \tag{B.15}$$

When $d\mathcal{J}/dQ$, becomes negative, the wavelike solutions of this equation develop complex frequencies. Fluctuations will grow exponentially in time, making the system dynamically unstable when the current goes through a maximum as a function of the flow momentum Q. The unstable nature of the "flowing supersolid" phase has been explored in Ref.[51] in a one-dimensional model. Within a simple real-time simulation, the commensurate dynamical instability seems to lead to a time-dependent and chaotic state.

Appendix C

Appendices to Chapter 4

C.1 Square bilayer: bosonic Bogoliubov transformation

The MFT Hamiltonian of Eq. 4.4 is diagonalized by a pseudounitary matrix,

$$U_{\mathbf{k}} = \begin{pmatrix} \cosh\theta_{\mathbf{k}} & \sinh\theta_{\mathbf{k}} \\ \sinh\theta_{\mathbf{k}} & \cosh\theta_{\mathbf{k}} \end{pmatrix}. \tag{C.1}$$

Imposing $\tanh 2\theta_{\mathbf{k}} = -2\epsilon_{\mathbf{k}}/(A+2\epsilon_{\mathbf{k}})$, we get

$$\psi^{\dagger}_{\mathbf{k},u}\begin{pmatrix} A+2\epsilon_{\mathbf{k}} & 2\epsilon_{\mathbf{k}} \\ 2\epsilon_{\mathbf{k}} & A+2\epsilon_{\mathbf{k}} \end{pmatrix}\psi_{\mathbf{k},u} = \phi^{\dagger}_{\mathbf{k},u}\begin{pmatrix} \lambda_{\mathbf{k}} & 0 \\ 0 & \lambda_{\mathbf{k}} \end{pmatrix}\phi_{\mathbf{k},u}. \tag{C.2}$$

We have defined new quasiparticle operators given by $\psi_{\mathbf{k},u} = U_{\mathbf{k}}\phi_{\mathbf{k},u}$ so that

$$\begin{pmatrix} t_{\mathbf{k},u} \\ t^{\dagger}_{-\mathbf{k},u} \end{pmatrix} = \begin{pmatrix} \cosh\theta_{\mathbf{k}} & \sinh\theta_{\mathbf{k}} \\ \sinh\theta_{\mathbf{k}} & \cosh\theta_{\mathbf{k}} \end{pmatrix}\begin{pmatrix} \tau_{\mathbf{k},u} \\ \tau^{\dagger}_{-\mathbf{k},u} \end{pmatrix}. \tag{C.3}$$

The τ operators are the triplon quasiparticles. The bilinears defined in Eq. 4.20, may be evaluated using the elements of U as follows:

$$\rho = \frac{1}{4N_\perp}\sum_{\mathbf{k},\delta}\left[\langle t^\dagger_{\mathbf{k},v} t_{\mathbf{k},v}\rangle e^{i\mathbf{k}.\delta}\right] = \frac{1}{4N_\perp}{\sum_{\mathbf{k}}}'(2\cos k_x + 2\cos k_y)\frac{A+2\epsilon_{\mathbf{k}}}{\lambda_{\mathbf{k}}}, \quad \text{(C.4)}$$

$$\Delta = \frac{1}{4N_\perp}\sum_{\mathbf{k},\delta}\left[\langle t^\dagger_{\mathbf{k},v} t^\dagger_{-\mathbf{k},v}\rangle e^{i\mathbf{k}.\delta}\right] = \frac{1}{4N_\perp}{\sum_{\mathbf{k}}}'(2\cos k_x + 2\cos k_y)\frac{(-2\epsilon_{\mathbf{k}})}{\lambda_{\mathbf{k}}}. \quad \text{(C.5)}$$

C.2 Square Bilayer: inclusion of quintets

The spin operators with the inclusion of quintets are given in Eq. 21 of Ref. [89]. Using this reference, we now give explicit expressions for $\hat{E}_{ttq}(S^2)$. In the main text, we defined $\hat{E}_{ttq}(S^2)$ in terms of triplet bilinears $\hat{T}^{[n]}_{i,i+\delta}$. Here, we give expressions for $\hat{T}^{[n]}_{i,i+\delta}$ in momentum space. We use the Fourier transform convention

$$t_{i,u\in\{x,y,z\}} = \frac{1}{\sqrt{N_\perp}}\sum_{\mathbf{k}} t_{\mathbf{k},u} e^{i\mathbf{k}.\mathbf{r}_i}. \quad \text{(C.6)}$$

The operator $\hat{T}^{[n]}_{i,i+\delta}$ is composed of bilinears of the form $t_{i,u}(t_{i+\delta,v} \pm t^\dagger_{i+\delta,v})$. Using the Fourier transform, this generic bilinear may be written as $(1/N_\perp)\sum_{\mathbf{k},\mathbf{p}} t_{-\mathbf{k}+\mathbf{p},u}(t_{\mathbf{k},u} \pm t^\dagger_{-\mathbf{k},u})e^{i\mathbf{k}.\delta}e^{i\mathbf{p}.\mathbf{r}_i}$.

Thus, we may write

$$\sum_\delta \hat{T}^{[n]}_{i,i+\delta} = \frac{M}{N_\perp}\sum_{\mathbf{k},\mathbf{p}} \hat{T}^{[n]}_{-\mathbf{k}+\mathbf{p},\mathbf{k}} e^{i\mathbf{p}.\mathbf{r}_i}\eta_{\mathbf{k}}, \quad \text{(C.7)}$$

where $\eta_{\mathbf{k}} = \sum_\delta e^{i\mathbf{k}\cdot\delta} = 2(\cos k_x + \cos k_y)$ and the coefficient $M = \sqrt{\frac{S(S+1)(2S-1)(2S+3)}{30}}$.

The explicit forms of $\hat{T}^{[n]}_{-\mathbf{k}+\mathbf{p},\mathbf{k}}$ are:

$$\begin{aligned}
\hat{T}^{[-2]}_{-\mathbf{k}+\mathbf{p},\mathbf{k}} &= \tilde{t}_{-\mathbf{k}+\mathbf{p},x}(t_{\mathbf{k},x}+t^{\dagger}_{-\mathbf{k},x}) - \tilde{t}_{-\mathbf{k}+\mathbf{p},y}(t_{\mathbf{k},y}+t^{\dagger}_{-\mathbf{k},y}) \\
&+ i\tilde{t}_{-\mathbf{k}+\mathbf{p},x}(t_{\mathbf{k},y}+t^{\dagger}_{-\mathbf{k},y}) + i\tilde{t}_{-\mathbf{k}+\mathbf{p},y}(t_{\mathbf{k},x}+t^{\dagger}_{-\mathbf{k},x}) \\
\hat{T}^{[-1]}_{-\mathbf{k}+\mathbf{p},\mathbf{k}} &= \tilde{t}_{-\mathbf{k}+\mathbf{p},z}(t_{\mathbf{k},x}+t^{\dagger}_{-\mathbf{k},x}) + \tilde{t}_{-\mathbf{k}+\mathbf{p},x}(t_{\mathbf{k},z}+t^{\dagger}_{-\mathbf{k},z}) \\
&+ i\tilde{t}_{-\mathbf{k}+\mathbf{p},z}(t_{\mathbf{k},y}+t^{\dagger}_{-\mathbf{k},y}) + i\tilde{t}_{-\mathbf{k}+\mathbf{p},y}(t_{\mathbf{k},z}+t^{\dagger}_{-\mathbf{k},z}) \\
\hat{T}^{[0]}_{-\mathbf{k}+\mathbf{p},\mathbf{k}} &= \sqrt{\frac{2}{3}}\Big[-\tilde{t}_{-\mathbf{k}+\mathbf{p},x}(t_{\mathbf{k},x}+t^{\dagger}_{-\mathbf{k},x}) \\
&- \tilde{t}_{-\mathbf{k}+\mathbf{p},y}(t_{\mathbf{k},y}+t^{\dagger}_{-\mathbf{k},y}) + 2\tilde{t}_{-\mathbf{k}+\mathbf{p},z}(t_{\mathbf{k},z}+t^{\dagger}_{-\mathbf{k},z})\Big] \\
\hat{T}^{[-1]}_{-\mathbf{k}+\mathbf{p},\mathbf{k}} &= -\tilde{t}_{-\mathbf{k}+\mathbf{p},z}(t_{\mathbf{k},x}+t^{\dagger}_{-\mathbf{k},x}) - \tilde{t}_{-\mathbf{k}+\mathbf{p},x}(t_{\mathbf{k},z}+t^{\dagger}_{-\mathbf{k},z}) \\
&+ i\tilde{t}_{-\mathbf{k}+\mathbf{p},z}(t_{\mathbf{k},y}+t^{\dagger}_{-\mathbf{k},y}) + i\tilde{t}_{-\mathbf{k}+\mathbf{p},y}(t_{\mathbf{k},z}+t^{\dagger}_{-\mathbf{k},z}) \\
\hat{T}^{[2]}_{-\mathbf{k}+\mathbf{p},\mathbf{k}} &= \tilde{t}_{-\mathbf{k}+\mathbf{p},x}(t_{\mathbf{k},x}+t^{\dagger}_{-\mathbf{k},x}) - \tilde{t}_{-\mathbf{k}+\mathbf{p},y}(t_{\mathbf{k},y}+t^{\dagger}_{-\mathbf{k},y}) \\
&-i\ \tilde{t}_{-\mathbf{k}+\mathbf{p},x}(t_{\mathbf{k},y}+t^{\dagger}_{-\mathbf{k},y}) - i\tilde{t}_{-\mathbf{k}+\mathbf{p},y}(t_{\mathbf{k},x}+t^{\dagger}_{-\mathbf{k},x})
\end{aligned} \tag{C.8}$$

We have denoted some triplet operators as t and some as $\tilde{t}$. For the purposes of the square lattice, this distinction can be ignored. We will use these same expressions in the context of the honeycomb lattice also. For the honeycomb case, t and $\tilde{t}$ operators will act on different sublattices.

The energy correction due to coupling to quintets is given in Eq. 4.32. Using the Fourier transformed expression in Eq. C.7, we rewrite the energy as

$$\Delta E^{S>1/2}_{\square} = \frac{M^2\bar{s}^2}{N_{\perp}} \sum_{m=-2,\cdots,2} \sum_{\mathbf{p}} E^{[m]}_{\mathbf{p}} \tag{C.9}$$

where $\mathbf{p}$ is the momentum of the intermediate state. The quantity $E^{[m]}_{\mathbf{p}}$ is given by

$$E^{[m]}_{\mathbf{p}} = \sum_{\nu\neq 0} \frac{|\langle\nu| \sum_{\mathbf{k}} \hat{T}^{[n]}_{-\mathbf{k}+\mathbf{p},\mathbf{k}}\eta_{\mathbf{k}}|0\rangle|^2}{E_0 - E_\nu}. \tag{C.10}$$

Here, $(-\mathbf{p})$ is the momentum of the intermediate state $|\nu\rangle$. As described in the Section 4.7.1, the intermediate states $|\nu\rangle$ that contribute have two triplon quasiparticle excitations and one quintet excitation. An intermediate state with momentum $(-\mathbf{p})$ may be

represented as

$$|\nu_{2-triplon}\rangle = \tau^{\dagger}_{\mathbf{q}-\mathbf{p},u'}\tau^{\dagger}_{-\mathbf{q},v'}|0\rangle. \tag{C.11}$$

With this parametrization, the sum over intermediate states $|\nu\rangle$ may be written as

$$\sum_{\nu\neq 0} \longrightarrow \sum_{\mathbf{q}} \sum_{u',v'\in\{x,y,z\}} . \tag{C.12}$$

Evaluating the matrix elements using this parametrization of the intermediate state, we find that the energy contribution $E^{[m]}_{\mathbf{p}}$ is the same from every m-sector, i.e., $E^{[m]}_{\mathbf{p}} = E_{\mathbf{p}}$ for all m. The quantity $E_{\mathbf{p}}$ is given by

$$\begin{aligned} E_{\mathbf{p}} = -2\sum_{\mathbf{q}} \quad & \Big[\sinh^2(\theta_{\mathbf{q}})\eta^2_{\mathbf{p}-\mathbf{q}}\{\cosh(2\theta_{\mathbf{p}-\mathbf{q}}) + \sinh(2\theta_{\mathbf{p}-\mathbf{q}}\} \\ + \quad & \sinh^2(\theta_{\mathbf{p}-\mathbf{q}})\eta^2_{\mathbf{q}}\{\cosh(2\theta_{\mathbf{q}}) + \sinh(2\theta_{\mathbf{q}})\}\Big]/\{\varepsilon_q - \mu + \lambda_{-\mathbf{q}} + \lambda_{-\mathbf{p}+\mathbf{q}}\}. \end{aligned} \tag{C.13}$$

C.3 Honeycomb bilayer: bosonic Bogoliubov transformation

The mean field Hamiltonian of Eq. 4.12 may be diagonalized by the matrix,

$$P_{\mathbf{k}} = \frac{1}{\sqrt{2}}\begin{pmatrix} 1 & 1 & 0 & 0 \\ -b_{\mathbf{k}} & b_{\mathbf{k}} & 0 & 0 \\ 0 & 0 & 1 & 1 \\ 0 & 0 & -b_{\mathbf{k}} & b_{\mathbf{k}} \end{pmatrix}\begin{pmatrix} C_{\mathbf{k},1} & 0 & S_{\mathbf{k},1} & 0 \\ 0 & C_{\mathbf{k},2} & 0 & S_{\mathbf{k},2} \\ S_{\mathbf{k},1} & 0 & C_{\mathbf{k},1} & 0 \\ 0 & S_{\mathbf{k},2} & 0 & C_{\mathbf{k},2} \end{pmatrix}.$$

Here, we have defined $b_{\mathbf{k}} \equiv \beta^*_{\mathbf{k}}/|\beta_{\mathbf{k}}|$. We take the other entries to be hyperbolic functions given by $C_{\mathbf{k},n} = \cosh\kappa_{\mathbf{k},n}$ and $S_{\mathbf{k},n} = \sinh\kappa_{\mathbf{k},n}$, with $n = 1, 2$. With this definition, this matrix $P_{\mathbf{k}}$ satisfies the pseudo-unitarity condition $P_{\mathbf{k}}\sigma P^{\dagger}_{\mathbf{k}} = \sigma$, where $\sigma = \mathrm{Diag}\{1, 1, -1, -1\}$. To diagonalize the Hamiltonian matrix $M_{\mathbf{k}}$, we set

$$\begin{aligned} \tanh 2\kappa_{\mathbf{k},1} &= \beta_{\mathbf{k}}/(C - \beta_{\mathbf{k}}); \\ \tanh 2\kappa_{\mathbf{k},2} &= -\beta_{\mathbf{k}}/(C + \beta_{\mathbf{k}}). \end{aligned} \tag{C.14}$$

With this choice, the matrix $P_{\mathbf{k}}$ diagonalizes the Hamiltonian,

$$P_{\mathbf{k}}^{\dagger} M_{\mathbf{k}} P_{\mathbf{k}} = \mathrm{Diag}\{\lambda_{\mathbf{k},1}, \lambda_{\mathbf{k},2}, \lambda_{\mathbf{k},1}, \lambda_{\mathbf{k},2}\}. \tag{C.15}$$

where $\lambda_{\mathbf{k},1/2}$ are as defined in the main body. We transform the triplet operators defined in Eq. 4.12 into new quasiparticle operators using

$$\begin{pmatrix} t_{\mathbf{k},A,u} \\ t_{\mathbf{k},B,u} \\ t^{\dagger}_{-\mathbf{k},A,u} \\ t^{\dagger}_{-\mathbf{k},B,u} \end{pmatrix} = P_{\mathbf{k}} \begin{pmatrix} \vartheta_{\mathbf{k},1,u} \\ \vartheta_{\mathbf{k},2,u} \\ \vartheta^{\dagger}_{-\mathbf{k},1,u} \\ \vartheta^{\dagger}_{-\mathbf{k},2,u} \end{pmatrix}. \tag{C.16}$$

The ϑ operators are the triplon quasiparticles. Compared to the square lattice case, the quasiparticle operators have an additional index on account of the sublattice degree of freedom. We can express our original triplet operators as follows:

$$\begin{aligned} t_{\mathbf{k},A,u} &= \sum_{f=1,2} \left(C_{\mathbf{k},f} \vartheta_{\mathbf{k},f,u} + S_{\mathbf{k},f} \vartheta^{\dagger}_{-\mathbf{k},f,u} \right), \\ t_{-\mathbf{k},B,u} &= \sum_{f=1,2} (-1)^f b^{*}_{\mathbf{k}} \left(C_{\mathbf{k},f} \vartheta_{-\mathbf{k},f,u} + S_{\mathbf{k},f} \vartheta^{\dagger}_{\mathbf{k},f,u} \right). \end{aligned} \tag{C.17}$$

The bilinears defined in Eq. 4.23 can be evaluated as

$$\begin{aligned} \rho &= \frac{2}{3N_{\perp}} \sum_{\mathbf{k}} \langle t^{\dagger}_{\mathbf{k},A,v} t_{\mathbf{k},B,v} \rangle \gamma_{\mathbf{k}} = \frac{1}{6N_{\perp}} \sum_{\mathbf{k}} |\gamma_{\mathbf{k}}| \left[-\frac{C - |\beta_{\mathbf{k}}|}{\lambda_{\mathbf{k},1}} + \frac{C + |\beta_{\mathbf{k}}|}{\lambda_{\mathbf{k},2}} \right], \\ \Delta &= \frac{2}{3N_{\perp}} \sum_{\mathbf{k}} \langle t^{\dagger}_{\mathbf{k},A,v} t^{\dagger}_{-\mathbf{k},B,v} \rangle \gamma_{\mathbf{k}} = \frac{-1}{6N_{\perp}} \sum_{\mathbf{k}} |\gamma_{\mathbf{k}}| \left[\frac{|\beta_{\mathbf{k}}|}{\lambda_{\mathbf{k},1}} + \frac{|\beta_{\mathbf{k}}|}{\lambda_{\mathbf{k},2}} \right]. \end{aligned}$$

C.4 Honeycomb bilayer: inclusion of quintets

In the main text, we defined $\hat{E}_{ttq}(S^2)$ in terms of triplet bilinears $\hat{A}^{[n]}_{i,i+\delta}$ and $\hat{B}^{[n]}_{i-\delta,i}$. Here, we give expressions for $\hat{A}^{[n]}_{i,i+\delta}$ and $\hat{B}^{[n]}_{i-\delta,i}$ in momentum space. We use the Fourier transform convention

$$t_{i,\alpha\in\{A,B\},u\in\{x,y,z\}} = \frac{1}{\sqrt{N_{\perp}/2}} \sum_{\mathbf{k}} t_{\alpha,\mathbf{k},u} e^{i\mathbf{k}.\mathbf{r}_i}. \tag{C.18}$$

(i) The terms in $\hat{A}^{[n]}_{i,i+\delta}$ are of the form $t_{i,A,u}(t_{i+\delta,B,v} + t^{\dagger}_{i+\delta,B,v})$. Using our Fourier transform convention, we may write

$$\sum_{\delta} \hat{A}^{[n]}_{i,i+\delta} = \frac{M}{N_{\perp}/2} \sum_{\mathbf{k},\mathbf{p}} \hat{A}^{[n]}_{-\mathbf{k}+\mathbf{p},\mathbf{k}} e^{i\mathbf{p}\cdot\mathbf{r}_i} \gamma_{\mathbf{k}}, \tag{C.19}$$

where $\gamma_{\mathbf{k}} = \sum_{\delta} e^{i\mathbf{k}\cdot\delta} = 1 + e^{-ik_b} + e^{-ik_a - ik_b}$ and the coefficient $M = \sqrt{\frac{S(S+1)(2S-1)(2S+3)}{30}}$ is the same as that defined for the square lattice case. The explicit forms of $\hat{A}^{[n]}_{-\mathbf{k}+\mathbf{p},\mathbf{k}}$ are the same of those of $\hat{T}^{[n]}_{-\mathbf{k}+\mathbf{p},\mathbf{k}}$ given in Eq. C.8 with the following redefinition:

$$\begin{aligned} \tilde{t}_{\mathbf{k},u} &\equiv t_{A,\mathbf{k},u} \\ t_{\mathbf{k},u} &\equiv t_{B,\mathbf{k},u} \end{aligned} \tag{C.20}$$

(ii) The terms in $\hat{B}^{[n]}_{i,i-\delta}$ are of the form $t_{i,B,u}(t_{i-\delta,A,v} \pm t^{\dagger}_{i-\delta,A,v})$. Using our Fourier transform convention, we write

$$\sum_{\delta} \hat{B}^{[n]}_{i,i-\delta} = \frac{M}{N_{\perp}/2} \sum_{\mathbf{k},\mathbf{p}} \hat{B}^{[n]}_{-\mathbf{k}+\mathbf{p},\mathbf{k}} e^{i\mathbf{p}\cdot\mathbf{r}_i} \gamma_{-\mathbf{k}} \tag{C.21}$$

Explicit expressions for $\hat{B}^{[n]}_{-\mathbf{k}+\mathbf{p},\mathbf{k}}$ are the same as those of $\hat{T}^{[n]}_{-\mathbf{k}+\mathbf{p},\mathbf{k}}$ given in Eq. C.8 but with the following redefinition:

$$\begin{aligned} \tilde{t}_{\mathbf{k},u} &\equiv t_{B,\mathbf{k},u} \\ t_{\mathbf{k},u} &\equiv t_{A,\mathbf{k},u} \end{aligned} \tag{C.22}$$

The quintet energy correction of Eq. 4.36 may be rewritten as

$$E^{[quint.]} = \frac{M^2 \bar{s}^2}{N_{\perp}/2} \sum_{\mathbf{p}} \sum_{m} \left[(A^{[m]}_{\mathbf{p}}) + (B^{[m]}_{\mathbf{p}}) \right], \tag{C.23}$$

where

$$\begin{aligned} (A^{[m]}_{\mathbf{p}}) &= \sum_{\nu \neq 0} \frac{|\langle \nu | \sum_{\mathbf{k}} \hat{A}^{[m]}_{-\mathbf{k}+\mathbf{p},\mathbf{k}} \gamma_{\mathbf{k}} | 0 \rangle|^2}{E_0 - E_\nu} \\ (B^{[m]}_{\mathbf{p}}) &= \sum_{\nu \neq 0} \frac{|\langle \nu | \sum_{\mathbf{k}} \hat{B}^{[m]}_{-\mathbf{k}+\mathbf{p},\mathbf{k}} \gamma_{-\mathbf{k}} | 0 \rangle|^2}{E_0 - E_\nu} \end{aligned} \tag{C.24}$$

The only intermediate states $|\nu\rangle$ that contribute to the energy are states with two triplon quasiparticle excitations. A generic intermediate state with momentum $(-\mathbf{p})$ may be characterized as

$$|\nu_{2-triplon}\rangle = \vartheta^{\dagger}_{-\mathbf{q},f,u}\vartheta^{\dagger}_{\mathbf{q}-\mathbf{p},g.v}|0\rangle. \tag{C.25}$$

Using this parametrization of a generic state, the sum over intermediate states in Eq. C.24 becomes

$$\sum_{\nu\neq 0} \longrightarrow \frac{1}{2}\sum_{\mathbf{q}}\sum_{f,g\in\{1,2\}}\sum_{u,v\in\{x,y,z\}}, \tag{C.26}$$

There is a factor of 1/2 to account for double counting as $(\mathbf{q}' = \mathbf{p}-\mathbf{q}, f' = g, g' = f)$ corresponds to the same state as $(\mathbf{q}, f, g)$. Evaluating the necessary overlaps, we find that the contribution from each m is the same $(A^{[m]}_{\mathbf{p}}) = (B^{[m]}_{\mathbf{p}}) = E_{\mathbf{p}}$ for $m = -2, \cdots, 2$. The quantity $E_{\mathbf{p}}$ is given by

$$E_{\mathbf{p}} = -2\sum_{\mathbf{q},f,g}\frac{\left[S_{\mathbf{q},f}(-1)^{g}(S_{-\mathbf{p}+\mathbf{q},g}+C_{\mathbf{p}-\mathbf{q},g})|\gamma_{\mathbf{p}-\mathbf{q}}| + S_{\mathbf{p}-\mathbf{q},g}(-1)^{f}(S_{-\mathbf{q},f}+C_{\mathbf{q},f})|\gamma_{\mathbf{q}}|\right]^{2}}{\varepsilon_{q}-\mu+\lambda_{-\mathbf{q},f}+\lambda_{\mathbf{q}-\mathbf{p},g}} \tag{C.27}$$

By plugging these expressions into Eq.C.23, the correction to ground state energy may be computed.

Bibliography

[1] B. Lake, G. Aeppli, K. N. Clausen, D. F. McMorrow, K. Lefmann, N. E. Hussey, N. Magnkorntong, M. Nohara, H. Takagi, T. E. Mason, and A. Schröder, "Spins in the vortices of a high-temperature superconductor," *Science*, vol. 291, no. 5509, pp. 1759–1762, 2001.

[2] J. E. Hoffman, E. W. Hudson, K. M. Lang, V. Madhavan, H. Eisaki, S. Uchida, and J. C. Davis, "A four unit cell periodic pattern of quasi-particle states surrounding vortex cores in $Bi_2Sr_2CaCu_2O_{8+\delta}$," *Science*, vol. 295, no. 5554, pp. 466–469, 2002.

[3] S. Morrison, A. Kantian, A. J. Daley, H. G. Katzgraber, M. Lewenstein, H. P. Büchler, and P. Zoller, "Physical replicas and the Bose glass in cold atomic gases," *New Journal of Physics*, vol. 10, no. 7, p. 073032, 2008.

[4] A. J. Drew, C. Niedermayer, P. J. Baker, F. L. Pratt, S. J. Blundell, T. Lancaster, R. H. Liu, G. Wu, X. H. Chen, I. Watanabe, V. K. Malik, A. Dubroka, M. Rössle, K. W. Kim, C. Baines, and C. Bernhard, "Coexistence of static magnetism and superconductivity in $SmFeAsO_{1-x}F_x$ as revealed by muon spin rotation," *Nature Materials*, vol. 8, pp. 310–314, Apr. 2009.

[5] P. A. Lee, N. Nagaosa, and X.-G. Wen, "Doping a Mott insulator: Physics of high-temperature superconductivity," *Rev. Mod. Phys.*, vol. 78, pp. 17–85, Jan 2006.

[6] J. Paglione and R. L. Greene, "High-temperature superconductivity in iron-based materials," *Nature Physics*, vol. 6, pp. 645–658, Aug. 2010.

[7] E. Morosan, H. W. Zandbergen, B. S. Dennis, J. W. G. Bos, Y. Onose, T. Klimczuk, A. P. Ramirez, N. P. Ong, and R. J. Cava, "Superconductivity in Cu_xTiSe_2," *Nature Physics*, vol. 2, pp. 544–550, Aug. 2006.

[8] M. P. A. Fisher, P. B. Weichman, G. Grinstein, and D. S. Fisher, "Boson localization and the superfluid-insulator transition," *Phys. Rev. B*, vol. 40, pp. 546–570, Jul 1989.

[9] J. Flouquet, D. Aoki, F. Bourdarot, F. Hardy, E. Hassinger, G. Knebel, T. D. Matsuda, C. Meingast, C. Paulsen, and V. Taufour, "Trends in Heavy Fermion Matter," *Journal of Physics Conference Series*, vol. 273, pp. 012001–+, Jan. 2011.

[10] I. Bloch and M. Greiner, "Exploring quantum matter with ultracold atoms in optical lattices," vol. 52 of *Advances In Atomic, Molecular, and Optical Physics*, pp. 1 – 47, Academic Press, 2005.

[11] P. B. Blakie and C. W. Clark, "Wannier states and BoseHubbard parameters for 2D optical lattices," *Journal of Physics B: Atomic, Molecular and Optical Physics*, vol. 37, no. 7, p. 1391, 2004.

[12] M. Greiner, O. Mandel, T. Esslinger, T. W. Hansch, and I. Bloch, "Quantum phase transition from a superfluid to a Mott insulator in a gas of ultracold atoms," *Nature*, vol. 415, no. 6867, pp. 39–44, 2002.

[13] W. Ketterle and M. W. Zwierlein, "Making, probing and understanding ultracold Fermi gases," *Rivista del Nuovo Cimento*, vol. 31, pp. 247–422, 2008.

[14] R. Grimm, *Proceedings of the International School of Physics E. Fermi, Course CLXIV*. IOS Press, Amsterdam, 2006.

[15] J. K. Chin, D. E. Miller, Y. Liu, C. Stan, W. Setiawan, C. Sanner, K. Xu, and W. Ketterle, "Evidence for superfluidity of ultracold fermions in an optical lattice," *Nature*, vol. 443, pp. 961–964, Oct. 2006.

[16] J.-S. Bernier, C. Kollath, A. Georges, L. De Leo, F. Gerbier, C. Salomon, and M. Köhl, "Cooling fermionic atoms in optical lattices by shaping the confinement," *Phys. Rev. A*, vol. 79, p. 061601, Jun 2009.

[17] T.-L. Ho and Q. Zhou, "Universal Cooling Scheme for Quantum Simulation," *ArXiv e-prints*, Nov. 2009.

[18] J. R. Williams, J. H. Huckans, R. W. Stites, E. L. Hazlett, and K. M. O'Hara, "Preparing a highly degenerate Fermi gas in an optical lattice," *Phys. Rev. A*, vol. 82, p. 011610, Jul 2010.

[19] K. L. Hur and T. M. Rice, "Superconductivity close to the Mott state: From condensed-matter systems to superfluidity in optical lattices," *Annals of Physics*, vol. 324, no. 7, pp. 1452 – 1515, 2009. July 2009 Special Issue.

[20] A. F. Ho, M. A. Cazalilla, and T. Giamarchi, "Quantum simulation of the Hubbard model: The attractive route," *Phys. Rev. A*, vol. 79, p. 033620, Mar 2009.

[21] M. Randeria, *Bose-Einstein Condensation*, pp. 355–392. Cambridge University Press, 1995.

[22] R. B. Diener, R. Sensarma, and M. Randeria, "Quantum fluctuations in the superfluid state of the BCS-BEC crossover," *Phys. Rev. A*, vol. 77, p. 023626, Feb 2008.

[23] P. Ghosh, "BCS-BEC crossover in an optical lattice," *ArXiv e-prints*, July 2011.

[24] P. V. E. McClintock, "Ions and the Landau critical velocity in he II," *Zeitschrift fr Physik B Condensed Matter*, vol. 98, pp. 429–434, 1995. 10.1007/BF01338419.

[25] A. P. Chikkatur, A. Görlitz, D. M. Stamper-Kurn, S. Inouye, S. Gupta, and W. Ketterle, "Suppression and enhancement of impurity scattering in a Bose-Einstein condensate," *Phys. Rev. Lett.*, vol. 85, pp. 483–486, Jul 2000.

[26] D. E. Miller, J. K. Chin, C. A. Stan, Y. Liu, W. Setiawan, C. Sanner, and W. Ketterle, "Critical velocity for superfluid flow across the BEC-BCS crossover," *Phys. Rev. Lett.*, vol. 99, p. 070402, Aug 2007.

[27] B. Wu and Q. Niu, "Landau and dynamical instabilities of the superflow of Bose-Einstein condensates in optical lattices," *Phys. Rev. A*, vol. 64, p. 061603, Nov 2001.

[28] E. Altman, A. Polkovnikov, E. Demler, B. I. Halperin, and M. D. Lukin, "Superfluid-insulator transition in a moving system of interacting bosons," *Phys. Rev. Lett.*, vol. 95, p. 020402, Jul 2005.

[29] J. Mun, P. Medley, G. K. Campbell, L. G. Marcassa, D. E. Pritchard, and W. Ketterle, "Phase diagram for a Bose-Einstein condensate moving in an optical lattice," *Phys. Rev. Lett.*, vol. 99, p. 150604, Oct 2007.

[30] J. Alicea, A. V. Chubukov, and O. A. Starykh, "Quantum stabilization of the 1/3-magnetization plateau in Cs_2CuBr_4," *Phys. Rev. Lett.*, vol. 102, p. 137201, Mar 2009.

[31] N. Shannon, T. Momoi, and P. Sindzingre, "Nematic order in square lattice frustrated ferromagnets," *Phys. Rev. Lett.*, vol. 96, p. 027213, Jan 2006.

[32] M. E. Zhitomirsky, "Octupolar ordering of classical Kagomé antiferromagnets in two and three dimensions," *Phys. Rev. B*, vol. 78, p. 094423, Sep 2008.

[33] P. Chandra, P. Coleman, and A. I. Larkin, "Ising transition in frustrated Heisenberg models," *Phys. Rev. Lett.*, vol. 64, pp. 88–91, Jan 1990.

[34] A. F. Albuquerque, D. Schwandt, B. Hetényi, S. Capponi, M. Mambrini, and A. M. Läuchli, "Phase diagram of a frustrated quantum antiferromagnet on the honeycomb lattice: Magnetic order versus valence-bond crystal formation," *Phys. Rev. B*, vol. 84, p. 024406, Jul 2011.

[35] A. Zheludev, T. Masuda, I. Tsukada, Y. Uchiyama, K. Uchinokura, P. Böni, and S.-H. Lee, "Magnetic excitations in coupled Haldane spin chains near the quantum critical point," *Phys. Rev. B*, vol. 62, pp. 8921–8930, Oct 2000.

[36] H. Mosadeq, F. Shahbazi, and S. A. Jafari, "Plaquette valence bond ordering in a J_1-J_2 Heisenberg antiferromagnet on a honeycomb lattice," *Journal of Physics: Condensed Matter*, vol. 23, no. 22, p. 226006, 2011.

[37] R. Ganesh, D. N. Sheng, Y.-J. Kim, and A. Paramekanti, "Quantum paramagnetic ground states on the honeycomb lattice and field-induced Néel order," *Phys. Rev. B*, vol. 83, p. 144414, Apr 2011.

[38] J. Hubbard, "Electron correlations in narrow energy bands," *Proceedings of the Royal Society of London. Series A, Mathematical and Physical Sciences*, vol. 276, no. 1365, pp. pp. 238–257, 1963.

[39] S. Robaszkiewicz, R. Micnas, and K. A. Chao, "Chemical potential and order parameter of extended Hubbard model with strong intra-atomic attraction," *Phys. Rev. B*, vol. 24, pp. 1579–1582, Aug 1981.

[40] J. E. Hirsch, "Simulations of the three-dimensional Hubbard model: Half-filled band sector," *Phys. Rev. B*, vol. 35, pp. 1851–1859, Feb 1987.

[41] A. Moreo and D. J. Scalapino, "Two-dimensional negative-U Hubbard model," *Phys. Rev. Lett.*, vol. 66, pp. 946–948, Feb 1991.

[42] D. J. Scalapino, S. R. White, and S. Zhang, "Insulator, metal, or superconductor: The criteria," *Phys. Rev. B*, vol. 47, pp. 7995–8007, Apr 1993.

[43] L. Belkhir and M. Randeria, "Crossover from cooper pairs to composite bosons: A generalized RPA analysis of collective excitations," *Phys. Rev. B*, vol. 49, pp. 6829–6840, Mar 1994.

[44] P. W. Anderson, "Random-phase approximation in the theory of superconductivity," *Phys. Rev.*, vol. 112, pp. 1900–1916, Dec 1958.

[45] G. Rickayzen, "Collective excitations in the theory of superconductivity," *Phys. Rev.*, vol. 115, pp. 795–808, Aug 1959.

[46] T. Kostyrko and R. Micnas, "Collective modes of the extended Hubbard model with negative U and arbitrary electron density," *Phys. Rev. B*, vol. 46, pp. 11025–11032, Nov 1992.

[47] S. Zhang, "Pseudospin symmetry and new collective modes of the Hubbard model," *Phys. Rev. Lett.*, vol. 65, pp. 120–122, Jul 1990.

[48] A. Auerbach, *Interacting Electrons and Quantum Magnetism.* Springer-Verlag, 1994.

[49] J. Carlson, "Ground-state and low-lying excitations of the Heisenberg antiferromagnet," *Phys. Rev. B*, vol. 40, pp. 846–849, Jul 1989.

[50] Z. Liu and E. Manousakis, "Variational calculations for the square-lattice quantum antiferromagnet," *Phys. Rev. B*, vol. 40, pp. 11437–11440, Dec 1989.

[51] A. A. Burkov and A. Paramekanti, "Stability of superflow for ultracold fermions in optical lattices," *Phys. Rev. Lett.*, vol. 100, p. 255301, Jun 2008.

[52] Y. Yunomae, D. Yamamoto, I. Danshita, N. Yokoshi, and S. Tsuchiya, "Instability of superfluid Fermi gases induced by a rotonlike density mode in optical lattices," *Phys. Rev. A*, vol. 80, p. 063627, Dec 2009.

[53] Z. Koinov, "Bethe-Salpeter equations for the collective-mode spectrum of a superfluid Fermi gas in a moving optical lattice," *ArXiv e-prints*, Oct. 2010.

[54] G. Veeravalli, E. Kuhnle, P. Dyke, and C. J. Vale, "Bragg spectroscopy of a strongly interacting Fermi gas," *Phys. Rev. Lett.*, vol. 101, p. 250403, Dec 2008.

[55] P. Zou, E. D. Kuhnle, C. J. Vale, and H. Hu, "Quantitative comparison between theoretical predictions and experimental results for Bragg spectroscopy of a strongly interacting Fermi superfluid," *Phys. Rev. A*, vol. 82, p. 061605, Dec 2010.

[56] A. J. Leggett, "Can a solid be 'superfluid'?," *Phys. Rev. Lett.*, vol. 25, pp. 1543–1546, Nov 1970.

[57] E. Kim and M. H. W. Chan, "Probable observation of a supersolid helium phase," *Nature*, vol. 427, no. 6867, pp. 225–227, 2004.

[58] A. M. Zagoskin, *Quantum Theory of Many-Body Systems*. Springer-Verlag, Berlin, 1998.

[59] B. I. Halperin and T. M. Rice, "Possible anomalies at a semimetal-semiconductor transition," *Rev. Mod. Phys.*, vol. 40, pp. 755–766, Oct 1968.

[60] C.-L. Song, Y.-L. Wang, P. Cheng, Y.-P. Jiang, W. Li, T. Zhang, Z. Li, K. He, L. Wang, J.-F. Jia, H.-H. Hung, C. Wu, X. Ma, X. Chen, and Q.-K. Xue, "Direct observation of nodes and twofold symmetry in FeSe superconductor," *Science*, vol. 332, no. 6036, pp. 1410–1413, 2011.

[61] O. Smirnova, M. Azuma, N. Kumada, Y. Kusano, M. Matsuda, Y. Shimakawa, T. Takei, Y. Yonesaki, and N. Kinomura, "Synthesis, crystal structure, and mag-

netic properties of $Bi_3Mn_4O_{12}(NO_3)$ oxynitrate comprising S = 3/2 honeycomb lattice," *Journal of the American Chemical Society*, vol. 131, no. 23, pp. 8313–8317, 2009. PMID: 19507911.

[62] S. Okubo, F. Elmasry, W. Zhang, M. Fujisawa, T. Sakurai, H. Ohta, M. Azuma, O. A. Sumirnova, and N. Kumada, "High-field ESR measurements of S =3/2 honeycomb lattice antiferromagnet $Bi_3Mn_4O_{12}(NO_3$)," *Journal of Physics: Conference Series*, vol. 200, no. 2, p. 022042, 2010.

[63] H. C. Kandpal and J. van den Brink, "Calculation of magnetic exchange couplings in the S=3/2 honeycomb system $(Bi_3Mn_4O_{12})NO_3$ from first principles," *Phys. Rev. B*, vol. 83, p. 140412, Apr 2011.

[64] H. Wadati, K. Kato, Y. Wakisaka, T. Sudayama, D. G. Hawthorn, T. Z. Regier, N. Onishi, M. Azuma, Y. Shimakawa, T. Mizokawa, A. Tanaka, and G. A. Sawatzky, "Magnetic frustration in a Mn honeycomb lattice induced by Mn-O-O-Mn pathways," *ArXiv e-prints*, Jan. 2011.

[65] M. Matsuda, M. Azuma, M. Tokunaga, Y. Shimakawa, and N. Kumada, "Disordered ground state and magnetic field-induced long-range order in an S=3/2 antiferromagnetic honeycomb lattice compound $Bi_3Mn_4O_{12}(NO_3)$," *Phys. Rev. Lett.*, vol. 105, p. 187201, Oct 2010.

[66] A. Mulder, R. Ganesh, L. Capriotti, and A. Paramekanti, "Spiral order by disorder and lattice nematic order in a frustrated Heisenberg antiferromagnet on the honeycomb lattice," *Phys. Rev. B*, vol. 81, p. 214419, Jun 2010.

[67] S. Okumura, H. Kawamura, T. Okubo, and Y. Motome, "Novel spin-liquid states in the frustrated Heisenberg antiferromagnet on the honeycomb lattice," *Journal of the Physical Society of Japan*, vol. 79, no. 11, p. 114705, 2010.

[68] A. Oosawa, M. Ishii, and H. Tanaka, "Field-induced three-dimensional magnetic ordering in the spin-gap system $TlCuCl_3$," *Journal of Physics: Condensed Matter*, vol. 11, no. 1, p. 265, 1999.

[69] T. Nikuni, M. Oshikawa, A. Oosawa, and H. Tanaka, "Bose-Einstein condensation of dilute magnons in $TlCuCl_3$," *Phys. Rev. Lett.*, vol. 84, pp. 5868–5871, Jun 2000.

[70] R. W. Smith and D. A. Keszler, "Synthesis, structure, and properties of the orthoborate $SrCu_2(BO_3)_2$," *Journal of Solid State Chemistry*, vol. 93, no. 2, pp. 430 – 435, 1991.

[71] H. Kageyama, K. Yoshimura, R. Stern, N. V. Mushnikov, K. Onizuka, M. Kato, K. Kosuge, C. P. Slichter, T. Goto, and Y. Ueda, "Exact dimer ground state and quantized magnetization plateaus in the two-dimensional spin system $SrCu_2(BO_3)_2$," *Phys. Rev. Lett.*, vol. 82, pp. 3168–3171, Apr 1999.

[72] H. Kageyama, K. Onizuka, T. Yamauchi, Y. Ueda, S. Hane, H. Mitamura, T. Goto, K. Yoshimura, and K. Kosuge, "Anomalous magnetizations in single crystalline $SrCu_2(BO_3)_2$," *Journal of the Physical Society of Japan*, vol. 68, no. 6, pp. 1821–1823, 1999.

[73] M. Jaime, V. F. Correa, N. Harrison, C. D. Batista, N. Kawashima, Y. Kazuma, G. A. Jorge, R. Stern, I. Heinmaa, S. A. Zvyagin, Y. Sasago, and K. Uchinokura, "Magnetic-field-induced condensation of triplons in han purple pigment $BaCuSi_2O_6$," *Phys. Rev. Lett.*, vol. 93, p. 087203, Aug 2004.

[74] M. B. Stone, C. Broholm, D. H. Reich, O. Tchernyshyov, P. Vorderwisch, and N. Harrison, "Quantum criticality in an organic magnet," *Phys. Rev. Lett.*, vol. 96, p. 257203, Jun 2006.

[75] A. J. Millis and H. Monien, "Spin gaps and spin dynamics in $La_{2-x}Sr_xCuO_4$ and $YBa_2Cu_3O_{7-\delta}$," *Phys. Rev. Lett.*, vol. 70, pp. 2810–2813, May 1993.

[76] A. W. Sandvik and D. J. Scalapino, "Order-disorder transition in a two-layer quantum antiferromagnet," *Phys. Rev. Lett.*, vol. 72, pp. 2777–2780, Apr 1994.

[77] A. V. Chubukov and D. K. Morr, "Phase transition, longitudinal spin fluctuations, and scaling in a two-layer antiferromagnet," *Phys. Rev. B*, vol. 52, pp. 3521–3532, Aug 1995.

[78] T. Dodds, B.-J. Yang, and Y. B. Kim, "Theory of magnetic-field-induced Bose-Einstein condensation of triplons in $Ba_3Cr_2O_8$," *Phys. Rev. B*, vol. 81, p. 054412, Feb 2010.

[79] T. M. Rice, "To condense or not to condense," *Science*, vol. 298, no. 5594, pp. 760–761, 2002.

[80] T. Giamarchi, C. Rüegg, and O. Tchernyshyov, "Bose-Einstein condensation in magnetic insulators," *Nat. Phys.*, vol. 4, p. 198, 2008.

[81] L. Wang, K. S. D. Beach, and A. W. Sandvik, "High-precision finite-size scaling analysis of the quantum-critical point of S=12 Heisenberg antiferromagnetic bilayers," *Phys. Rev. B*, vol. 73, p. 014431, Jan 2006.

[82] K. H. Höglund, A. W. Sandvik, and S. Sachdev, "Impurity induced spin texture in quantum critical 2D antiferromagnets," *Phys. Rev. Lett.*, vol. 98, p. 087203, Feb 2007.

[83] T. Roscilde and S. Haas, "Quantum localization in bilayer Heisenberg antiferromagnets with site dilution," *Phys. Rev. Lett.*, vol. 95, p. 207206, Nov 2005.

[84] Y. Matsushita, M. P. Gelfand, and C. Ishii, "Bond-operator mean field theory for the bilayer Heisenberg model," *Journal of the Physical Society of Japan*, vol. 68, no. 1, pp. 247–252, 1999.

[85] D.-K. Yu, Q. Gu, H.-T. Wang, and J.-L. Shen, "Bond-operator approach to the bilayer Heisenberg antiferromagnet," *Phys. Rev. B*, vol. 59, pp. 111–114, Jan 1999.

[86] A. Collins and C. J. Hamer, "Two-particle bound states and one-particle structure factor in a Heisenberg bilayer system," *Phys. Rev. B*, vol. 78, p. 054419, Aug 2008.

[87] H. Liao and T. Li, "Variational study of the quantum phase transition in bilayer Heisenberg model with bosonic RVB wave function," *ArXiv e-prints*, Feb. 2011.

[88] M. B. Stone, M. D. Lumsden, S. Chang, E. C. Samulon, C. D. Batista, and I. R. Fisher, "Singlet-triplet dispersion reveals additional frustration in the triangular-lattice dimer compound $Ba_3Mn_2O_8$," *Phys. Rev. Lett.*, vol. 100, p. 237201, Jun 2008.

[89] B. Kumar, "Bond operators and triplon analysis for spin-S dimer antiferromagnets," *Phys. Rev. B*, vol. 82, p. 054404, Aug 2010.

[90] R. Ganesh, S. V. Isakov, and A. Paramekanti, "Néel to dimer transition in spin-S antiferromagnets: Comparing bond operator theory with quantum Monte Carlo simulations for bilayer Heisenberg models," *Phys. Rev. B*, vol. 84, p. 214412, Dec 2011.

[91] S. Sachdev and R. N. Bhatt, "Bond-operator representation of quantum spins: Mean-field theory of frustrated quantum Heisenberg antiferromagnets," *Phys. Rev. B*, vol. 41, pp. 9323–9329, May 1990.

[92] A. V. Chubukov, "Spontaneous dimerization in quantum-spin chains," *Phys. Rev. B*, vol. 43, pp. 3337–3344, Feb 1991.

[93] H.-T. Wang, H. Q. Lin, and J.-L. Shen, "Bond-operator analysis of the magnetization of spin chains," *Phys. Rev. B*, vol. 61, pp. 4019–4025, Feb 2000.

[94] M. P. Gelfand, Z. Weihong, C. J. Hamer, and J. Oitmaa, "Spin-S bilayer Heisenberg models: Mean-field arguments and numerical calculations," *Phys. Rev. B*, vol. 57, pp. 392–397, Jan 1998.

[95] L. Fritz, R. L. Doretto, S. Wessel, S. Wenzel, S. Burdin, and M. Vojta, "Cubic interactions and quantum criticality in dimerized antiferromagnets," *Phys. Rev. B*, vol. 83, p. 174416, May 2011.

[96] E. C. Samulon, Y. Kohama, R. D. McDonald, M. C. Shapiro, K. A. Al-Hassanieh, C. D. Batista, M. Jaime, and I. R. Fisher, "Asymmetric quintuplet condensation in the frustrated S=1 spin dimer compound $Ba_3Mn_2O_8$," *Phys. Rev. Lett.*, vol. 103, p. 047202, Jul 2009.

[97] Z. Y. Meng, T. C. Lang, S. Wessel, F. F. Assaad, and A. Muramatsu, "Quantum spin liquid emerging in two-dimensional correlated Dirac fermions," *Nature*, vol. 464, pp. 847–851, Apr. 2010.

[98] P. W. Anderson, "New approach to the theory of superexchange interactions," *Phys. Rev.*, vol. 115, pp. 2–13, Jul 1959.

[99] E. Fradkin, *Field theories of condensed matter systems*, pp. 10–13. Addison-Wesley Publishing Co., 1991.

[100] B. K. Clark, D. A. Abanin, and S. L. Sondhi, "Nature of the spin liquid state of the Hubbard model on a honeycomb lattice," *Phys. Rev. Lett.*, vol. 107, p. 087204, Aug 2011.

[101] F. Wang, "Schwinger boson mean field theories of spin liquid states on a honeycomb lattice: Projective symmetry group analysis and critical field theory," *Phys. Rev. B*, vol. 82, p. 024419, Jul 2010.

[102] Y.-M. Lu and Y. Ran, "Z_2 spin liquid and chiral antiferromagnetic phase in the Hubbard model on a honeycomb lattice," *Phys. Rev. B*, vol. 84, p. 024420, Jul 2011.

[103] C. L. Henley, "Ordering due to disorder in a frustrated vector antiferromagnet," *Phys. Rev. Lett.*, vol. 62, pp. 2056–2059, Apr 1989.

[104] C. Weber, L. Capriotti, G. Misguich, F. Becca, M. Elhajal, and F. Mila, "Ising transition driven by frustration in a 2D classical model with continuous symmetry," *Phys. Rev. Lett.*, vol. 91, p. 177202, Oct 2003.

[105] E. Dagotto and A. Moreo, "Phase diagram of the frustrated spin-1/2 Heisenberg antiferromagnet in 2 dimensions," *Phys. Rev. Lett.*, vol. 63, pp. 2148–2151, Nov 1989.

[106] J. Sirker, Z. Weihong, O. P. Sushkov, and J. Oitmaa, "J_1–J_2 model: First-order phase transition versus deconfinement of spinons," *Phys. Rev. B*, vol. 73, p. 184420, May 2006.

[107] R. Darradi, O. Derzhko, R. Zinke, J. Schulenburg, S. E. Krüger, and J. Richter, "Ground state phases of the spin-$\frac{1}{2}$ $J_1 - J_2$ Heisenberg antiferromagnet on the square lattice: A high-order coupled cluster treatment," *Phys. Rev. B*, vol. 78, p. 214415, Dec 2008.

[108] L. Capriotti and S. Sachdev, "Low-temperature broken-symmetry phases of spiral antiferromagnets," *Phys. Rev. Lett.*, vol. 93, p. 257206, Dec 2004.

[109] C. L. Henley, "Ordering by disorder: Ground-state selection in FCC vector antiferromagnets," *J. Appl. Phys.*, vol. 61, no. 8, pp. 3962–3964, 1987.

[110] J. T. Chalker, P. C. W. Holdsworth, and E. F. Shender, "Hidden order in a frustrated system: Properties of the Heisenberg Kagomé antiferromagnet," *Phys. Rev. Lett.*, vol. 68, pp. 855–858, Feb 1992.

[111] J. Fouet, P. Sindzingre, and C. Lhuillier, "An investigation of the quantum J_1-J_2-J_3 model on the honeycomb lattice," *The European Physical Journal B - Condensed Matter and Complex Systems*, vol. 20, pp. 241–254, 2001.

[112] Villain, J., Bidaux, R., Carton, J.-P., and Conte, R., "Order as an effect of disorder," *J. Phys. France*, vol. 41, no. 11, pp. 1263–1272, 1980.

[113] C. N. Varney, K. Sun, V. Galitski, and M. Rigol, "Kaleidoscope of exotic quantum phases in a frustrated XY model," *Phys. Rev. Lett.*, vol. 107, p. 077201, Aug 2011.

[114] R. Moessner, "Magnets with strong geometric frustration," *CAN.J.PHYS.*, vol. 79, p. 1283, 2001.

[115] F. Y. Wu, "The Potts model," *Rev. Mod. Phys.*, vol. 54, pp. 235–268, Jan 1982.

[116] C. K. Majumdar and D. K. Ghosh, "On next-nearest-neighbor interaction in linear chain. I," *J. Math. Phys.*, vol. 10, no. 8, pp. 1388–1398, 1969.

[117] R. Kumar, D. Kumar, and B. Kumar, "Honeycomb antiferromagnet with a triply degenerate dimer ground state," *Phys. Rev. B*, vol. 80, p. 214428, Dec 2009.

[118] S. Gopalan, T. M. Rice, and M. Sigrist, "Spin ladders with spin gaps: A description of a class of cuprates," *Phys. Rev. B*, vol. 49, pp. 8901–8910, Apr 1994.

[119] B.-J. Yang, A. Paramekanti, and Y. B. Kim, "Competing quantum paramagnetic ground states of the Heisenberg antiferromagnet on the star lattice," *Phys. Rev. B*, vol. 81, p. 134418, Apr 2010.

[120] J. Richter, J. Schulenburg, A. Honecker, and D. Schmalfuß, "Absence of magnetic order for the spin-half Heisenberg antiferromagnet on the star lattice," *Phys. Rev. B*, vol. 70, p. 174454, Nov 2004.

[121] E. Rastelli, A. Tassi, and L. Reatto, "Non-simple magnetic order for simple Hamiltonians," *Physica B*, vol. 97, no. 1, 1979.

[122] F. A. Lindemann *Phys. Z.*, vol. 11, p. 609, 1910.

[123] P. P. Orth, D. L. Bergman, and K. Le Hur, "Supersolidity of cold-atom Bose-Fermi mixtures in optical lattices," *Phys. Rev. A*, vol. 80, p. 023624, Aug 2009.

[124] T. Ohgoe, T. Suzuki, and N. Kawashima, "Novel mechanism of supersolid of ultracold polar molecules in optical lattices," *ArXiv e-prints*, Apr. 2011.

[125] A. V. Gorshkov, S. R. Manmama, G. Chen, J. Ye, E. Demler, M. D. Lukin, and A. M. Rey, "Tunable superfluidity and quantum magnetism with ultracold polar molecules," *ArXiv e-prints*, June 2011.

[126] T. Momoi and K. Totsuka, "Magnetization plateaus of the Shastry-Sutherland model for $SrCu_2(BO_3)_2$: Spin-density wave, supersolid, and bound states," *Phys. Rev. B*, vol. 62, pp. 15067–15078, Dec 2000.

[127] E. C. Samulon, Y. Kohama, R. D. McDonald, M. C. Shapiro, K. A. Al-Hassanieh, C. D. Batista, M. Jaime, and I. R. Fisher, "Asymmetric quintuplet condensation in the frustrated S=1 spin dimer compound $Ba_3Mn_2O_8$," *Phys. Rev. Lett.*, vol. 103, p. 047202, Jul 2009.

[128] A. Vishwanath, L. Balents, and T. Senthil, "Quantum criticality and deconfinement in phase transitions between valence bond solids," *Phys. Rev. B*, vol. 69, p. 224416, Jun 2004.

[129] L. D. Landau, "The theory of superfluidity of Helium II," *J. Phys. (USSR)*, vol. 5, p. 71, 1941.